universität wien

MASTERARBEIT

Titel der Masterarbeit

„Phase Equilibria in the Intermetallic System Li-Cu-Sb“

verfasst von

Alexander Beutl, BSc.

angestrebter akademischer Grad

Master of Science (MSc.)

Wien, 2014

Studienkennzahl lt. Studienblatt:	A 066 862
Studienrichtung lt. Studienblatt:	Masterstudium Chemie
Betreut von:	Ao. Univ.–Prof. MMag. Dr. Hans Flandorfer

Preface

This work was undertaken from October 2013 to June 2014 in the working group of Ao. Univ. -Prof. MMag. Dr. Hans Flandorfer at the department of Inorganic Chemistry (Materials Chemistry).

I want to thank my thesis supervisor Prof. Flandorfer, who entrusted me with such an interesting research topic, and guided me through the entire work.

Furthermore, I want to thank all my colleagues in the whole department for their continuous support, especially Mag. Siegfried Fürtauer, who showed much patience with me and never turned me away, when I had a question.

Special thanks go to Ao. Univ.-Prof. Dr. Herta Effenberger, who conducted the single crystal measurements and took much effort in characterizing newly found phases.

Also I want to thank Mag. Dr. Franz Jirsa for his help conducting AAS measurements of my samples.

Finally I want to thank the FWF (Fonds zur Förderung der wissenschaftlichen Forschung), for providing funds for this work by the project I559-N19

Table of contents

1. Introduction

The energy demand of today's society is ever increasing. Up until now, thermal power stations provided most of the electric energy needed. However, the shortage of fossil fuels leaves us with the challenge to use other energy sources more efficiently. Nuclear power plants are problematic due to the radioactive waste they produce. Therefore renewable energy sources like wind and solar energy are preferable. However, efficient energy storage units are necessary to maintain a steady energy supply. Rechargeable lithium ion batteries (LIBs) are recognized as potential energy storage systems for this purpose. However, current LIBs are not fit for this high energy application, especially in terms of energy density, lifetime and safety of operation. Therefore a new generation of LIBs has to be developed which is capable to respond to the demands of modern society.

New electrode materials have the potential to effectively increase the capacity as well as safety of operation of LIBs. Accompanying the lithiation of these materials though, volume changes of up to over 300% occur. Hence much research has been conducted to cope with this problem. A potential solution to reduce the volume change during lithiation is to use intermetallic phases, which are able to incorporate lithium while maintaining their structural integrity. However the search for these materials is overwhelming due to the amount of possible systems. Naturally computer calculations have to be used, to determine which intermetallic systems are reasonable candidates for electrode materials. Even so, without detailed thermodynamic information about these systems, i.e. without accurate experimental data, computer simulations have not the potential to describe intermetallic systems adequately.

This work was conducted in the framework of the priority program WenDeLIB SPP 1473, which aims to address the lack of thermodynamic data, by conducting experimental investigations as well as theoretical calculations in systems, which are relevant for new electrode materials for LIBs. The focus of this work lies in the performance of initial experiments in the binary Li-Sb and ternary Cu-Li-Sb systems. Although much literature has already been published about the Li-Sb phase diagram, there are still many uncertainties, especially regarding the phase transition temperatures. Samples with different Li content were prepared and analyzed by means of X-ray powder diffraction

(XRPD) and difference thermal analysis (DTA). Also first steps were taken to reconstruct the binary phase diagram on the basis of the executed measurements.

In the ternary system an isothermal section at 400°C was investigated. Samples were prepared by adding Li to Cu-Sb alloys. Subsequent analysis by XRD and DTA were conducted. Also single crystal x-ray diffraction (SXRD) was done, in order to characterize yet unknown ternary compounds.

2. Lithium-Ion batteries (LIBs)

2.1. General introduction to LIBs

Since the advent of the Li-ion rechargeable batteries in 1991 [1], they have increased to influence our daily lives more and more. Many products which are readily available nowadays were regarded as science fiction a couple of years ago. Smart phones and tablet-computers wouldn't be as convenient without the high energy density of LIBs. Among the advantages of LIBs are [2]:

- High voltage
- High energy density
- Low self-discharge rate
- Wide temperature range of operation

Current standard of technology yields energy densities of 100 to 150 Wh/kg. This is quite a high value compared to other battery technologies like lead-acid and nickel-hydride cells as seen in Fig. 1 [3]. The self-discharge rate of commercial LIBs lies by 2-8% per month. Over 1000 charge/discharge cycles are possible and an operation temperature range between -20°C and 60°C makes LIBs the number one choice for mobile electronic devices. However the use of LIBs also shows some drawbacks. As far as safety is concerned, LIBs have to be protected from over-charge, as this leads to capacity loss or even thermal runway, which may end in an explosive destruction of the battery. Therefore most of the commercially available LIBs are provided with some kind of protective circuitry to ensure safety of handling [4].

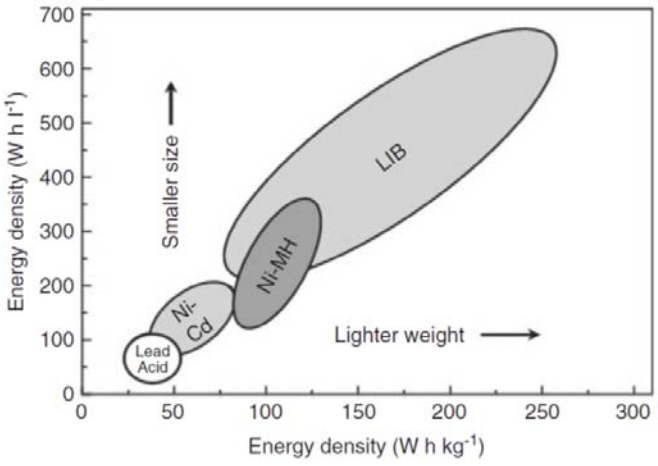

Fig. 1, Specific energies and energy densities of different battery systems are plotted against each other [3].

For future high energy applications, LIBs are regarded as potential storage media including smart grits and electronic vehicles. However, the current technology is not able to produce LIBs which are suited for this kind of applications. The highest energy density value is exhibited by gasoline and lies in the range of 12.000Wh/kg. Although this is a theoretical value and the practical value is only a fraction of the theoretical one, it still provides an effective energy density of about 1000Wh/kg. For LIBs to be able to compete with gasoline, energy densities of at least 500-800Wh/kg have to be provided [3]. However not only the energy density of LIBs has to be improved, but also the safety of performance and the cycle life are major concerns [3].

The general structure of a lithium ion battery is shown in Fig. 2. The working principle is relatively straightforward. During charging of the battery, Li^+-ions are emitted from the cathode material and migrate through the electrolyte to the anode. There they react with or intercalate into the anode material, which is reduced. During discharge, the reaction is reversed and a current flows, which is able to do work.

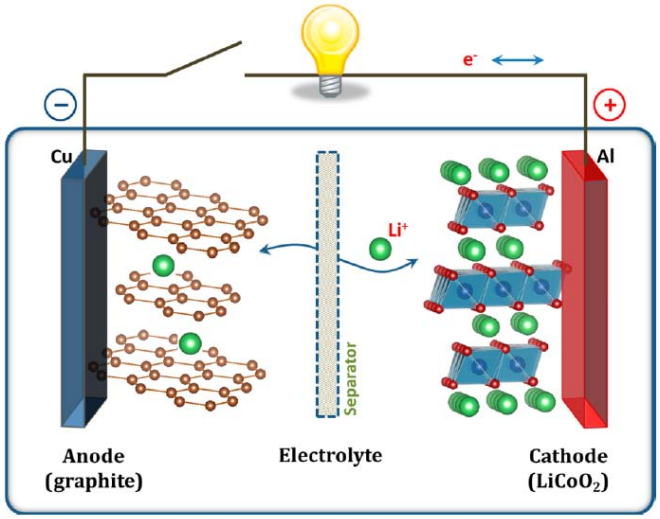

Fig. 2, Working principle of a LIB. The setup shown here reflects the structure of the first commercialized LIBs, using $LiCoO_2$ for the cathode and graphite for the anode [5].

There are three crucial components, which determine the main properties of an electrochemical cell.

- The cathode
- The anode
- The electrolyte

The electrochemical potentials of the anode and cathode determine the open circuit voltage, see equation (1). The open circuit voltage, is the potential difference of the two half cells of a battery, when the electrical circuit is not closed.

$$V_{oc} = (\mu_a - \mu_c)/e \qquad (1)\ [5]$$

The open circuit voltage is limited by the electrolyte "window". This is the voltage range in which the electrolyte is stable. As the highest occupied molecular orbital (HOMO) of the electrolyte should not lie below the electrochemical potential of the cathode (μ_c) and the lowest unoccupied molecular orbital of the electrolyte should not lie above the chemical potential of the anode (μ_a), the open circuit voltage is restricted to certain values. In the first case, the electrolyte would be oxidized by the cathode and in the latter case, the electrolyte would be reduced by the anode [5]. This is illustrated in Fig. 3.

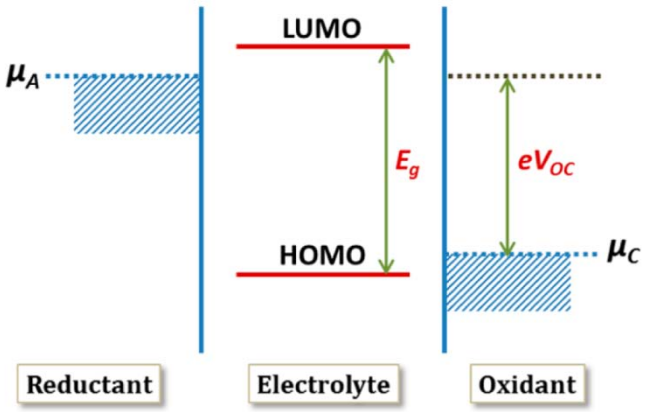

Fig. 3, The electrolyte window (E_g) is shown in relation to the chemical potentials of the anode (μ_a) and cathode (μ_c) materials, which determine the open circuit potential V_{oc} [5].

The electrolytes of current LIBs are organic esters or polycarbonates mixed with a lithium salt like lithium hexafluorophosphate, $LiPF_6$. In general these kinds of substances are volatile as well as flammable and are therefore seen as a safety issue. New electrolytes are currently under investigation, including ionic liquids, polymer and ceramic electrolytes. The first commercialized LIB used $LiCoO_2$ as the cathode material and graphite as the anode material. Since then, much research was undertaken to improve their properties regarding energy density and safety of operation [5].

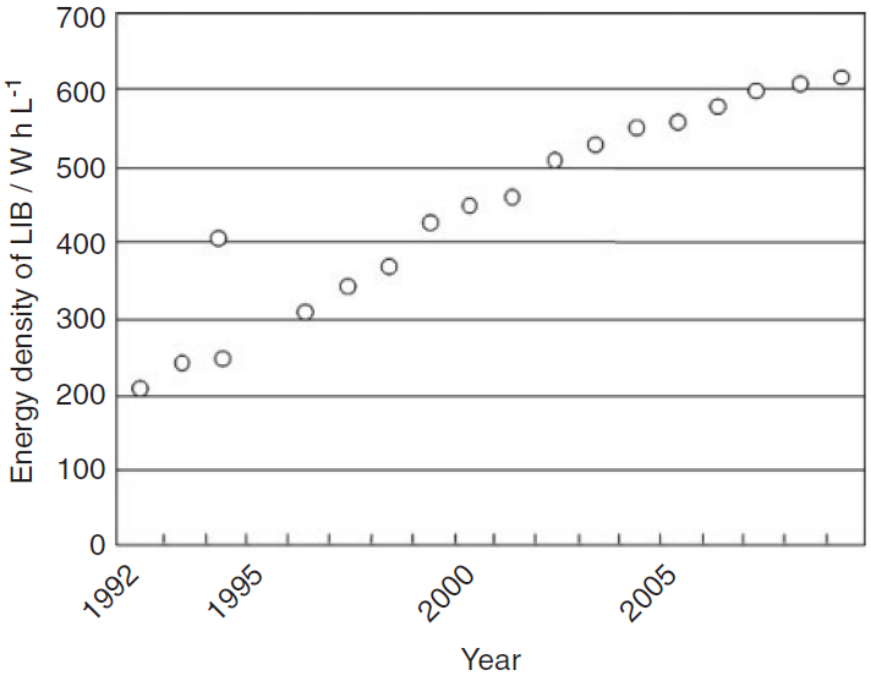

Fig. 4, The development of the energy densities of LIB in the course of time is shown. The saturation of the increase in capacity can easily be seen [3].

In Fig. 4 the energy-density development of LIBs is shown during the course of the years. It can be seen that the increase of energy density is slowly saturating. This saturation is a result of the focus of battery research up until now. The main goal was to optimize the already established electrode materials, rather than searching for new ones. This approach was very successful at first, yielding higher and higher energy densities mainly by optimizing packaging, but as can be seen in Fig. 4, it has almost reached its limits now. The electrode materials like $LiCoO_2$ or graphite are fully optimized and at their maximum capacities. In order to develop new LIBs with even higher energy densities, new electrode materials have to be developed [3].

2.2. Anode materials for LIBs.

The current anode material of choice for LIBs is graphite. Due to its long cycle life, abundance and relatively low price, it has been used in different shapes and forms as an anode material for LIBs. However by using graphite as an electrode material, batteries are restricted to a relatively low theoretical energy density. The fully lithiated compound of graphite, LiC_6, has a theoretical charge density of 372mAh/g_C [6]. Other elemental electrodes like Si or Sn show much higher lithium uptake capacities per atom. Si, for

example, forms the compound $Li_{4.4}Si$, which has a theoretical capacity of 4200 mAh/g_{Si} or 2100 mAh/$g_{Li4.4Si}$. This shows the huge potential lying within these so called **alloy electrodes**.

Fig. 5 shows the gravimetric and volumetric theoretical energy densities of some alloy anodes [7]. Graphite is among the compounds with the lowest energy-densities. Si ($Li_{3.75}Si$) and Sn have almost ten times and 3 times the gravimetric capacity of graphite. Therefore these materials might be the key to bring LIBs to the next level and make them capable to be used as high-energy storage media [7].

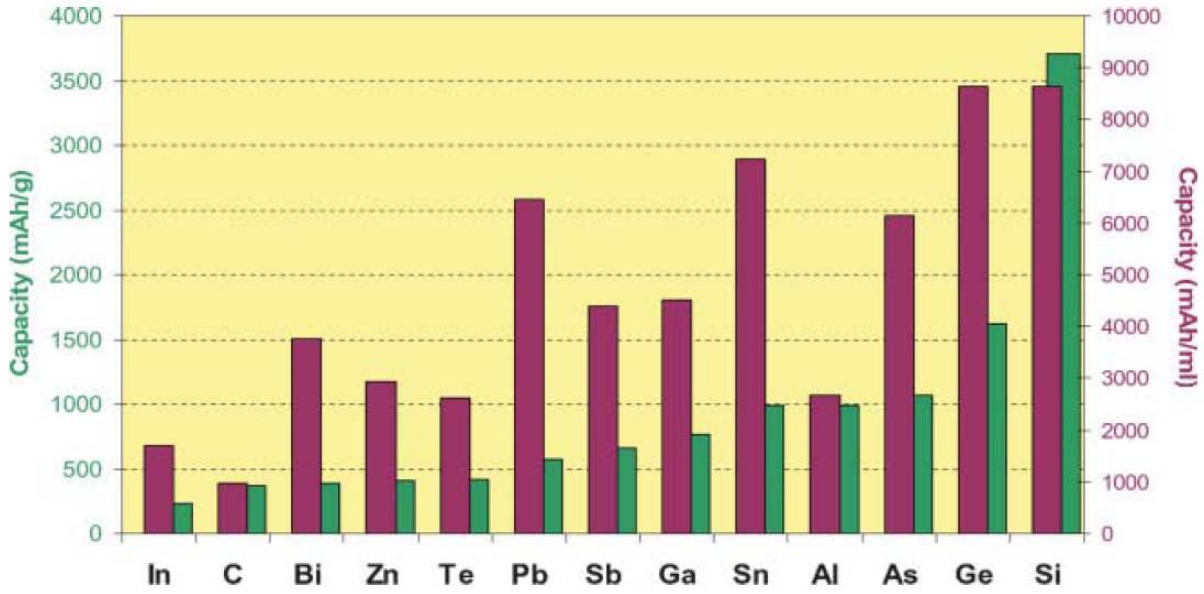

Fig. 5, The volumetric (green) and gravimetric (red) capacities of some anode materials [7].

Another advantage of alloy anodes is the operation potential vs. lithium [6]. As seen in Table 1, the graphite electrode has a potential of just 0.05V against Li. Therefore if the potential of the battery varies just a little bit due to e.g. overcharge, lithium plating might occur. This means that rather than lithium intercalation, elemental lithium deposition occurs at the anode. This is a major concern especially in regard of safety of operation. Anode degradation promotes this effect even further. Various aging mechanisms are responsible for capacity losses at the anode material, leading to a polarization of the anode. Therefore overcharge can occur more easily and lithium plating occurs to an even higher extend. Although lithium plating is reversible (deposited lithium is oxidized at potentials of about 100mV, which is much lower than the de-intercalation potential used),

it still causes safety issues. The plated lithium is able to form dendrites (long, thin crystallites), which grow across the electrolyte, reaching the cathode material. There they might cause short-circuit, resulting in a local increase in temperature. As most electrolytes for LIBs are flammable, the worst case would be a thermal runway of the battery, which can end in an explosive destruction of the cell [8]. Alloy anodes though have a higher potential against Li and are therefore more resistant to overcharge, reducing the risks of lithium plating [9].

Table 1 Comparison of the electrochemical properties of different anode materials [6].

Materials	Li	C	Si	Sn	Sb	Al	Mg	Bi
Density (g cm^{-3})	0.53	2.25	2.33	7.29	6.7	2.7	1.3	9.78
Lithiated phase	Li	LiC_6	$Li_{4.4}Si$	$Li_{4.4}Sn$	Li_3Sb	LiAl	Li_3Mg	Li_3Bi
Theoretical specific capacity (mAh g^{-1})	3862	372	4200	994	660	993	3350	385
Theoretical charge density (mAh cm^{-3})	2047	837	9786	7246	4422	2681	4355	3765
Volume change (%)	100	12	320	260	200	96	100	215
Potential vs. Li (V)	0	0.05	0.4	0.6	0.9	0.3	0.1	0.8

Disregarding all perks and merits of the alloy electrodes, they exhibit a huge drawback. The volumetric changes upon lithiation are devastating. In Table 1 the volume change upon lithiation of some materials are listed. Graphite exhibits a volume change of only 12% upon formation of LiC_6. The fully lithiated silicon compound, $Li_{4.4}Si$, shows a volume expansion of 320% compared to pure silicon.

The volume change is calculated by dividing the molar volume of the product by the sum of the molar volumes of the reactants. Regarding the example of Si, the reactants would be 4.4Li and pure Si and the product would be $Li_{4.4}Si$, as depicted in equation (5)[9]:

$$4.4Li + Si \rightarrow Li_{4.4}Si \quad (2)$$

A change in volume of over 300% is of course a serious drawback in regard of using these materials as electrodes for LIBs. The mechanical stress, which is applied onto the electrode during charge/discharge, yields fractures in the material and the structural integrity cannot be ensured. Therefore a major research topic at the moment is to lower this volume change. There are several approaches to solve this problem of which three are described below [6]:

- Multiphase composites:

A host matrix is used to buffer the volume change of the active material. The matrix material has to ensure rapid electron as well as Li-ion transport and must be structurally invariant during the electrode reaction. The matrix material also inhibits the aggregation of active particles during the charge/discharge process.

- Particle size control:

By reducing the particle size of the active material below 100nm, the cycling performance of alloy anodes can be improved. The reason for this lies in the enhanced mechanical stability of nano-crystalline alloys. Due to the decreased grain size, the fracture strength of metals is increased. This phenomenon can be explained by the inhibiting effect of nano-sized grains, to the formation of pile-ups of dislocations. Therefore the electrode material can resist the stress of the volume change during lithiation. Also the high concentration of grain boundaries enhances Li-ion transport and can be even used for additional Li-storage.

- Intermetallics:

Not the pure metals but, intermetallic compounds are used as electrodes. These compounds have to exhibit either a stable sublattice structure, similar to the graphite layers in which Li-ions are inserted, or they form a ductile component which is inactive against lithium and is extruded in the course of lithiation.

The lithiation process for graphite is mainly intercalation of the Li^+ ions between the graphite planes as shown in Fig. 2. Intermetallic electrodes can exhibit different solid-state reactions with lithium. The three main mechanism of lithiation can be described as follows [9]:

- Insertion reaction:

$xLi + AB_y \rightarrow Li_xAB_y$ (3)

In general the host structure AB_y and the ternary compound Li_xAB_y have same crystal structures.

- Displacement reaction

$xLi + AB_y \rightarrow Li_xB_y + A$ (4)

Here one of the compounds of the host structure is extruded in the course of lithiation.

- Mixed reaction

$xLi + AB_y \rightarrow Li_xA_{1-z}B_y + A_z$ (5)

In this process, both insertion and displacement reactions occur in parallel. Only a part of A is displaced and the ternary compound $Li_xA_{1-z}B_y + A_z$ is formed.

For the two latter cases we can distinguish between both, A and B forms Li-compounds or only A or B can uptake Li. The respective second element is inert against Li.

In general not only one, but all of the reactions described above can be observed during lithiation, resulting in different reaction steps [9]. It is important to know the reaction processes taking place during charge or discharge of an electrochemical cell, in order to be able to optimize the system and estimate the properties of the cell. However, it is necessary to describe the intermetallic system in a phase diagram first, before determining the reaction sequence during charge/discharge. Therefore it is necessary to calculate the stability and thermodynamic phase equilibria of potential binary and ternary systems using CALPHAD [10]. However, in order to provide a basis for these calculations, experimental data have to be obtained. Of special importance is the experimental exploration into the ternary for identifying ternary compounds because with CALPHAD a hitherto unknown phase cannot be predicted.

2.3. Sb and Cu_2Sb as electrode materials

The fully lithiated antimony compound is Li_3Sb. It has a theoretical charge density of 4422mAhcm^{-3}, which is more than five times the charge density of graphite. The potential vs. lithium is about 0.9V. This lowers the open circuit potential compared to graphite, but also reduces the possibility of lithium plating [6].

Upon lithiation, the first reaction step yields Li_2Sb. After complete conversion, the Li_2Sb phase reacts further to Li_3Sb. These two reactions take place at different potentials.

$$Sb + 2Li \rightleftharpoons Li_2Sb \quad (6)$$

$$Li + Li_2Sb \rightleftharpoons Li_3Sb \quad (7)$$

Wang et.al. [11] determined a potential of 0.948V against Li for reaction (6) and 0.956V for reaction (7). As can be seen in Fig 6a, at room temperature there is almost no shift of

voltage during lithiation [11]. At higher temperatures though, the two potentials shift apart, resulting in a significant voltage drop in the E vs. x_{Li} diagram.

The flat charge/discharge profile of Sb was already reported by Besenhard in 1975, who also saw the potential of using Sb as an electrode material for lithium ion batteries [12]. However pure Sb exhibits a volumetric change during lithium uptake of about 200%. Therefore it is not possible to use pure Sb as an electrode material.

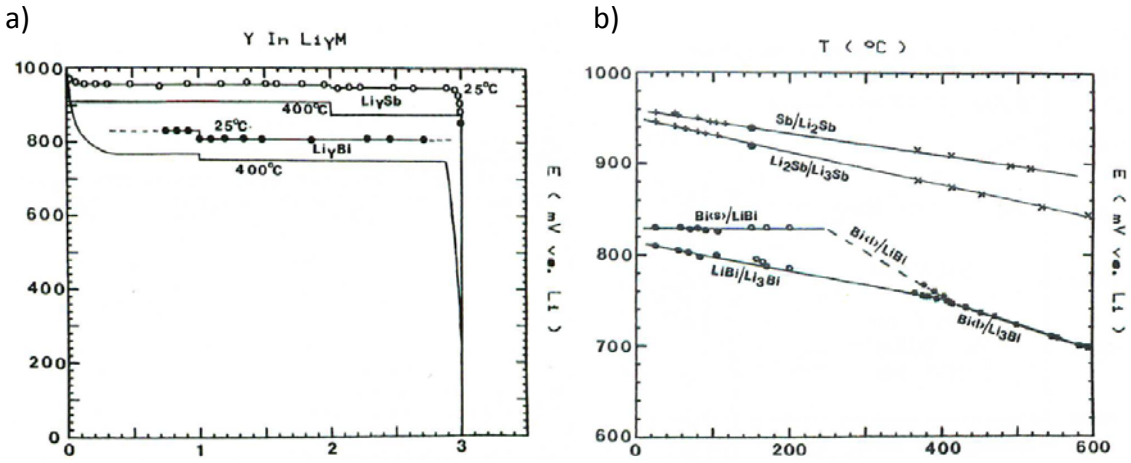

Fig. 6a, Coulometric titration curves for Li-Bi and Li-Sb are shown. The potential step at the transition from reaction (6) to reaction (7) is hardly visible at 25°C. At 400°C the potential step can be clearly seen. b, Temperature dependence of the potentials for Li-Sb and Li-Bi systems. At higher temperatures, the curves for reaction (6) and (7) shift apart [11].

That is the reason why the investigation shifted towards intermetallic materials, which show only a very low volumetric distortion upon lithiation. One of these materials, which are currently under investigation, is Cu_2Sb. Fransson et. al. reported [13] that Cu_2Sb exhibits excellent cycling stability providing a rechargeable capacity of 290mAhg^{-1}. During the first charge-discharge cycle, the electrode undergoes a large capacity loss of 36%. However after this "conditioning" cycle, the charge capacity of the electrode material is stable (see Fig. 7).

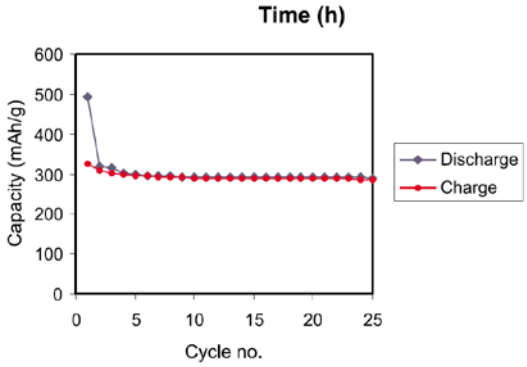

Fig. 7, Plot of capacity vs. cycle number of a Li/Cu2Sb electrode [12].

The main reason for these promising properties of Cu_2Sb is the strong structural relations between the host structure and the lithiated phases (Cu_2Sb-$CuLi_2Sb$-Li_3Sb). However there are still some uncertainties regarding which lithiated phases are formed and which reaction path is taken (intercalation/extrusion). The reaction mechanisms already proposed are quite different from each other. Matsuno et. al. [14] proposes the following reaction path:

1. Li + Cu2Sb → CuLiSb + Cu (three-phase coexistence reaction)
2. Li + CuLiSb → $CuLi_{1+x}Sb$ ($0 \leq x \leq 0.5$, solid solution reaction)
3. $(2 - x)$Li + $CuLi_{1+x}Sb$ → Li_3Sb + Cu ($x \leq 0.5$, three-phase coexistence reaction)

In contrary, Sharma [15] calculated the following reaction scheme:

1. 0.5Li + Cu_2Sb → $CuLi_{0.5}Sb$
2. 0.5Li + $CuLi_{0.5}Sb$ → $Cu_{1.5}LiSb$ + 0.5Cu
3. Li + $Cu_{1.5}LiSb$ → $CuLi_2Sb$ + 0.5Cu
4. Li + $CuLi_2Sb$ → Li_3Sb + Cu

The two reaction schemes presented above are based on thermodynamic calculations and EMF measurements. However, no effort was made to synthesize the proposed lithiated phases, to confirm their existence. There is a general lack of fundamental thermodynamic data in the system Cu-Li-Sb, which is one reason, why it is difficult to determine the phase equilibria during lithiation.

3. Literature review

3.1. The binary system Li-Sb

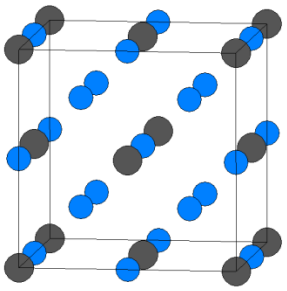

Fig. 8, α-Li_3Sb (Fm-3m)

The first reported Li-Sb compound was found in 1902 by LeBeau [16]. He observed that the two elements, Li and Sb, readily react exothermically upon heating. To control the amount of lithium added to antimony, he used an electrochemical approach. He put a graphite anode and an antimony cathode into a melt of KCl/LiCl (1:1) and applied a current of 15A. Tiny crystallites with the composition Li_3Sb solidified in the melt. LeBeau was also able to form the compound by wet chemical methods [16]. He solved lithium in liquid ammonia, yielding a blue solution. Then powdered antimony was added until the blue color of the solution vanished. After distillation of the ammonia, Li_3Sb was acquired. LeBeau reported a melting point of the compound of over 960°C.

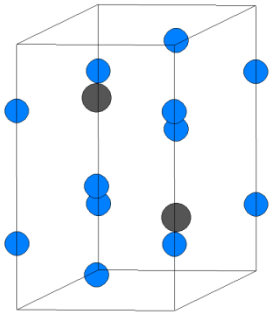

Fig. 9, β-Li_3Sb ($P6\frac{3}{m}mc$)

Later Brauer and Zintl [17] followed the working procedure of LeBeau to form Li_3Sb. After annealing the compound at different temperatures, ranging from 320-650°C, they used XRPD to solve the respective crystal structure. They found that Li_3Sb crystallizes in a cubic structure, namely Fm-3m, which is isotypically to Li_3Bi. They also tried to form the compound metallurgically by melting the stoichiometric amounts of the elements in iron crucibles. However they encountered difficulties. Antimony readily reacts with iron and therefore many crucibles were attacked by the samples and were destroyed during the melting process. However it was possible to analyze one sample, which was melted at 1300°C, by means of XRPD. Surprisingly they found that the sample exhibited a hexagonal structure. The compound Li_3Sb therefore does not only exist in a low-temperature cubic structure, but exhibits also a high-temperature hexagonal modification. They named the low-temperature modification β-Li_3Sb and the high-temperature modification, α-Li_3Sb, but later the names were switched due to conformity with other systems.

Not before 1974, a second binary compound was reported by Réne Gérardin and Jacques Aubry [18]. They formed the compound Li_2Sb by mixing powders of antimony and Li_3N (at the ratio of 3:2) and stepwise heating of the mixture for 24 hours at a maximal temperature of 430°C (100°C, 200°C, 300°C, and 430°C). The process was undertaken in a dry and oxygen free atmosphere. They determined the crystal structure of the compound by XRPD, which was P-62c. Gérardin also reported some data related to the melting point of this phase. Li_2Sb is still stable at 1000°C but decomposes at 1200°C. This information is very vague, as it is not clear, whether he means that the compound melts at 1000°C or whether it is just not yet decomposed at the given temperature.

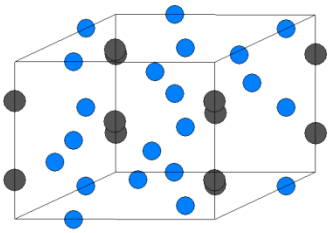

Fig. 10, Li_2Sb (P-62c)

In 1993 Sangster and Pelton [19] calculated the binary Li-Sb phase diagram on the basis of experimental data from various research groups. They used the modified quasichemical model to account for the ordering at about 25at.% of Li (Li_3Sb). The experimental data they relied upon though are very inaccurate (see e.g. reported melting points above [17], [18]) and therefore the phase transition temperatures do not reproduce the real ones precisely. This was indicated by a wave sign beside the value of the phase transition temperatures, in the phase diagram. Especially the liquidus curve may be too low and exhibits an error limit at higher temperatures, as proposed by the authors, of +150°C and -50°C. Also the lithium rich side of the phase diagram is not resolved clearly. The authors calculated a solubility of Sb in Li below 0.01at%. They assume a eutectic reaction occurring at 0.05°C below the melting point of lithium. This assumption is valid and probable; however a peritectic reaction might also be possible. The four phase equilibrium at >650°C is not possible according to the Gibbs phase rule. However, this is a special case in which two reactions are so close to each other, that they cannot be resolved easily and are therefore degenerated. This is discussed in more detail below.

Also in the binary phase diagram collection of Massalski [20], the Li-Sb system can be found. The one calculated by [21] is pictured, but almost all lines are dotted or dashed, indicating the inaccuracy of the shown phase diagram. This visualization reflects the current information about this system more readily. In Fig. 11 the phase diagram calculated by [19], and the one depicted in [20] are shown.

All in all there are still many open questions concerning the binary Li-Sb phase diagram. Therefore a complete experimental revision is necessary to support the theoretical calculations with mandatory experimental data to eliminate the inaccuracies and errors in the current phase diagram.

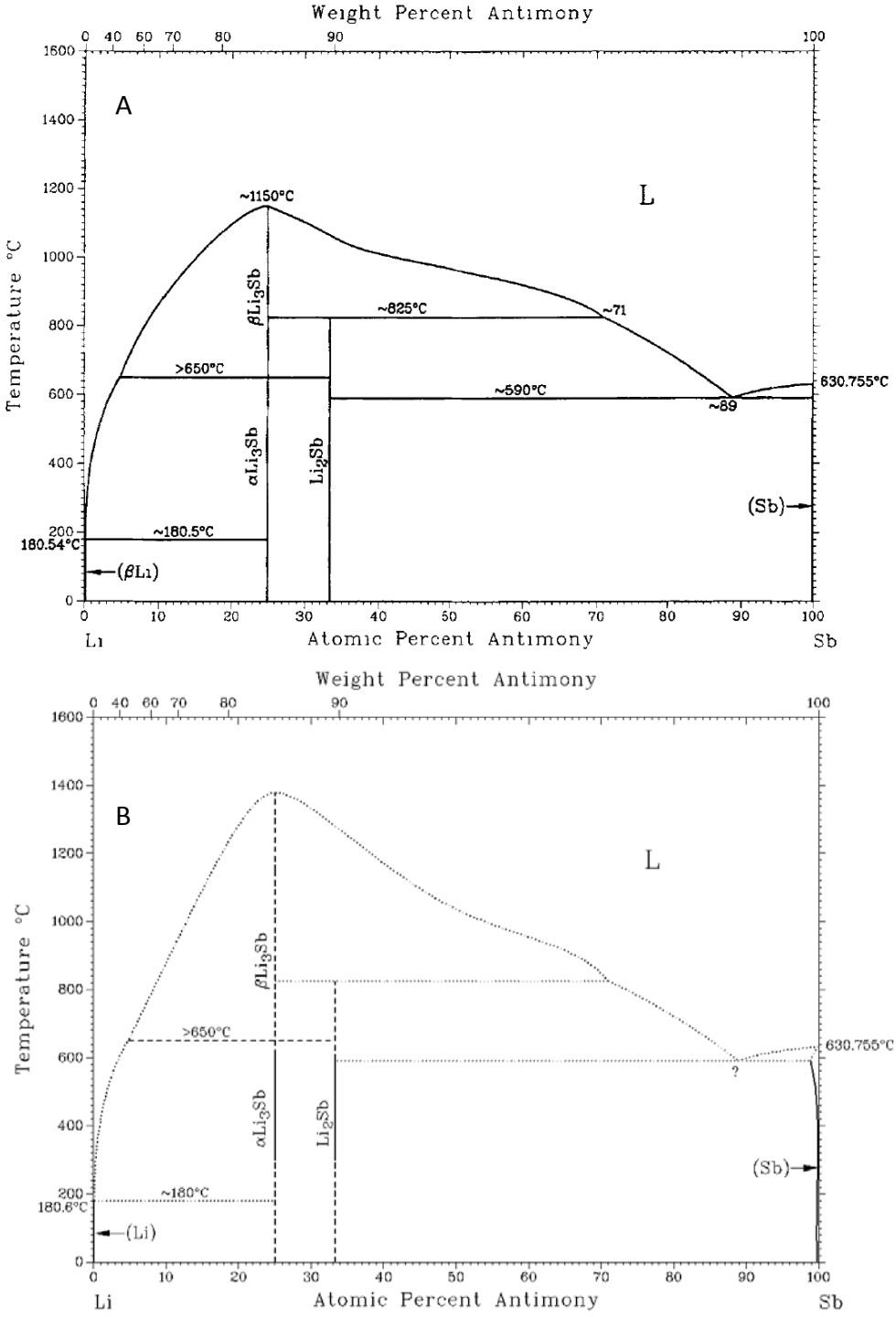

Fig.11, Phase diagram calculated by Sangster and Pelton in 1993 [19] (A) and found in Massalski 1995 (B) [20].

3.2. The binary system Cu-Li

The copper-lithium system is shown in Fig. 12. It exhibits only one eutectic reaction near pure lithium (0.01at% Li [21]).

Table 2, reactions in the binary system Cu-Li.

Name	Reaction	Reaction type	Temperature [°C]
E1	L → Cu + Li	Eutectic	180.5

No binary compounds were yet characterized. Li shows a significant solubility in copper of about 20at.% at 300°C [22]. Although the phase diagram seems to be quite simple, there are still some unresolved issues. Pelton, who reviewed the Cu-Li system in 1986 [21], reported that the very flat liquidus curve might indicate an immiscibility gap in the liquidus region. When this immiscibility gap would extend into the liquid region, a monotectic reaction would be the result. An example of a monotectic reaction is shown in the inset of Fig. 12. The similarity to the Cu-Li phase diagram is obvious. Pelton based his assessment of the Cu-Li system on the experimental data obtained by Pastorello [23]. As Pastorello, measured only one sample in the concentration region of the immiscibility gap, Pelton assumes that it might has been overlooked.

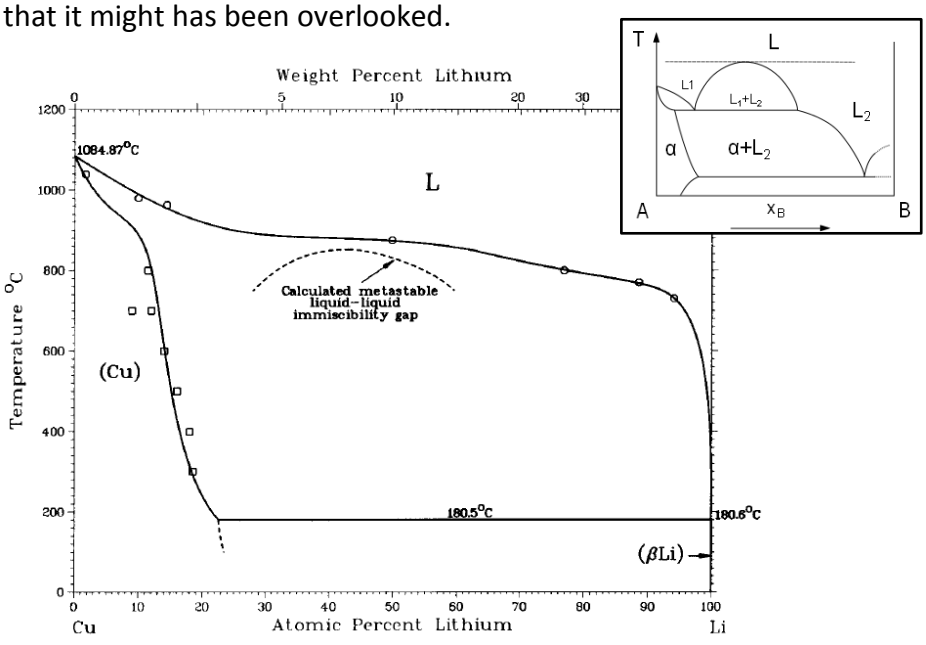

Fig. 12, The Cu-Li phase diagram as reported by Pelton [21]. The inlet shows a scheme of a monotectic reaction.

Another point of discussion is whether binary Cu-Li compounds exist or not. Dudel et. al. [24] reported that during physical vapor deposition of lithium onto copper foils, Cu-Li crystallites formed. These crystallites were analyzed by means of inductively coupled plasma atomic absorption spectroscopy (ICP-AAS) and XRPD. The results of the AAS measurements indicate a stoichiometry of Cu_4Li. The XRD pattern showed that the crystal structure of the crystallites is an fcc structure with a lattice parameter, which is a little bigger than the one for copper, which also crystallizes in the fcc structure. Van de Walle et al. [25] though suggests, that the Cu_4Li phase is rather a copper rich solid solution of a bcc CuLi phase, which undergoes a second order transition into a bcc solid solution at higher temperatures (900K-1200K). He supports his suggestion with first principle calculations and emf measurements conducted in the Cu-Li system. However Gasior et. al. [26] assumes, that both, the Cu_4Li and the CuLi phases might have been metastable phases. He also conducted theoretical calculations in parallel with emf experiments to conclude that a different phase exists in the binary system. This phase is only stable at temperatures above 500°C and decomposes metatectically into pure copper and liquid. Gasior et al. [26] reported, that this decomposition justifies the lack of structural data of this phase. However the stoichiometry is estimated to be about Cu_2Li_3. The existance of this phase is only indicated by emf measurements but there is no proof from DTA or XRD! As can be seen, there are still many open questions about the Cu-Li system. For this work, the assessed phase diagram of Pelton was used, as it provides a simple basis for further investigations, without any binary compounds, which are not confirmed yet.

3.3. The binary system Cu-Sb

The Cu-Sb system is rather complex and was recently discussed in detail by [27]. It seems, that there are no major points of discussion anymore, concerning this phase diagram. The β-phase was reported to be not quenchable, decomposing into the δ- and ε-phase. At 400°C there are three thermodynamically stable binary compounds, the δ-, ε-, and η-phase which correspond to approximately Cu_4Sb, Cu_3Sb and Cu_2Sb.

Table 3, reactions in the binary system Cu-Sb

Name	Reaction	Reaction type	Temperature [°C]
L1	L → β	Congruent melting	690
E1	L → (Cu) + β	eutectic	645
P1	L + β → η	Peritectic	586
E2	L → η + (Sb)	Eutectic	526
P2	(Cu) + β → γ	Peritectic	484
P3	β + γ → δ	Peritectic	467
P4	β + δ → ε	Peritectic	440
E3	β → ε + η	Eutectic	427
E4	γ → (Cu) + δ	Eutectic	440
P5	δ + ε → ζ	Peritectic	390
E5	ε → ζ + η	Eutectic	360
E6	ζ → δ + η	Eutectic	260

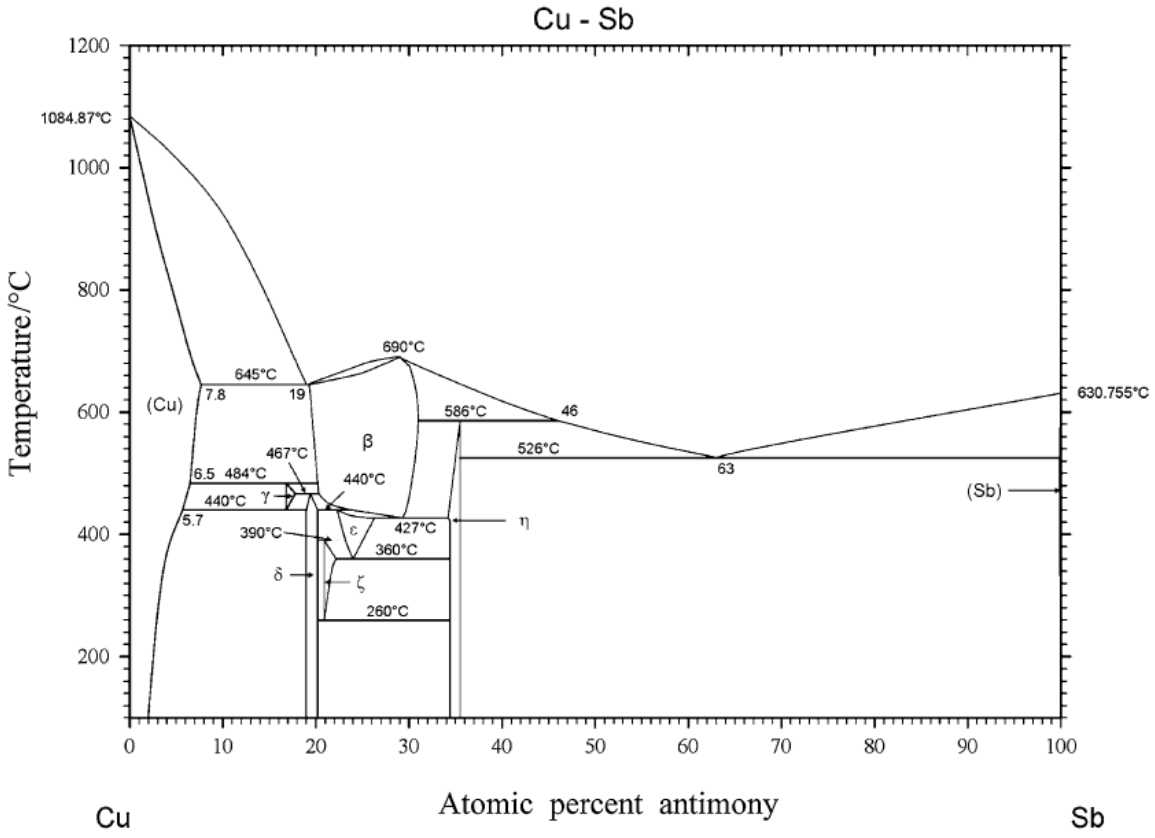

Fig.13, The binary system Cu-Sb as reported by [27].

3.4. The ternary system Cu-Li-Sb

The ternary system Cu-Li-Sb is not completely unknown. Already in 1968, Pauly et al. [28] found the ternary compound $CuLi_2Sb$ in the course of his study about intermetallic phases with the general formula Li_2EX (E = Cu, Ag, Au; X = Al, Ga, In, Tl, Si, Ge, Sn, Pb, Sb, Bi). He prepared his samples in iron crucibles and claimed a very low final iron content of the samples after melting them under dry air. He determined the crystal structure of the compound by means of powder x-ray diffraction.

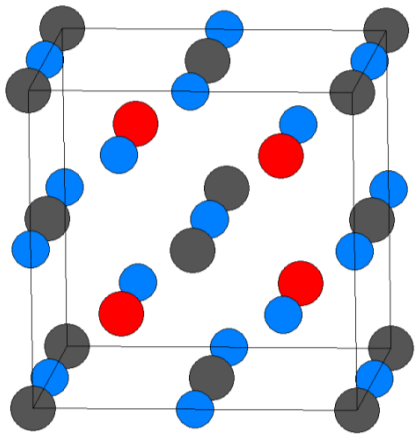

Fig. 14, The structure of the compound $CuLi_2Sb$. Lithium (blue), copper (red), antimony (grey) [14].

Apart from this, no other ternary compound was experimentally found yet. Nonetheless, EMF measurements were conducted in this system [14, 13] and theoretical calculations were made [15, 29]. The published papers on this system though were mainly concerned with the mechanism of lithiation in the Cu_2Sb compound. Only Matsuno et. al [14] and Sharma [15] started also a phase diagram investigation on the basis of their EMF measurements and theoretical calculations. Matsuno assumed a solid solution $CuLi_{2-x}Sb$ in the Cu-Li-Sb phase diagram (see Fig. 16a). He based his assumption on the observation of an increasing lattice parameter of the cubic $CuLi_2Sb$ phase during a coulometric titration with lithium. He also postulates another ternary compound with the composition CuLiSb which exhibits a half Heusler structure. He described this phase as an ordered arrangement between lithium and vacancies in the solid solution $CuLi_{2-x}Sb$. He also gave two possible structures of this phase (15, b,c), of which, on the basis of first principle density functional calculations, structure (C) is the most stable.

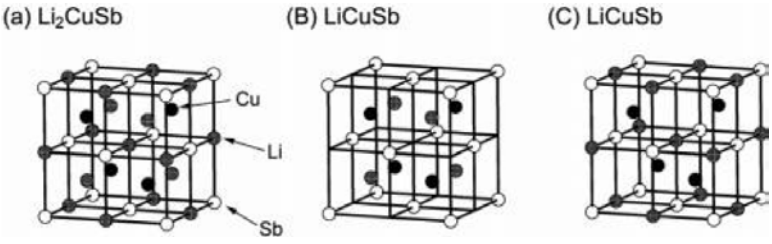

Fig. 15 The crystal structure of the ternary phase $CuLi_2Sb$ and the two possible structures of the postulated phase CuLiSb are shown. Structure c turned out to be the most stable one of the two [14].

Further calculations showed that the formation energies for $CuLi_{1.75}Sb$ and $CuLi_2Sb$ became positive against the three phase equilibrium region of Cu-$CuLi_{1.5}Sb$-Li_3Sb. Therefore Matsuno et al. [14] disregarded the experimentally synthesized ternary compound $CuLi_2Sb$ in their construction of the ternary phase diagram, as the calculations yielded that it would be thermodynamically unstable.

The following reactions are assumed to occur during lithiation [14]:

1. $Li + Cu_2Sb \rightarrow CuLiSb + Cu$
2. $Li + CuLiSb \rightarrow CuLi_{1+x}Sb$ $(0 \leq x \leq 0.5)$
3. $(2-x)Li + CuLi_{1+x}Sb \rightarrow Li_3Sb + Cu$ $(x \approx 0.5)$

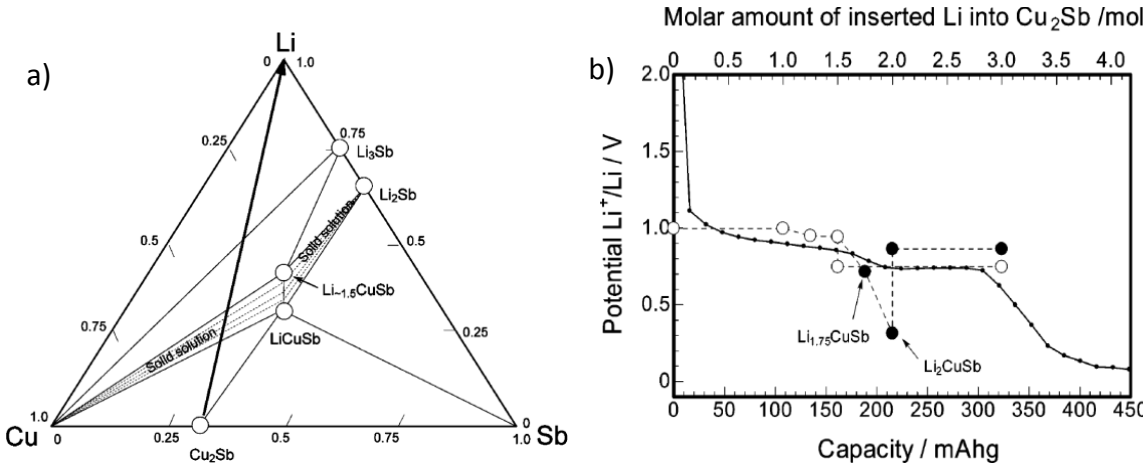

Fig. 16a, the ternary phase diagram constructed by Matsuno [14] is shown. Between the two ternary compounds $CuLi_{1.5}Sb$ and CuLiSb a solid solution is assumed. b, Experimental and calculated voltage for the coulometric titration of Cu_2Sb is shown. The solid line reflects the experimental data, whereas the opened and filled symbols are calculated voltages. The filled symbols show the reaction sequence: Cu_2Sb-CuLiSb-$CuLi_2Sb$-Li_3Sb, and the unfilled symbols show th reaction sequence: Cu_2Sb-CuLiSb-$CuLi_{1.5}Sb$-Li_3Sb [14].

Total energy calculations in the Cu-Li-Sb system were conducted also by Sharma et.al. [15]. They investigated the lithiation mechanism in Cu_2Sb. Two different reaction paths were described and compared, namely insertion/intercalation of lithium and substitution of copper by lithium. Depending on the lithiation mechanism, different reaction products are formed. To determine the dominant mechanism, the formation energies of the different compounds, which form during lithiation, were calculated. As shown in 17, the most stable compounds during the lithiation process of Cu_2Sb are: $Cu_2Li_{0.5}Sb$, $Cu_{1.5}LiSb$, $CuLi_2Sb$ and Li_3Sb. On the basis of these calculations, a lithiation mechanism of Li intercalation up to $Cu_2Li_{0.5}Sb$ and following Cu extrusion is postulated.

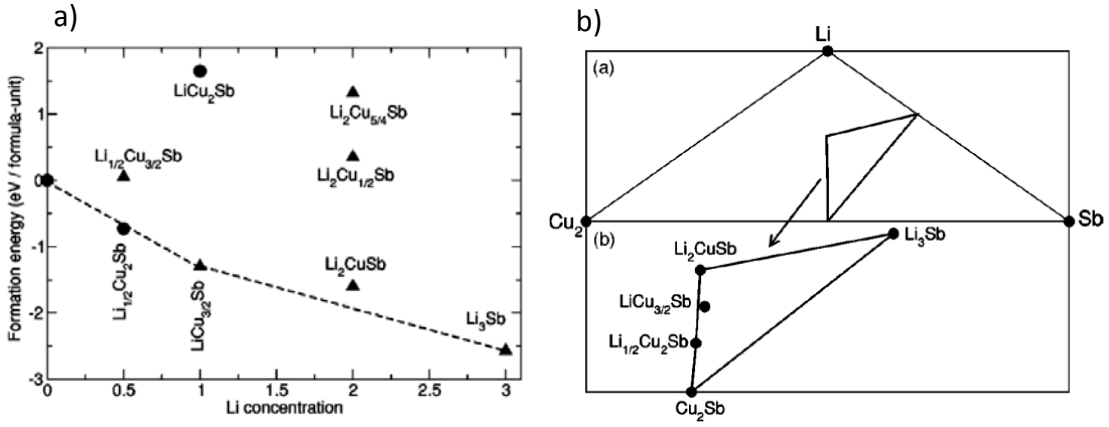

Fig. 17a, The formation energies for the compounds of the two different reaction paths (intercalation: circles, extrusion: triangles) is shown. The dashed line indicates the postulated reaction path of lithiation [15]. b, The results of the phase diagram investigation conducted by Sharma are shown. Cu is substituted by Cu_2 [15].

Apart from the theoretic calculations and the emf measurements, no experiments were conducted. Although it is crucial to confirm the actual existence of the postulated stable phases, formed upon lithiation, by experimental synthesis of these compounds, no such experiments were performed. Therefore it is unclear, whether the postulated phases really exist, or whether there are just metastable or nonexistent phases.

4. Sample preparation

4.1. General procedure

The elements Li and Sb were cleaned/purified before using them for sample preparation. A pure lithium wire (Alfa Aesar, 3.2mm, 99.8%, with oil coating) which is stored under argon (Ar) in a glovebox was used for all samples. Before usage, an appropriate amount was washed in n-hexane and dried on air for a few seconds, thereby getting rid of the oil coating. Then the wire was put back into the glovebox. There the first surface layers of the wire were peeled off, to get rid of already formed oxide layers.

Antimony (99.999%), was purified by filtering the molten metal through quartz glass wool under vacuum. First a quartz glass tube was closed at one end. At a distance of roughly ten centimeters, the tube was narrowed. Then the quartz glass wool was put into the tube in such a way, that it cannot go beyond the prepared neck. On top of the wool, a certain amount of Sb was placed. Then a vacuum of about 5-6*10^{-3}mbar was applied to the tube. After these preparations the actual purification process started:

- Melting Sb by heating the surrounding glass tube with an H_2/O_2 torch.
- Applying a pressure by passing Ar into the tube.
- The molten Sb is pressed through the quartz wool and the slags stay above.

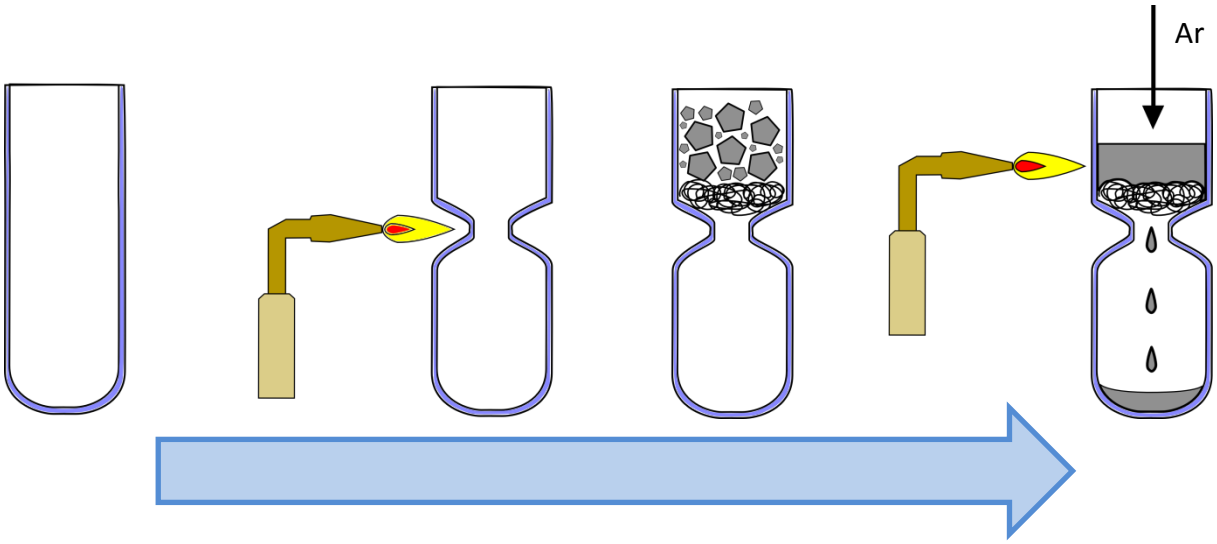

Fig. 18, Purification process for Sb. First a neck is created by heating a narrow region of an evacuated silica tube. Then silica wool is placed onto the neck. Sb is inserted into the tube and melted with an oxyhydrogen torch. Ar is inserted into the tube to create enough pressure to press Sb through the quartz wool.

For the prepared samples, corresponding amounts of the purified elements were weighed on a balance with an accuracy of ±0.1mg. As lithium is easily oxidized on air, all steps which contained handling of lithium, were conducted in a glovebox under argon atmosphere.

Sample preparation started by weighing corresponding amounts of the metals, and putting them into a crucible. If tantalum crucibles were used, they were closed gas tight, by sealing them in an arc furnace. Ceramic crucibles were in general not closed, except some of the boron nitride (BN) crucibles which had corresponding lids. All crucibles were sealed in silica glass under vacuum (about $5\text{-}6*10^{-3}$mbar) to avoid oxidation of the samples and/or crucible materials during the melting or annealing steps.

The samples were melted in a resistance furnace (ceramic crucibles) or induction furnace (tantalum crucibles). When the induction furnace was used, the samples were heated to a certain temperature and immediately cooled afterwards. This was done three times and to ensure proper mixing of the compounds, the used crucibles were rotated by 180° after each heating cycle.

When the resistance furnace was used, the samples were put into the furnace at the melting temperature for about 1.5 hours. After every 30min, the samples were shaken to ensure mixing of the compounds.

After melting of the samples, the respective heat treatment in a resistance furnace followed.

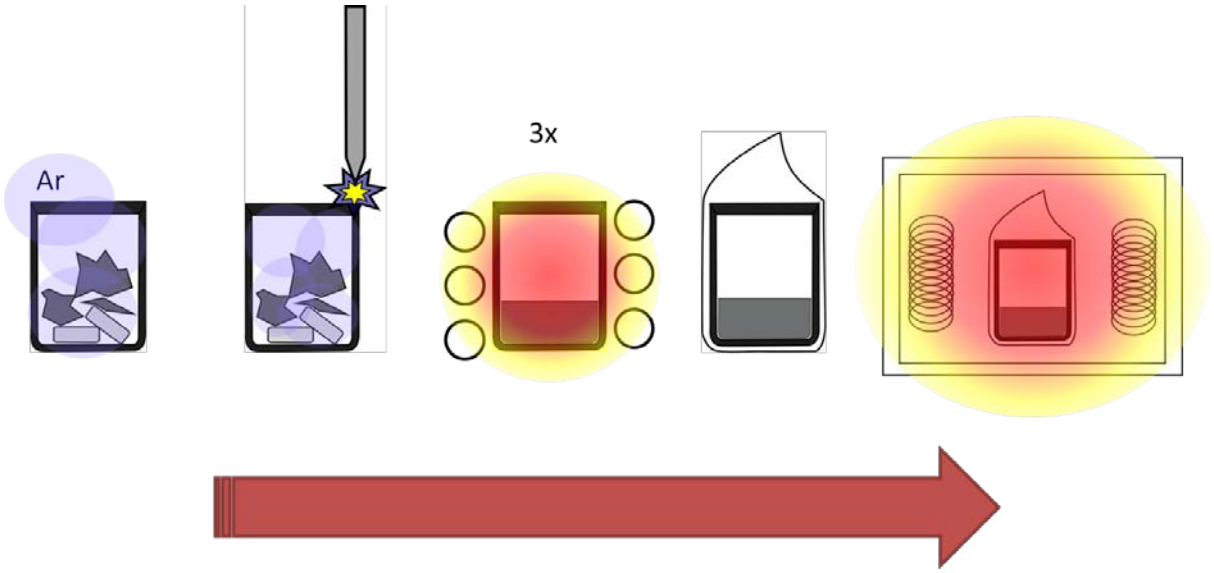

Fig. 19, Visualization of the sample preparation in tantalum crucibles.

4.2. Crucible materials

A major task in this work was the search for a proper crucible material, which can be used for sample preparation. As lithium and antimony are both very reactive metals, the search for an inert crucible material is not at all a trivial matter. A suitable material has to have the following properties:

- No reaction with lithium at temperatures up to 1300°C.
- No reaction with antimony at temperatures up to 1300°C.
- Sealable (gas-tight)
- No diffusion of lithium through the material.
- Not too expensive (because many samples have to be prepared)

Many metallic crucibles used by other research groups, which use lithium in their experiments, cannot be applied to this system. Iron, which is stable against Li, was used by Brauer et. al. [17] to conduct experiments in the binary Li-Sb system. However, they reported that during heat treatment, Sb readily reacts with iron. Molybdenum, which was used in studies concerning the Li-Cu system [26], also forms binary compounds with Sb. The only metal, which is stable against both, lithium and antimony, is tungsten. Although, not much experimental investigations were conducted in the respective systems [30, 31], it seems that no binary compounds of tungsten with Sb or Li exist. However, tungsten is a very expensive material, as it is difficult to work with. It might also not be possible to seal tungsten crucibles in an arc furnace, as the melting point of tungsten is too high.
Silica, which can be used for preparation of Sb alloys [30, 31], is reduced by lithium and thus cannot be used for sample preparation in the present system.

4.2.1. Tantalum crucibles

At first it was decided to use tantalum crucibles for the samples in the binary system, as well as for the ones in the ternary system. Tantalum is stable up to over 3000°C, therefore it is no problem to melt the samples (T_{max} = 1300°C) in this material. Lithium does not show a reaction with tantalum, however it is able to diffuse through the grain boundaries of the tantalum walls at higher temperatures. This phenomenon is indicated by a brownish 0discoloring of the surrounding silica tube in which the tantalum crucible is

enclosed. It is assumed, that lithium reduces the silicon dioxide, yielding brown silicon monoxide. Although this is unfavorable, it happens only to a small extent and in most cases the loss of lithium is negligible. There is however another drawback regarding the use of tantalum as a crucible material for the Li-Sb system, namely its reaction with antimony. Already in 1965, Furuseth et. al. [32] found three binary compounds in the Sb-Ta system, Sb_2Ta, Sb_4Ta_5 and $SbTa_3$. Therefore the possibility of Sb reacting with the tantalum crucible during the melting and annealing steps of the sample preparation was very high. However Ta crucibles were still used, because it was assumed, that Ta shows a certain kinetic stability towards Sb, especially at low temperatures (ca. 800°C). The basis for this assumption were experiments conducted in the Li-Sn system, which showed a likewise behavior [33]. Tantalum forms three binary compounds with Sn: Sn_3Ta_2, Sn_2Ta_3 and $SnTa_3$ [34]. However Henriques et.al. [33] did not observe any reaction occurring between the samples and the crucible walls. Therefore Sn has to have a certain kinetic stability towards tantalum. And as Sb is right next to Sn in the periodic table and shows a similar chemical behavior, the assumption that also Sb might exhibit a kinetic stability was justified. Unfortunately, the first conducted experiments disproved this assumption as binary Sb-Ta phases were found in samples with higher Sb contents. (see *6. Results and Discussion*).

Fig. 20, Ta crucible for sample preparation.

As no suitable metallic crucibles were found for the entire Li-Sb system, the focus shifted towards ceramic materials.

4.2.2. Ceramic crucibles

Ceramic materials exhibit a high chemical resistivity and are stable up to high temperatures. Therefore they seem to be proper materials for sample preparation in the Li-Sb system. However they lack one important property; they cannot be easily sealed gas-tight. Nonetheless three different ceramics were tested in parallel: alumina, magnesia and boron nitride.

4.2.2.1. Alumina crucibles

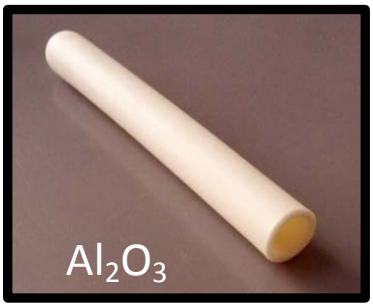

Fig. 21, Alumina crucible for sample preparation.

Already in 1985, Konys and Borgstedt [35] conducted experiments regarding the reaction between Li and aluminum oxide, Al_2O_3. They found, that alumina is not compatible with Li, because ternary oxides are likely to be formed upon heating.

Nevertheless, alumina crucibles were tested for sample preparation, because it was unknown, whether lithium reacts preferentially with antimony or Al_2O_3. It could be possible, that lithium reacts quickly with antimony, forming the intermetallic alloy and therefore does not react with alumina.

The pretreatment for alumina crucibles was as follows. About 6cm long crucibles were cut to an appropriate length (about 3cm) with a diamond circular saw. Then they were cleaned with acetone and dried on air. Finally they were heated with a Bunsen burner until they glowed red. The samples were then put into the crucible and encapsulated in silica glass under vacuum. The findings of Konys and Borgstedt [35] were confirmed in the course of our experiments. After the heat treatment of the samples, a black layer could be observed between the crucible material and the sample itself (see Fig 19a). This layer of mixed oxides however was very thin. Therefore it was assumed, that the sample composition shifted only slightly towards lower lithium concentrations. It was expected, that this deviation from the nominal concentration is small and can be quantified by atomic absorption spectroscopy. (see *4.4. AAS samples*).

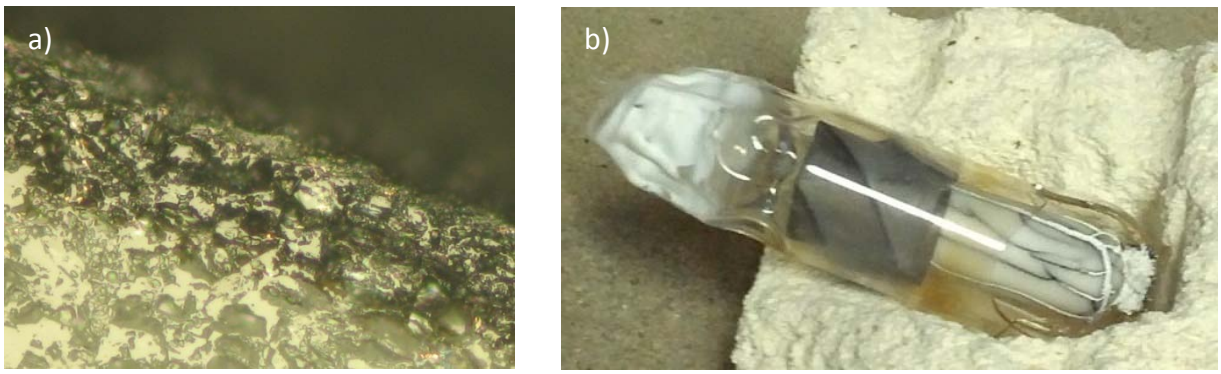

Fig 22a, mixed oxide layer formed on an alumina crucible due to reaction with lithium; b, lithium diffused through tiny cracks in the crucible and reacted with the silica tube. After the silica tube broke, the lithium immediately oxidized (white powder at the bottom).

Another important point encountered during the sample preparation with alumina crucibles was, that it is crucial, that the crucibles are free of any cracks. Lithium can easily diffuse through these cracks out of the crucible. It then attacks the silica tube, which corrodes and breaks. After air gets into the tube, lithium oxidizes and due to the greater volume of the oxides, the crucible gets even more cracks. Not once a sample preparation failed because of tiny cracks in the crucibles, which were not visible with the naked eye.

4.2.2.2. Magnesia crucibles

The second ceramic material tested, was magnesia. At first crucibles which were purchased from Morgan Refractories were used. The MgO crucibles were pre-cleaned with deionized water and acetone and afterwards they were heated with a Bunsen burner until they glowed red. Then the respective amount of lithium and antimony was put into the crucible and everything was sealed in quartz glass. The crucibles were open in the quartz glass ampoule. The sample was then melted at 800°C and annealed at the respective temperature (500°C/400°C).

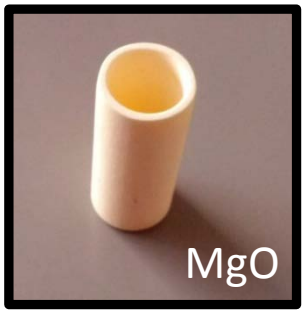

Fig. 23, Magnesia crucible for sample preparation.

However during the annealing process of the first sample, which was prepared in a magnesia crucible, the silica tube corroded and broke. A closer look at the crucible after this incident revealed the reason why this happened. Apparently the porosity of the crucible material was too high. Lithium was able to diffuse through the pores of the crucible material to the quartz glass and reacted with it. The quartz glass got thinner and broke. It could also be observed that even Sb was able to settle in the pores of the ceramic material. Ceramics made from MgO-powder are first pressed into a certain shape and then sintered by applying pressure and high temperatures. The products produced in such a way exhibit a certain porosity, which varies from a few percent to 20% or even more. As the datasheet for the used crucibles


Fig. 24, A part of the magnesia crucibles purchased from Morgan Refractories; the black material which penetrated the crucible is antimony, which settled in the pores of the material.

was not available, it was estimated that the porosity of the used crucibles was more than 10%.

After this incident it was evident, that MgO crucibles only with low porosity are suitable for sample preparation. That's why new crucibles were ordered by Ozark Technical Ceramics, Inc. with an open porosity of less than 1%. Lithium was not able to diffuse through the walls of these crucibles. There was also no reaction of the sample with the crucible material.

4.2.2.3. Boron nitride crucibles

As MgO and Al_2O_3 did not yield satisfying results, also boron nitride (BN) crucibles were tested for sample preparation. BN exhibits the same structure as graphite. Therefore it is often suggested, that Li might also be able to intercalate into this material. However theoretical calculations [36] assume that it is not energetically favorable for Li to intercalate into h-BN. The dislocated electrons in carbon seem to be necessary to stabilize the Li-ions in the hexagonal layers. Therefore at atmospheric pressure intercalation should not be observed.

Fig. 25, Boron nitride crucible for sample preparation.

Before using the BN crucibles, they were placed in methanol for three days, to get rid of boric acid, which forms on the surface of the material. Methanol forms a volatile ester with boric acid [37], which can then be evaporated by heating the crucibles under vacuum to 800°C.

$$B(OH)_3 + 3CH_3OH \rightarrow B(OCH_3)_3 + 3H_2O \qquad (8)$$

At first, open BN crucibles were used. Samples melted and annealed in these crucibles showed no reaction with the crucible material. Despite of this, some of the samples stuck at the crucible walls and could not be completely removed. In XRPD measurements of these samples, BN is clearly visible. This problem however, was not always observed and does not influence further measurements. Later, also BN crucibles with lids were tested. They were sealed in quartz glass as shown in Fig 23. A silica glass rod was placed onto the crucible during the sealing process. The rod should ensure that the lid of the crucible is

tightly closed and that it won't open up again during the annealing or the melting step. Due to the high vapor pressure of lithium and antimony at higher temperatures, the lid could easily be lifted because of the evolving pressure inside the crucible. The silica glass rod serves as a kind of counter force, pressing against the lid so that it stays closed (see 26). Some quartz glass wool was placed at the bottom of the crucible, in order to prevent the occurrence of too much mechanical stress due to the different thermal expansion coefficients of silica glass and BN.

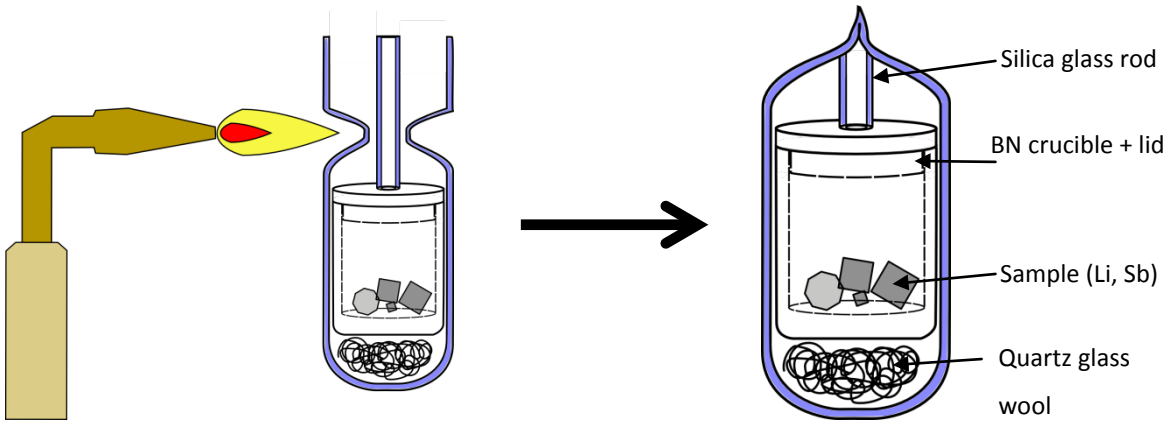

Fig. 26, The sealing process of BN crucibles with lids. The glass rod ensures that the lids won't open up during heat treatment.

The BN crucibles which were closed with a lid, showed very good results in respect to sample preparation. First of all the BN is inert to the sample materials, therefore no side reactions occur. Also it seems that due to the lid, most of the antimony vapor is inhibited to leave the crucible. Almost no antimony was observed outside the BN crucible after 41 days of annealing at 400°C. However, the crucible, which is white before the heat treatment of the sample, grew a little grey after the annealing process. Therefore further investigations have to be conducted, to find out whether antimony still gets out of the crucible and if so, how much antimony is lost during the heating steps of the sample preparation. Still, up until now, this method seems to be the most promising one, for future sample preparations. It will find use not only in the binary system, but also for the antimony rich side of the ternary system Cu-Li-Sb.

4.2.2.4. Unsolved problems regarding ceramic crucibles

The major drawback in regard of ceramic crucibles is their lack to be sealable gas tight. If open ceramic crucibles are used however, lithium and antimony vapor can freely extend

into the silica ampoule. Lithium, which melts at 180°C, reacts very fast with antimony and therefore only a little amount is able to get out of the crucible. However the little amount of lithium reaching the silica glass reacts with it and this leads in the worst case to cracks in the glass ampoule. The bigger problem however is antimony. After melting of the sample (temperatures up to 800°C are reached), the furnace cools down to the annealing temperature (400°C or 500°C). The layered structure of the sample (glass ampoule → crucible → sample) leads to a temperature gradient within the glass ampoule. Therefore, antimony vapor within the sample condenses preferentially on the cooler silica walls. As more and more antimony is drawn out of the sample, tiny crystallites are formed, which rapidly grow bigger. After the annealing step, the crystallites have already formed single crystals, which weigh up to 29mg. To quantify the loss of antimony in the sample, an analytical tool like AAS has to be used. Therefore it is not only necessary to determine the Li content of the samples (alumina samples) but also the antimony content. However an antimony lamp for the AAS instrument was not available during the course of this work.
A possible way to solve the problem of antimony evasion might be the use of ceramic adhesives. Suitable lids for the different ceramic crucibles can be attached with such pastes. However, the ceramic adhesive has to exhibit very specific properties.

- gas tight
- resistant to high temperatures
- hardening should take place at room temperature or at max. 100°C
- very small thermal expansion coefficient

It is difficult to find adhesives with these properties, but there are a few, which will be probably tested in the near future.

4.2.3. Hybrid solutions

In addition to Ta and ceramic crucibles, also hybrid solutions were tested. Two different approaches are shown in Fig. 27.

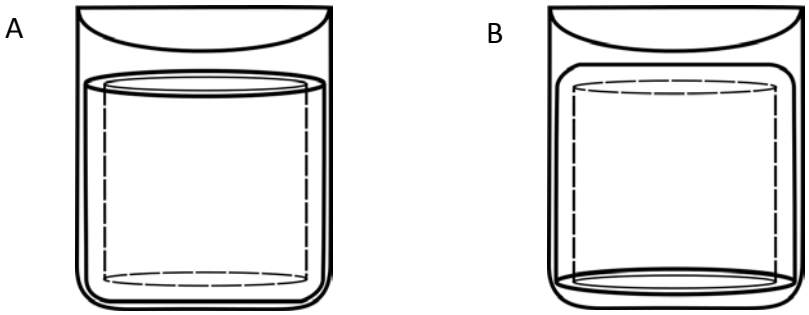

Fig. 27, The two hybrid solutions are shown. A BN inlet is placed into a Ta crucible (A); a BN inlet is placed upside down into a Ta crucible (B).

The first idea was to use a BN inlet for the Ta-crucibles to prevent physical contact of the sample with the Ta walls. This approach was used for DTA measurements and showed good results. No Sb-Ta compound was found in the sample. When the crucible was opened however, it was observed that Sb was deposited onto the lid and Ta-walls around the lid. There antimony vapor could have reacted with the crucible material without getting noticed. Therefore another approach was tested. The BN inlet was inverted and imposed on the sample. The idea behind this approach was that maybe only the antimony vapor reacts with the Ta walls but not the melt. The BN inlet fits quite well into the Ta-crucible, so that there is almost no space in between. When the sample inside the BN inlet melts, it seals off the floor of the crucible and the vapor is only able to extend into the space confined by the BN inlet. Thereby a reaction between the antimony vapor and the Ta crucible is inhibited. The sample which was prepared in this way (Li25Sb75_BNinv_400) showed no Sb-Ta compounds in the diffraction pattern after 55 days of annealing at 400°C, thereby confirming the assumption that only the antimony vapor reacts with the Ta crucible.

This approach is not only suitable for sample preparation, but also might enhance the sensitivity of the DTA measurements. Until now, the best solution for DTA measurements was the use of a BN inlet as shown in Fig.27(A). However the sensitivity is reduced due to the insulating effects of the BN inlet. By turning the inlet upside-down, the opening of the inlet faces the bottom of the crucible. Therefore, no reduction of the sensitivity should take place. This will be tested in the near future.

A little drawback of the hybrid solutions is the small volume available for the sample. Therefore only little amount of a sample can be prepared. That is why the hybrid solutions will essentially be used for DTA measurements.

A short summary of the used crucible materials and comments about their advantages and disadvantages is shown in table 4.

Table 4, Summary of the different crucible materials used.

Method	Advantages	Disadvantages	comments
Ta crucible/ heat treatment in resistance furnace	Precise temperature control	SbTa compounds form in samples with higher Sb-content, if heat treatment at high temperatures is too long.	Suited for annealing samples
Ta crucible/ heat treatment in induction furnace	Fast melting of the sample and therefore smaller probability of SbTa compounds to form	Temperature control is limited	Suited for melting samples
Ta crucible+BNinlet without lid	No direct reaction with crucible material	BN may adhere onto the sample; vapor of the sample might react with the crucible; small sample volume.	suited for DTA measurements
Ta crucible+BNinlet with lid	No significant difference to BNinlet without a lid, as the antimony vapor easily diffuses out of the inlet through the small crack between lid and inlet.		suited for DTA measurements
Ta crucible + BN inlet without lid (opening faces bottom of Ta crucible)	Sb reacts with Ta only via gas phase; therefore no reaction with the crucible material takes place.	Small sample volume.	Suited for DTA; higher sensitivity
Alumina/ heat treatment in resistance furnace	No reaction of Sb with crucible material.	Samples cannot be sealed. Therefore Sb as well as Li may get out of sample. Li reacts with alumina, thereby altering the sample composition.	Effective sample composition has to be determined by AAS or other analytical methods.
BN-crucible with lid/ heat treatment in resistance furnace	No reaction with crucible material; crucible lid reduces vapor pressure of Sb.	BN may adhere onto the sample	If the crucible is closed tightly, almost no antimony is able to escape.
MgO-crucible/ resistance furnace	No reaction with crucible material.	No lid and therefore Sb escaping from the crucible.	Porosity of crucible material has to be very low.

4.3. Aspects regarding ternary samples

All ternary samples were prepared in Ta crucibles. In order to avoid a reaction of antimony with the crucible material, antimony-copper alloys were prepared. This was supposed to reduce the activity of antimony and thereby inhibit a reaction with the crucible material. The alloys were prepared by melting the corresponding amounts of antimony and copper in a silica tube at 1000°C. The silica tube was sealed under vacuum before heat treatment, to prohibit oxidation of the materials. The so produced alloys were used as master alloys for sample preparation in the ternary system.

The ternary samples were prepared by mixing corresponding amounts of the antimony-copper master alloys with lithium in a tantalum crucible. The crucible was closed by welding a lid onto it in an arc furnace. Then the sample was melted three times in an induction furnace at 800°C. After each time of melting, the sample was rotated by 180° to ensure thorough mixing of the compounds. Finally the crucible with the already melted sample was sealed in a silica tube under vacuum. Then annealing in a resistance furnace started. Although all these procedures were performed with great care, some of the annealed samples still exhibited Sb-Ta compounds to a certain extent. Therefore it will be necessary to use a hybrid approach, as discussed above or ceramic crucibles in the antimony rich region of the ternary phase diagram.

4.4. AAS samples

To determine the total loss of lithium due to reactions with alumina, AAS was used. A total of three samples, plus two reference solutions were analyzed. Each sample was crushed and three appropriate parts were picked for the analysis. The weight of the parts had to be in accord with the optimal lithium concentration of the final solutions. The final lithium concentration should not exceed 2.5mg/l, because of the limited scope of application of the Lambert-Beer law.

First, the parts were weighed under argon atmosphere on a micro balance. The accuracy of the scale was about ±0.005mg. Then the parts were dissolved in 2ml aqua regia. After that, 4ml tartaric acid (1mol/l) was added to confine antimony in an antimony tartrate complex. This is necessary to prohibit the precipitation of antimony oxide during the addition of water.

All solutions were diluted with deionized water until a volume of 50ml was reached. The solutions prepared in such a way were again diluted before the measurements to reach a lithium concentration of about 2mg/l. For the two reference solutions, about 7mg of pure lithium was solved in 2ml of deionized water. Then 2ml aqua regia was added. Only one of the two solutions was also mixed with 4ml tartaric acid. Then both solutions were diluted to 50ml with deionized water. Again they were diluted even further for the measurements.

The reference solutions were prepared in order to determine how accurate the measurements are. The one with tartaric acid should ensure that the addition of this reagent does not influence the outcome of the measurements.

The results of the analysis are shown in the table 5. The reference samples showed that the difference between the nominal and the measured amount of lithium is about 0.3mg. This amount of Li is lost during reference sample preparation, or could not be detected by the AAS instrument due to ionization or self-absorption. For both reference solutions the loss of lithium is the same, indicating that the addition of tartaric acid does not influence the measurement in any kind.

Table 5, Results of the AAS measurements of the samples Li20Sb80_AlOx_500, Li50Sb50_AlOx_500, Li70Sb30_AlOx_500.

Nr	Sample	Nominal amount of Li in the sample [mg]	Measured amount of Li in the sample [mg]	Difference [mg]
1	Li	7.01	6.71	0.31
2	Li without tartaric acid	7.03	6.70	0.33
3	Li20Sb80_AlOx_500_A	15.01	23.81	-8.80
4	Li20Sb80_AlOx_500_B	15.01	14.74	0.27
5	Li20Sb80_AlOx_500_C	15.01	15.88	-0.87
6	Li50Sb50_AlOx_500_A	48.04	31.45	16.59
7	Li50Sb50_AlOx_500_B	48.04	32.89	15.15
8	Li50Sb50_AlOx_500_C	48.04	31.19	16.85
9	Li70Sb30_AlOx_500_A	48.1	45.39	2.71
10	Li70Sb30_AlOx_500_B	48.1	41.03	7.07
11	Li70Sb30_AlOx_500_C	48.1	42.15	5.95

The results of the AAS measurements are difficult to evaluate. The three samples, which were measured, differ significantly in their lithium concentration. In reference to Le Chatelier's principle, it is expected that the sample with the highest lithium content will also show the highest loss of lithium, due to reactions with the alumina crucible. Le Chatelier's principle states that a chemical system in equilibrium which is exposed to a disturbance

(change in pressure, temperature, concentration, etc.) will tend to minimize the effects of the disturbance and a new equilibrium is established [38]. Therefore the chemical equilibrium between the educts lithium and alumina and the mixed oxides they form, will be shifted towards the mixed oxides upon increase of the lithium content.

$$Li + Al_2O_3 \leftrightarrow mixed\ oxides \qquad (9)$$

However the sample with the highest lithium loss is Li50Sb50_AlOx_500. About 16mg of lithium, which is one third of the whole lithium content in this sample, was lost. This is a quite high value, especially in relation to the sample with the highest lithium concentration, Li70Sb30_AlOx_500, which showed a lithium loss of just 5mg. The sample Li20Sb80_AlOx_500 showed almost no loss of lithium. Therefore it can be concluded, that not only the initial concentration of the samples determines the loss of lithium, but also other factors play a role (e.g. the properties of the crucible).

Apart from the unusual high lithium loss in the sample Li50Sb50_AlOx_500, another result of the AAS measurements needs some discussion. For two parts of the sample Li20Sb80_AlOx_500, the measurements yielded a higher Li content than the nominal one. A simple reason for this is that the sample was inhomogeneous. Therefore there are lithium rich and lithium poor parts. By coincidence, a part with a very high lithium concentration was used for one measurement. The other samples show inhomogeneity in respect to the lithium concentration too. However there is another explanation for the higher than expected lithium content in the sample Li20Sb80_AlOx_500. During the melting and annealing steps of the sample preparation process, antimony vapor is formed, which condenses onto the outer walls of the crucible, as well as onto the silica tube which conceals the whole sample. Thereby the antimony content of the sample decreases and the relative amount of lithium increases, resulting in a higher Li concentration than the nominal one.

The AAS measurements showed that it is possible to determine the loss of lithium due to reactions with the alumina crucibles. However, losses of lithium during solving of the samples for the measurements and the inherent inhomogeneity of the samples themselves make the measured values quite inaccurate. If both the lithium content of the sample as well as the antimony content can be measured, the relative composition of the whole sample can be determined. This approach might yield better results for the analysis of the prepared samples.

5. Experimental methods

5.1. X-ray Diffraction

5.1.1. Production of X-rays.

X-rays are high energetic electromagnetic waves, with wavelengths ranging from 10 to 0.001nm [39]. The most common way to produce X-ray radiation is by means of an x-ray tube shown in Fig. 28. A high voltage (several kV) is applied between two metal electrodes. Due to the large potential difference, electrons are emitted from the cathode and accelerated towards the anode. The emission of electrons is facilitated by heating the cathode material. The electrons collide with the respective anode material and lose their kinetic energy, producing X-ray radiation (less than 1%) and heat [40]. Since most of the electrons energy is dissipated as heat, the anode has to be cooled. An X-ray spectrum produced in such a manner shows two kinds of radiation, a continuous part called white radiation and a discrete part called characteristic radiation.

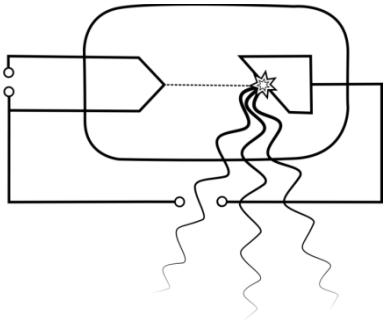

Fig. 28, An x-ray tube, consists of an anode, a cathode and a concealing glass tube.

The white radiation is produced by the slowdown of the electrons due to interactions with the electron clouds of the nuclei of the anode material. As different electrons take different paths in the course of their interaction with the anode material (Fig. 29), the resulting X-ray energies are different, yielding a continuous spectrum. The maximal energy of the white radiation is limited by the initial kinetic energy of the electrons and therefore by the applied voltage between the two electrodes [40]. The discrete part of the emitted radiation superimposes the white radiation and is derived from a totally different process. Electrons, which have kinetic energies, higher than a certain threshold value, are able to excite near-shell electrons at the anode material, and create thereby electron holes. These holes are on their part filled with electrons from higher

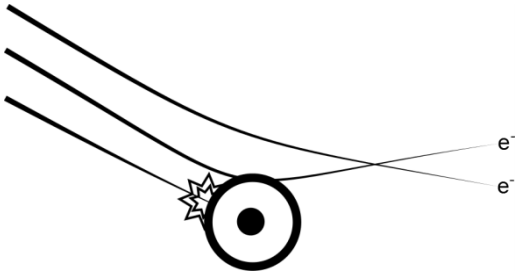

Fig. 29, Electrons interact differently with the electron cloud of atoms from the anode. Therefore they all loose a different amount of their kinetic energy.

shells of the respective atoms. During this relaxation process, energy is emitted as X-rays with discrete energy values. Depending on which shells are involved in the relaxation process, we speak of K_{alpha}-, K_{beta}-, L_{alpha}-, … -radiation (see Fig. 30).

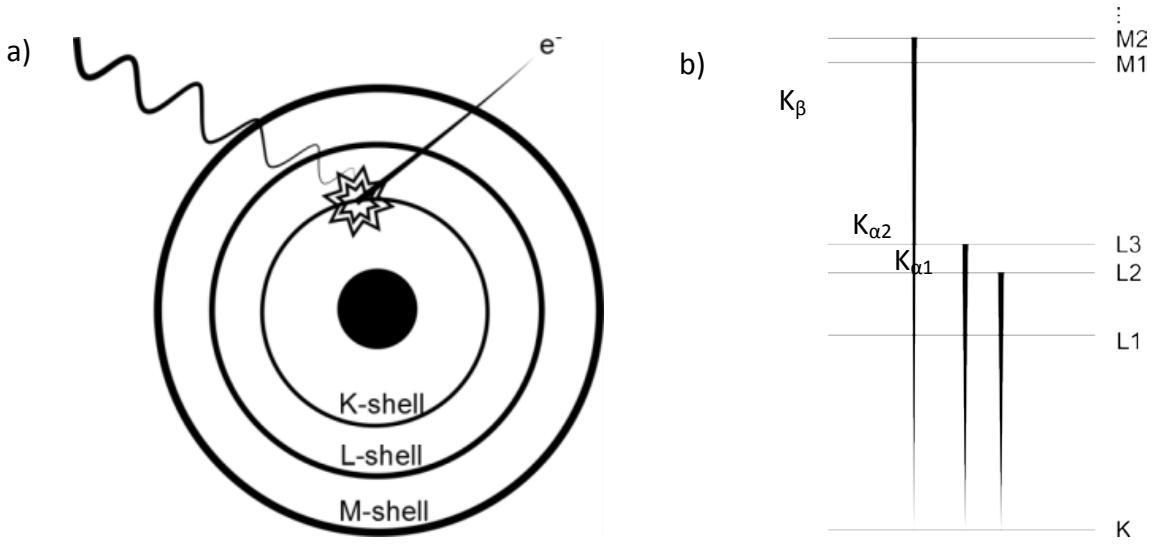

Fig. 30a, excitation of a near shell electron and following; b, possible relaxation processes.

The relaxation process is restricted to certain selection rules, which are

Table 6, Rules for relaxation processes.

Quantum numbers	Allowed values
Δn	anything
Δl	±1
Δj	0 or ±1

where Δn, Δl and Δj stand for the change in the principal, azimuthal and total angular momentum quantum numbers during the relaxation. Therefore some electron transitions are forbidden, e.g. the $L_l \rightarrow K$ transition, where Δl = 0 [40].

5.1.2. X-ray diffraction

X-rays are a kind of electromagnetic radiation and therefore can be elastically scattered by electrons. The electron shell of an atom is therefore able to scatter incoming X-rays into all directions and thus the atom can be considered as scattering center. If more atoms are aligned in an array, it is not possible anymore to observe the diffracted light at all directions.

This is due to interference effects, which occur upon interaction of the different diffracted beams with each other.

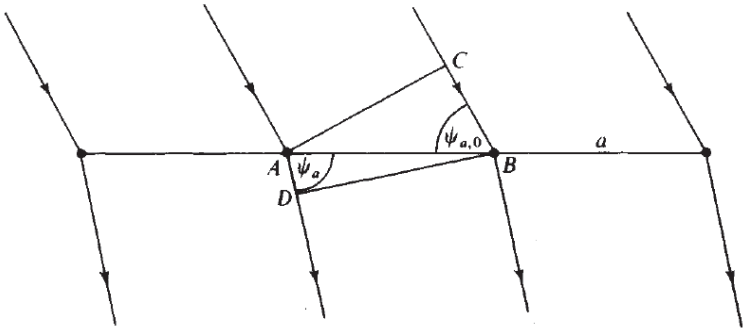

Fig. 31, Depiction of the geometrical aspects of the scattering process [41].

Fig 28 depicts the situation for an array of atoms. The incoming X-rays with incident angle $\psi_{a,0}$ are diffracted at the electron shell of the atoms and propagate afterwards in the direction of the angle ψ_a. For two X-rays which are diffracted at the atoms A and B to show positive interference, the following equation has to be fulfilled:

$$CB - AD = h\lambda \qquad (10) \text{ or}$$

$$a\left(cos\psi_a - \cos\psi_{a,0}\right) = h\lambda \qquad (11)$$

The additional distance (CB-AD), which the incoming radiation diffracted at atom B has to travel (in contrast to the one diffracted at atom A), has to be equal to the wavelength λ times an integer h. The incident radiation is not necessarily coplanar and therefore a distinct angle of incidence $\psi_{a,0}$ and integer h defines a diffraction angle ψ_a which yields a radiation cone with semi-angle ψ_a [41].

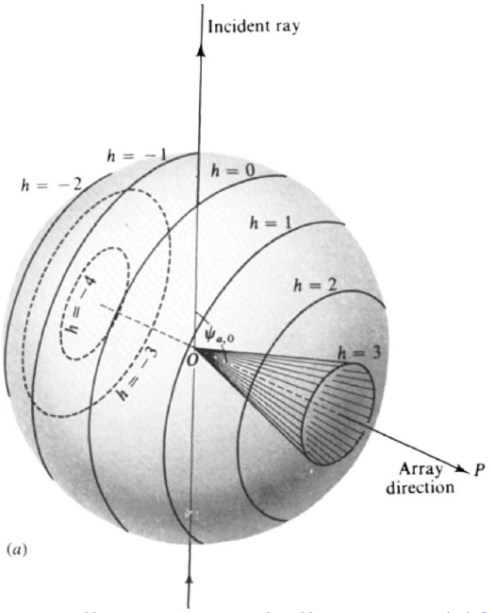

Fig. 32, diffraction cones of different order (h) [41].

In a crystal lattice, the periodically distributed electron density distributed in three dimensions, leads to corresponding three equations, which have to be fulfilled to obtain positive interference. It was Friedrich von Laue, who discovered this phenomenon in 1912 [42] and therefore the equations are called Laue equations.

$$a\left(cos\psi_a - \cos\psi_{a,0}\right) = h\lambda \quad (12)$$

$$b\left(cos\psi_b - \cos\psi_{b,0}\right) = k\lambda \quad (13)$$

$$c\left(cos\psi_c - \cos\psi_{c,0}\right) = l\lambda \quad (14) \quad [41]$$

The equations correspond to the three crystallographic axes (a, b, c) of the crystal. Only if all equations are true, positive interference occurs [43]. The three Laue equations correspond to different diffraction cones, which intersect. Only if three cones, corresponding to the three axes a, b and c intersect in one point, constructive interference occurs.

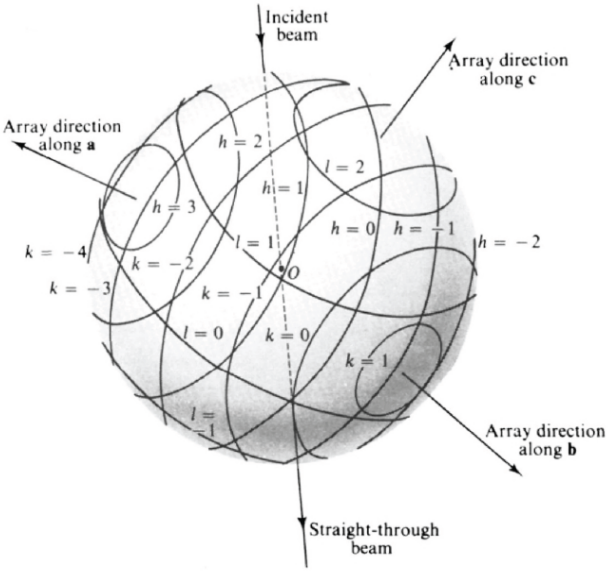

Fig. 33, The three Laue equations depicted as diffraction cones along the three different axis a, b and c [41].

W.L. Bragg proposed a different, much easier way to calculate the interference pattern of X-rays diffracted by a crystal lattice. He reduced the crystal lattice to parallel planes, on which the X-rays are partially reflected. By geometric means, he deduced an equation much simpler than the Laue equations, though yielding the same solution.

$$2d_{hkl}sin\theta_{hkl} = n\lambda \quad (15)$$

Bragg's equation states that for a certain lattice plane hkl, with an interplanar distance d, only at an angle θ, there is positive interference. If the angle θ is only slightly off, negative interference, i.e. extinction occurs [41].

5.1.3. Miller indices

The lattice planes in a unit cell of a crystal are characterized by the so called Miller indices h, k and l. The Miller indices are the reciprocal intercepts of the crystallographic axes [43]. Each lattice plane has its own d spacing between neighboring planes. The Miller indices are constructed in the following way:

1. Look for the plane next to the one which goes through the zero point.
2. Note the intercepts to the crystallographic axes of this plane.
3. Take the reciprocal fraction of these values which yield the Miller indices [43].

As most planes have their own d spacing, according to Bragg's equation, they all yield constructive interference at a different angle θ. This is the basis of structure determination by X-ray diffraction.

An X-ray diffraction pattern shows the angles θ at which different lattice planes show positive interference. If the wavelength of the X-rays is known, one can easily calculate the respective d values. The d values give information about the geometry of the unit cell. E.g. for cubic systems, the following equation holds,

$$\frac{1}{d^2} = \frac{h^2+k^2+l^2}{a^2} \qquad (16)$$

Therefore if we know d and the corresponding Miller indices, we can calculate the lattice parameter a.

Additional information about the Bravais lattice of the system is obtained due to the so called extinction rules. These rules state, that if a certain Bravais lattice is present some planes, which would normally show constructive interference according to the Bragg equation, show extinction of the X-rays [43].

5.1.4. Atomic scattering factor

Scattering of X-rays occurs by adsorption and reemission of the incident radiation by electrons. In atoms other than hydrogen, the incoming radiation is scattered by several electrons, leading to interference of the scattered radiation. Whether the scattered radiation of the electrons is in phase or out of phase depends on the angle of emission. The efficiency of scattering of one atom, is defined by the atomic scattering factor f,

$$f = \frac{amplitude\ of\ wave\ scattered\ by\ an\ atom}{amplitude\ of\ wave\ scattered\ by\ a\ single\ electron} \qquad (17)$$

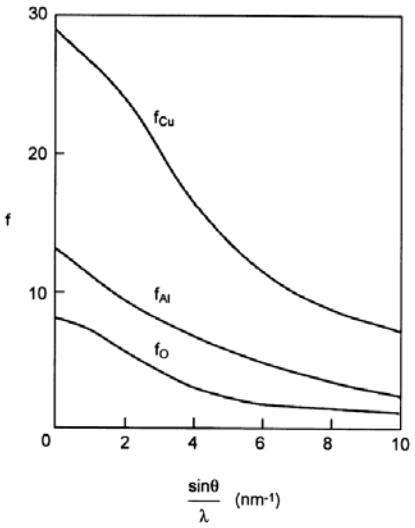

Fig. 34, Dependence of the atomic scattering factor on the scattering angle θ [41].

which is a function of the incident wavelength λ and the scattering angle θ [40]. For θ= 0, the atomic scattering factor yields the atomic number of the respective atom. To illustrate the angle and wavelength dependence of the atomic scattering factor, it is often plotted against sin(θ)/λ, as shown in Fig. 34.

5.1.5. Structure factor

A crystal lattice is composed of more than one atom. Therefore it is not sufficient to describe the scattering behavior of just one, but rather you have to look at scattering and interference of all atoms, or at least of the atoms in the unit cell. The structure factor describes the influence of the crystal lattice to the diffracted radiation [40] and is defined by the following equation:

$$F_{hkl} = \sum_i f_i e^{2\pi i(hx_i+ky_i+lz_i)} \qquad (18) \quad [44]$$

F is the structure factor, f_i the atomic scattering factor, x_i, y_i and z_i indicate the position of the atom in the unit cell and h, k and l are the Miller indices of the respective diffraction line [40].

The observed intensity of the diffracted radiation is proportional to the square of the structure factor.

$$I \propto F^2 \qquad (19)$$

This relation is the reason for a major drawback regarding structure analysis by X-ray diffraction, the so called **phase problem**. As the intensity I is proportional to F^2, the information about the phase incorporated in the complex term of F is lost. As only the intensity of the diffracted radiation can be detected, the phase angles have to be determined by means of more sophisticated methods (direct methods, Patterson etc.) [40].

5.2. Single crystal X-ray diffraction

Single crystal X-ray diffraction is a potent method for structure analysis, which uses X-ray diffraction to determine the crystal structure of single crystals. A single crystal is mounted on the head of a goniometer, which is able to rotate the crystal around three axes. The crystal gets irradiated with X-rays and diffraction occurs. In order to obtain diffraction peaks for all hkl planes, it is necessary to rotate the crystal according to Bragg's law. Therefore by

changing the orientation of the crystal, a three dimensional diffraction pattern can be recorded. This pattern is then indexed by software, which also calculates the orientation matrix of the crystal. After the measurement, the lattice parameters and the symmetry of the unit cells can be deduced from the indexed diffraction pattern. The exact positions of the atoms are more difficult to determine. The phase problem prohibits a direct determination of the location of the atoms in the unit cell. Therefore so called direct and indirect methods have to be applied.

The instrument used for single crystal measurements was a Bruker Nonius Kappa CCD FR590 diffractometer with gamma geometry and a liquid nitrogen cooling system.

5.3. X-Ray Powder Diffraction

In X-ray powder diffraction, a powder rather than a single crystal is exposed to X-rays. The powder consists of crystallites which are randomly orientated. During the measurement, the incident light irradiates the sample and a diffraction pattern is obtained. Although the irradiation occurs at a certain angle, all hkl planes fulfill the Bragg condition. This is due to the random orientation of the crystallites. There are always some crystallites, which are orientated in such a way, that a certain hkl plane fulfills the Bragg equation. However the random orientation of the crystallites is also responsible for a major drawback of powder X-ray diffraction. The point signals obtained in single crystal measurements become circles in the powder diffraction pattern, due to the different orientation of the crystallites. This means, that an information loss occurs, as the different point signals overlap in the powder diffraction pattern and can no longer be distinguished anymore. Therefore it is much more difficult to solve an unknown structure on the basis of powder X-

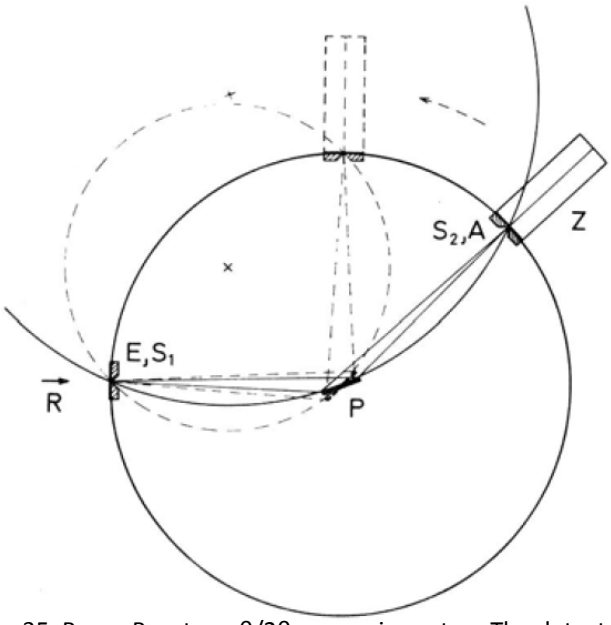

Fig. 35, Bragg-Brentano θ/2θ measuring setup. The detector Z and the x-ray source $\vec{R}$ are moving along the measuring circle. A rotation of the sample P by θ corresponds to a distance of 2θ at the measuring circle. The radiation passes two times a system of slits (S_1, S_2, E, A) [44].

ray measurements, than single crystal measurements. However, if no single crystal is available the crystal structure can be sometimes solved from powder patterns.

All diffraction patterns were recorded with a Bruker D8 Powder-X-ray-Diffractometer with Bragg-Brentano θ/2θ geometry. The detector moves along the measuring circle and the sample holder, located in the center, moves with only half of the angular velocity of the detector. The X-ray radiation passes a system of apertures and the so called soller slits, which reduce the divergence of the ray. Then the X-rays are diffracted at the sample and pass again a system of apertures with Soller slits. Finally the intensity of the diffracted radiation was measured with a Silicon strip detector. It counts along 2θ=3° simultaneously and is much faster compared to a single point detector. The sample is immobilized on the sample holder by using Vaseline as an adhesive. The sample holder itself is a single crystal silicon disc, which is cut along a certain plain to avoid diffraction and is able to rotate around its center.

5.3.1. Rietveld refinement

The Rietveld refinement is a process in which a calculated diffraction pattern, based on a trial structure, is fitted to the observed pattern. In a least squares process, parameters such as atomic coordinates, the model parameters, thermal parameters, etc. are altered in order to obtain the best fit. The formula for the calculated intensities is defined as [44]:

$$y_{ci} = S \sum_K L_K |F_K|^2 \Phi(2\theta_i - 2\theta_K)\, P_K A S_r E + y_{bi} \quad (20)$$

There are several criteria indicating the goodness of the fit. The ones used in this work are the so called R-Bragg (R_B) value for single phases and the weighted profile R-value (R_{wp}) for whole samples. They are defined as follows [45]:

y_{ci}…calculated intensity at point i
S…scaling factor
K…hkl
L_K…Lorentz-polarization factor
F_K…structure factor of a certain hkl plane
Φ…profile function (Gaussian or Lorentzian)
P_K…factor for preferred orientation
A…absorption function
S_r…surface roughness
E…extinction coefficient
y_{bi}…background signal at point i

$$R_B = \frac{\sum_j |I_{obs,j} - I_{calc,j}|}{\sum_j I_{obs,j}} \qquad (21) \qquad R_{wp} = \sqrt{\frac{\sum_j w_j (y_{obs,j} - y_{calc,j})^2}{\sum_j w_j (y_{obs,j})^2}} \qquad (22)$$

Here $I_{obs,j}$ is the integrated intensity of an observed signal j and $I_{calc,j}$ is the calculated integral intensity of this peak. $y_{obs,j}$ are the observed intensities, $y_{calc,j}$ are the calculated intensities and w_j is a weighting factor for a point j in the diffraction pattern.

5.4. Difference Thermal Analysis (DTA)

During a DTA measurement the temperature of a sample and the temperature of a reference substance, which are heated in a furnace at constant rate, are measured against time. The temperature is measured by means of a thermocouple. A thermocouple is composed of two different metals, which are joined together at two points. Due to the Seebeck effect, a temperature difference between the junctions at the two points results in a voltage, which can be measured. This voltage is proportional to the temperature difference. The proportionality constant is called the Seebeck coefficient S.

$$V = S\Delta T \qquad (23)$$

One junction of the thermocouple is placed directly under the sample crucible and the other one under the reference substance.

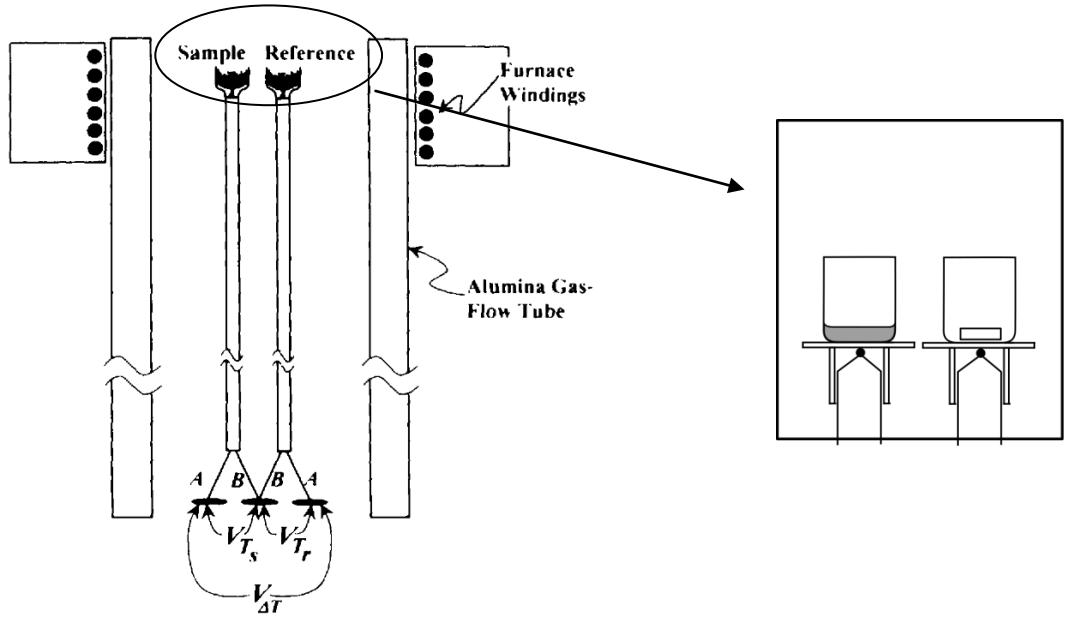

Fig. 36, Measuring setup for a DTA measurement. The junction of the thermocouples (A-B-B-A) is located directly beneath the crucible holder [46].

The reference substance should have a similar thermal mass as the sample and should not undergo a transformation reaction in the temperature range of interest [46]. Both substances are placed in a furnace, which can be heated with a constant heating rate. A typical heating program is shown in the figure below.

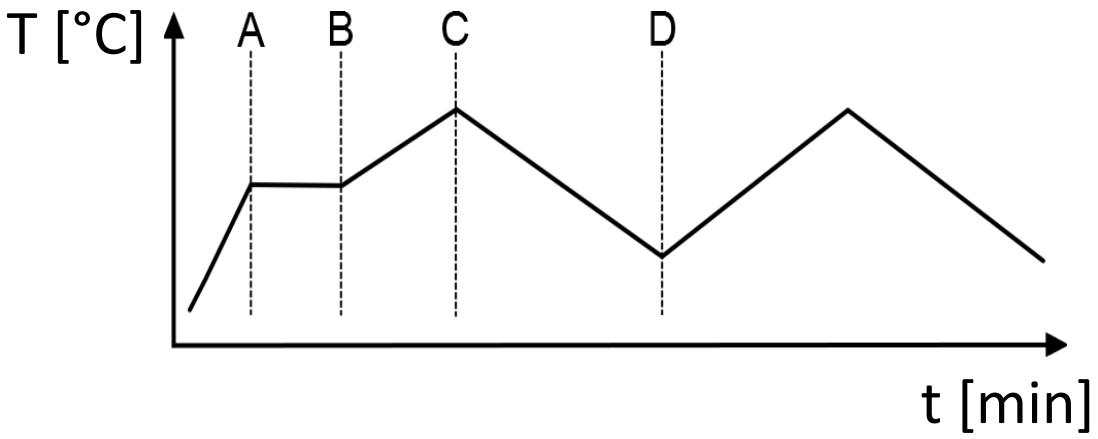

Fig. 37, At first the furnace is heating fast to the annealing temperature of the sample (A). Then the temperature is held for a certain period of time, to equilibrate the sample. After this isothermal section, the actual measurement starts. From point B to C, the temperature is increased beyond the melting point of the sample. Then the first cooling period starts. At point D, the first measurement cycle ends and the second one starts.

During the measurement, the reference substance as well as the sample is heated at a constant rate. The temperature difference between the sample and the reference substance is constant and zero at ideal conditions. In practice it is not zero and changes during heating. The result of both effects gives the baseline. When a reaction occurs in the sample, which consumes (endothermal) or emits (exothermal) energy, the measured temperature difference is increased or decreased, resulting in a peak/signal [47].

There are two different types of reactions occurring in a phase diagram; invariant and non-invariant reactions. Invariant reactions are characterized by zero degrees of freedom according to the Gibbs phase rule. Non invariant reactions have at least one degree of freedom. If an invariant reaction occurs during a DTA measurement, the slope of the corresponding signal is very steep. That's because the temperature of the sample is constant during the course of the reaction (zero degrees of freedom) and therefore the temperature difference between the sample and the reference substance increases rapidly. On the other hand during a non-invariant reaction, the slope of the signal is flatter. Here the sample temperature is still increasing, but with a different slope compared to the reference material.

Therefore the temperature difference between the sample and the reference substance is increasing, but not as steep as during an invariant reaction, in which all of the energy coming from the furnace is used for the phase transformation in the sample.

During the evaluation process, it is important to determine which signals correspond to which type of reaction. For invariant reactions, the transition temperature is determined by taking the onset of the signal. The onset is the point where a significant deviation from the basis line occurs. For non-invariant reactions, like the melting temperature of a higher order sample, the peak maximum is evaluated. However, it is not always possible to distinguish the two types of peaks, especially in ternary systems.

All samples were measured on a DSC 404 F1 Pegasus from NETZSCH, with a type S thermocouple (Pt-Rh/Pt).

5.5. Atomic Absorption Spectroscopy (AAS)

The principle set up of an AAS measurement is shown in Fig. 38.

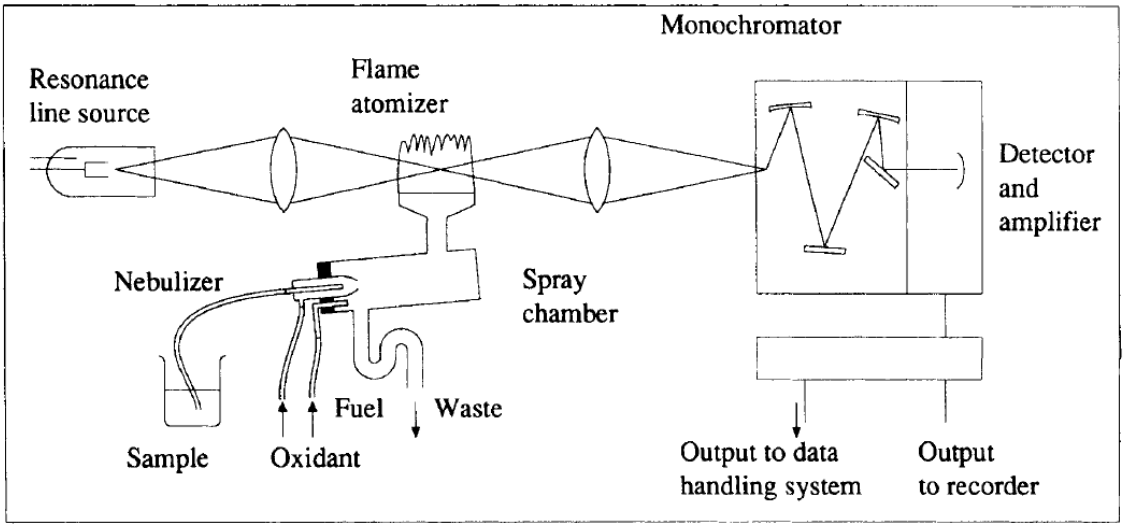

Fig. 38, The instrumental setup of an AAS instrument [48].

The most used radiation sources for AAS are hollow cathode lamps. They consist of a glass tube, in which a cathode and an anode are placed. The cathode is composed of the analyte element and the anode of zirconium, tantalum, nickel or tungsten. The enclosing glass tube is evacuated and filled with a filler gas like Ar or Ne. During operation, a voltage of 100-400V is applied between the electrodes. Electrons with high kinetic energies are emitted from the

cathode and ionize the filler gas. The so produced cations, are accelerated toward the cathode and collide on the surface. The energy of the impact is high enough to sputter atoms from the surface. The vaporized atoms are then excited by collisions with the filler gas or the emitted electrons. During the relaxation process, the characteristic atomic emission spectrum is emitted in parallel with the emission spectrum of the filler gas [48].

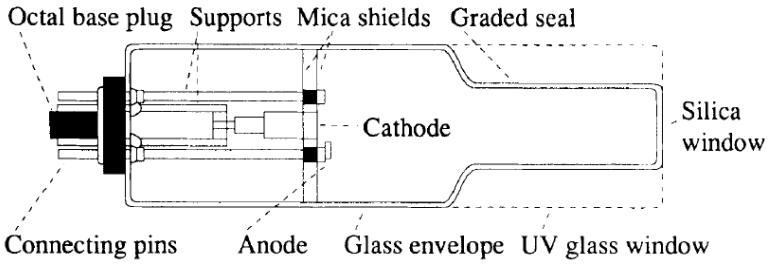

Fig. 39, Vertical cut of an hollow cathode lamp. [48].

The emitted radiation passes the flame atomizer, where the atomized sample absorbs the characteristic atomic radiation. The temperature of flame atomizers lies in the range of 2000-3000K (air-acetylene: 2450K). The sample solution is transported via a nebulizer system into the flame. The nebulizer is a crucial component of the measuring instrument. It does not only transport the analyte to the flame, but also determines the droplet size of the produced aerosol. The droplet size is important in regard of sensitivity and flame noise.

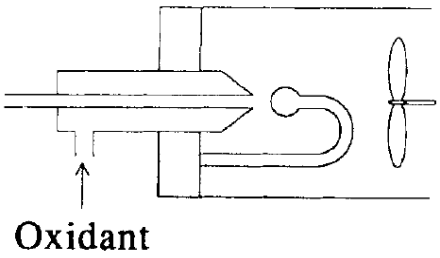

Fig. 40, Impact bead nebulizer: The sample is mixed with the oxidant gas, forming an aerosol. To enhance fragmentation, an impact device is installed [48].

The wavelength for detection is isolated by a monochromator before the radiation reaches the detector system. The monochromator is used to select the wavelength for detection. It consists of two slits (entrance- and exit-slit) and a dispersive element like a prism or a grating. It should be able to resolve two spectral lines which are 0.2nm apart.

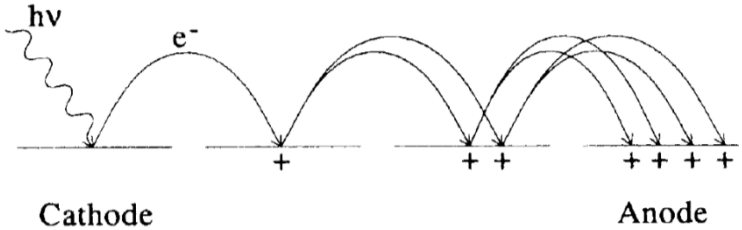

Fig. 41, Working principle of a photo multiplier tube [48].

The detector system is almost always a photo multiplier tube.

These tubes consist of a cathode, able to emit electrons upon irradiation, and several anodes. If the cathode gets irradiated, electrons are emitted, which are accelerated towards the anode material. There the electrons collide and more electrons are emitted. These are accelerated again and collide with another anode, etc. Thereby the initial radiation is transformed into an electrical signal, which can be processed later on. Quantification of the results of an AAS measurement is done by applying the so called Lambert-Beer law.

$$A = abc \qquad (24) \qquad A = -log\frac{I}{I_0} \quad (25)$$

This law states, that the absorbance **A** is equal to the absorptivity **a** multiplied with the path length **b** and multiplied with the concentration **c** of the sample [49]. The absorbance **A** is defined as the negative logarithm of the intensity of the radiation coming from the radiation source, after passing the atomizer (I) over the intensity before passing the atomizer (I_0). Only two variables of the Lambert Beer law are unknown; the sample concentration **c** and the absorptivity **a** of the analyte. The value for the absorbance **A** is the result of the measurement and the path length **b** is a constant, determined by the used instrument. To obtain the concentration of the sample, it is therefore necessary to create a linear calibration curve by measuring solutions with exactly known concentrations. The slope of this curve is equal to the product of the absorptivity **a** and the path length **b**. To include **b** into the calibration gives better results than using the constant instrument parameter:
The instrument used for all conducted measurements was a Perkin Elmer AAnalyst 200 with an air-acetylene flame.

6. Results and Discussion

6.1. The binary Li-Sb system

6.1.1. XRD measurements

To determine the phase equilibria of the binary Li-Sb system, samples of compositional range from 5at.% to 97at.% Li were synthesized. After the annealing process, XRD was used to identify the different phases in the samples. Appendix 9.1. shows all synthesized samples in the binary system. No new binary compounds were found. As mentioned above, antimony reacted with the Ta-crucible. However this was only observed in samples, in which the amount of Sb exceeded 25at%. The reason for this is evident, if one looks at the phase diagram constructed by Sangster and Pelton [19]. In the Li-rich side of the phase diagram (lithium content up to 75%), there is no Sb in equilibrium with another phase. Therefore all the antimony is used up by lithium to form the binary compound Li_3Sb. It seems that Sb reacts preferably with Li rather than with Ta. However if we go beyond the Li_3Sb compound, there is always Sb in equilibrium with another phase. The free Sb is then able to react with the walls of the Ta-crucible. In the solid region between Li_3Sb and Li_2Sb, no free Sb exists. However above the solid region, there is the liquid phase in equilibrium with Li_3Sb. During the cooling process, after melting of the sample, Sb might precipitate out of the liquid phase as shown in Fig. 42. This is why in samples LSB04_500 and Li70Sb30_400 Sb and Sb_2Ta were found in their X-ray diffraction patterns.

If a binary Sb-Ta compound was formed, it was almost always Sb_2Ta. Only once Sb_4Ta_5 has been observed. This was in the sample LSB04_700. It was the only sample, which was annealed at temperatures higher than 500°C. This leads to the assumption, that Sb_4Ta_5 is a phase, which is only stable above 500°C.

A proper indicator for the equilibrium state of a quenched sample is the application of the so called **Gibbs phase rule**. It states, that the number of phases in thermodynamic equilibrium plus the degrees of freedom is equal to the number of components plus two [50]. If the pressure is held constant, the degrees of freedom are reduced by 1. Therefore for a binary system, a maximum of three phases are able to coexist in thermodynamic equilibrium:

$$P + F = C + 2 \qquad (26)$$

Such an invariant equilibrium at a fixed temperature can usually not be quenched. Thus in our quenched samples only two phases can be in equilibrium.

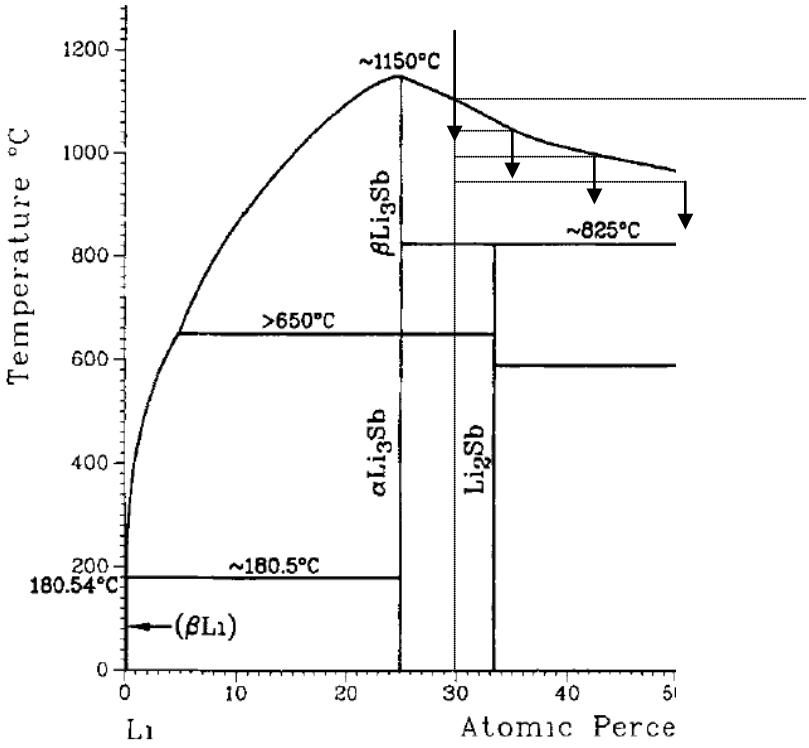

At this point, β-Li_3Sb is formed out of the liquid phase. Beyond this point, the liquid phase becomes more and more Sb rich. Out of this Sb rich liquid, Sb may precipitate if the cooling process is faster than the establishment of thermodynamic equilibrium.

Fig. 42, Precipitation of Sb in the course of cooling a sample in the region between Li_3Sb and Li_2Sb [19].

However in Appendix 9.1., there are samples which show four or even five phases in their X-ray diffraction pattern. One reason for this is the reaction of Sb with Ta, which adds one component and therefore also four phases are allowed to coexist in equilibrium. Another reason is that β-Li_3Sb exhibits a rather strong kinetic stability. β-Li_3Sb is formed at temperatures above 650°C [17]. Such high temperatures are only reached during the melting process of the sample preparation. Here the β-modification of Li_3Sb is formed and it is kinetically stable enough, that at least to a certain extent, it is able to resists the conversion to the alpha modification during the annealing period. Thus it is not possible to synthesize pure α-Li_3Sb from melting and annealing. To investigate the phase transition between α- and β-Li_3Sb a little closer, the sample Li75Sb25, which consisted almost only of the Li_3Sb compound, was divided into three parts. Each part was then annealed at 800°C, 900°C or 1000°C respectively. The parts annealed at 800°C and 1000°C showed a similar X-ray diffraction pattern, which again was similar to the one of the mother-sample Li75Sb25

annealed at 500 °C. The sample, which was annealed at 900°C however showed, apart from α-Li_3Sb and minor amounts of β-Li_3Sb also significant amounts of Sb and Li_2Sb phases in the diffraction pattern. This finding leads to the assumption that the phase transition temperature for the conversion of α-Li_3Sb to β-Li_3Sb might be in the region around 900°C. All Li75Sb25 samples are in a one phase region according to the phase diagram of Sangster and Pelton [19]. However, if the transition temperature for the two modifications of α- and β-Li_3Sb lies at 900°C, then the sample which was annealed at this temperature is may be not in a one phase region (Li_3Sb) anymore, but rather in the three phase region, in which α- and β-Li_3Sb are in thermodynamic equilibrium with a liquid phase. Upon cooling, the Sb-rich liquid formed by a metatectic reaction precipitates Sb as well as Li_2Sb, which is found in the X-ray diffraction pattern. This assumption has to be investigated further. A possible way to determine the phase transition is to prepare the compound Li_3Sb by wet-chemical means in order to obtain only the α-modification. Then parts of this compound have to be annealed at different temperatures, lying in the region between 800°C and 1000°C.

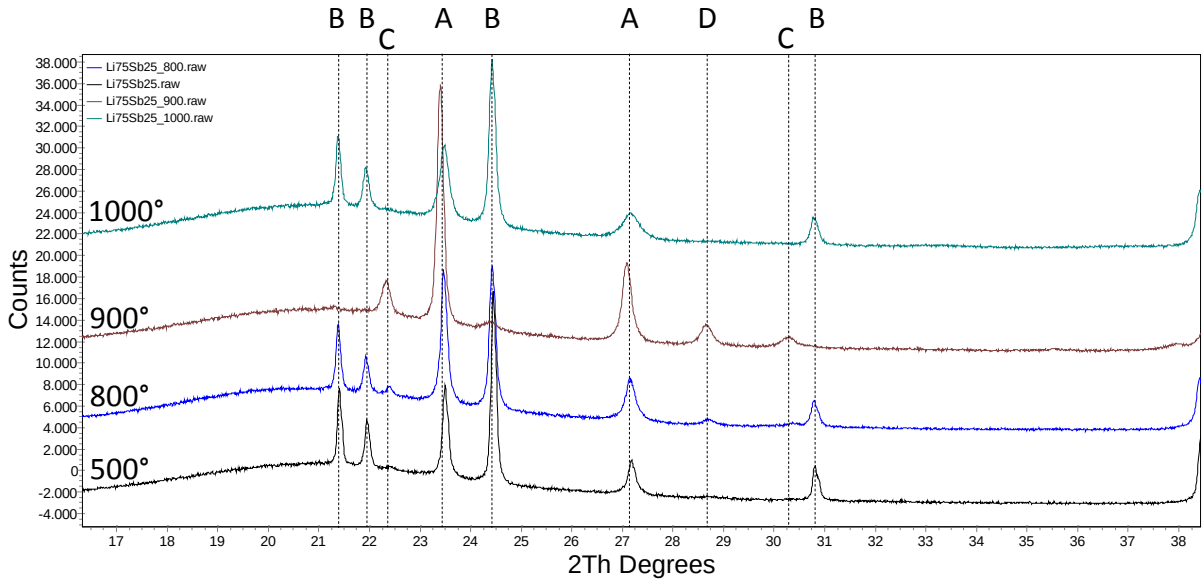

Fig. 43, The XRD patterns of the sample Li75Sb25 annealed at different temperatures (500°C, 800°C, 900°C and 1000°C). The different peaks belong to the following phases α-Li_3Sb (A), β-Li_3Sb (B), Li_2Sb (C), Sb (D).

6.1.2 DTA measurements

To determine the phase transition temperatures in the binary Li-Sb system, Difference Thermal Analysis was used. As lithium and antimony form oxides especially at higher temperatures, they had to be sealed under Ar atmosphere in a tantalum crucible.

Several problems were encountered during the DTA measurements. A major concern was the reaction of solid Ta with Sb in the gas phase. Therefore all pure Sb containing binary samples showed Sb_2Ta phases after the DTA measurements. Because of the contamination of the sample with another component, the phase equilibria and the corresponding phase transition temperatures are influenced making a DTA measurement meaningless. The samples already exhibiting Sb_2Ta after preparation thus were not measured. A significant improvement of the DTA measurements brought a custom made boron nitride inlet for the Ta crucibles. The inlet is supposed to prohibit the formation of Sb_2Ta via the gas phase during DTA measurements.

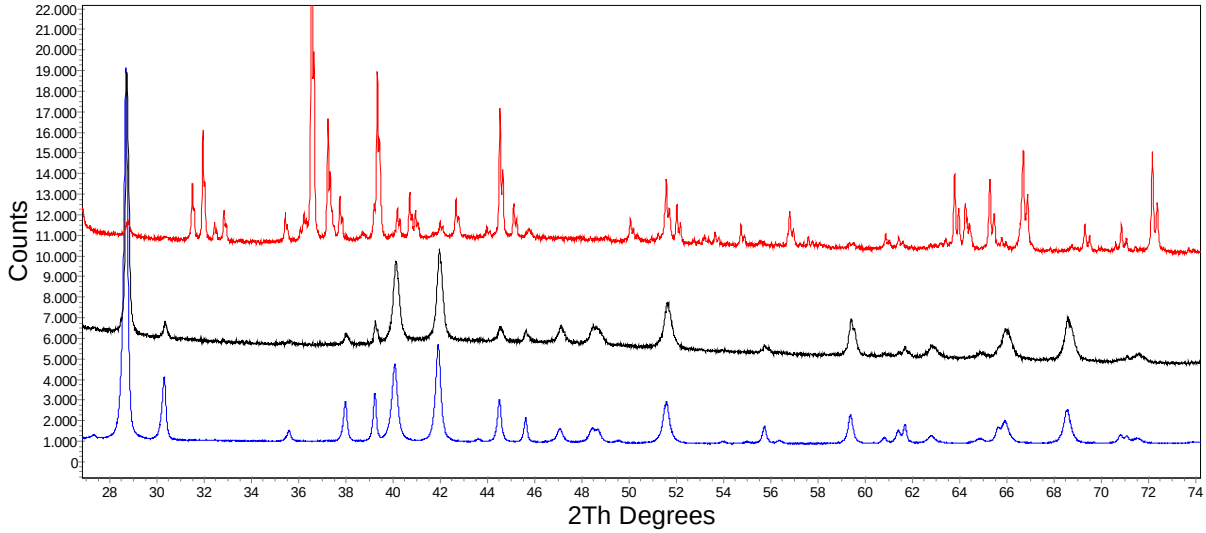

Fig. 44, The XRD patterns of the sample Li25Sb75_BN_500 before (black) and after (red, blue) a DTA measurement is shown. The red pattern shows many additional peaks corresponding to the Sb_2Ta phase, which is formed when no BN inlet is used. The blue pattern is almost identical to the black one and confirms, that a BN inlet for the Ta-crucibles prevents a reaction of Sb with the crucible material.

Initial experiments showed that the reaction between Sb and Ta could successfully be prohibited. As shown in Fig. 44, the sample Li25Sb75_BN_500 was analyzed by X-ray diffraction before and after a DTA measurement. When the Ta-crucible was used without a BN inlet, there are additional peaks in the diffraction pattern, corresponding to the Sb_2Ta compound formed (red pattern in Fig. 44). However, if a BN inlet is used (blue pattern in Fig 41), the diffraction pattern after the DTA measurement is almost identical to the one before the thermal analysis. At first the BN inlets were used without a corresponding BN lid. Therefore a part of the Sb evaporated during the DTA measurements and reacted with the walls of the Ta-crucible. In fact the sample was not contaminated with Sb-Ta phases but Sb was lost during the measurements. Later BN lids were added to the inlets, but as it was not

possible to seal the inlets gas-tight, Sb diffused out of the inlet through the gap between inlet and lid. To determine the influence of the inlet on the measured temperatures, antimony was measured for reference. In Fig. 46 measured DTA signals for the melting point of Sb are shown. The red line represents Sb in a Ta-crucible without BN inlet and the blue one with BN inlet. Fig 46a shows the onsets of the signals and Fig. 46b shows the extrapolated onsets. The phase transition temperature is shifted by a maximum of about 1.6°C towards higher temperatures upon using the inlet. The reason for this shift might lie in the bad thermal conductivity of the BN inlet. Upon melting of Sb – an endothermic process – energy, taken from the surroundings, is consumed. Because of the low thermal conductivity of BN, it takes some time for this effect to be registered by the thermocouple. This time-delay corresponds to a temperature delay, as the reference crucible is heated at a constant rate. That is why the melting temperature is shifted towards higher values.

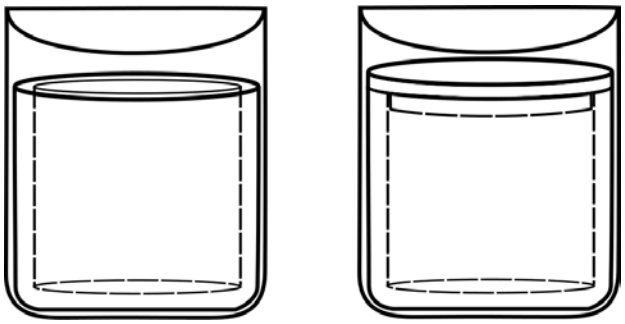

Fig. 45, The BN inlets used for DTA measurements.

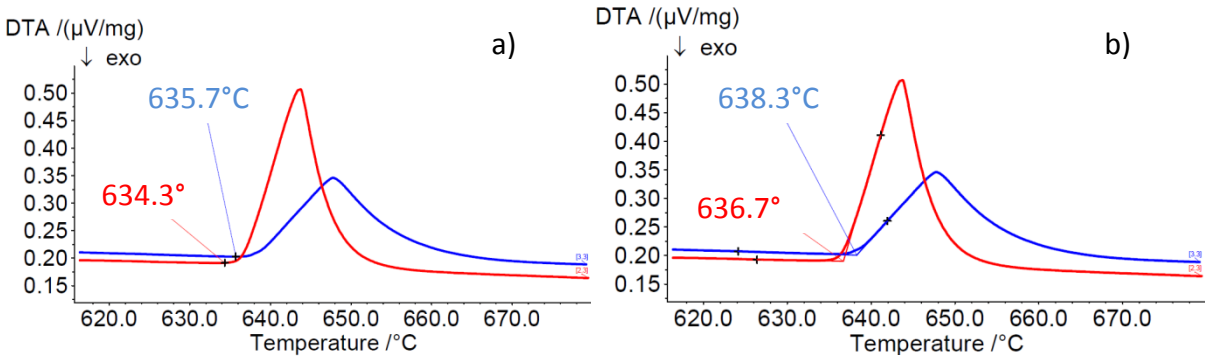

Fig. 46a,b DTA measurements of Sb in Ta-crucible and Sb in Ta-crucible with BN inlet. The red lines represents Sb in a Ta-crucible without BN inlet and the blue ones with BN inlet. The two plots correspond to two different evaluation methods (a: onset, b: extrapolated onset) of the same measurement. As can be seen, the measured temperature of the melting point of Sb is shifted by about 1.6°C to higher temperatures. The broader peak shape of the peak, obtained by measuring with the BN inlet is caused by a higher sample mass and lower thermal conductivity.

The broader peak shape of the blue signal is a result of the higher sample mass used for this measurement. If more mass of a sample is used for DTA measurements, the occurring effects take longer (e.g. melting of the sample) and the corresponding peaks are broader.

To compensate for the higher values of transition temperatures, yielded by measurements with a BN inlet, a new temperature calibration using Ta-crucibles with BN inlets should be done before further measurements are conducted.

Another drawback encountered during DTA measurements was the difficulty to evaluate the signals for the liquidus curve. Especially in the lithium rich side of the phase diagram, where the slope of the liquidus curve is steep no significant corresponding peak could be observed. The degenerated phase transition at about 180°C, which corresponds to the melting of lithium, is well resolved though. But apart from this signal there are only small deviations from the basis line recorded during the cooling periods of the measurements.

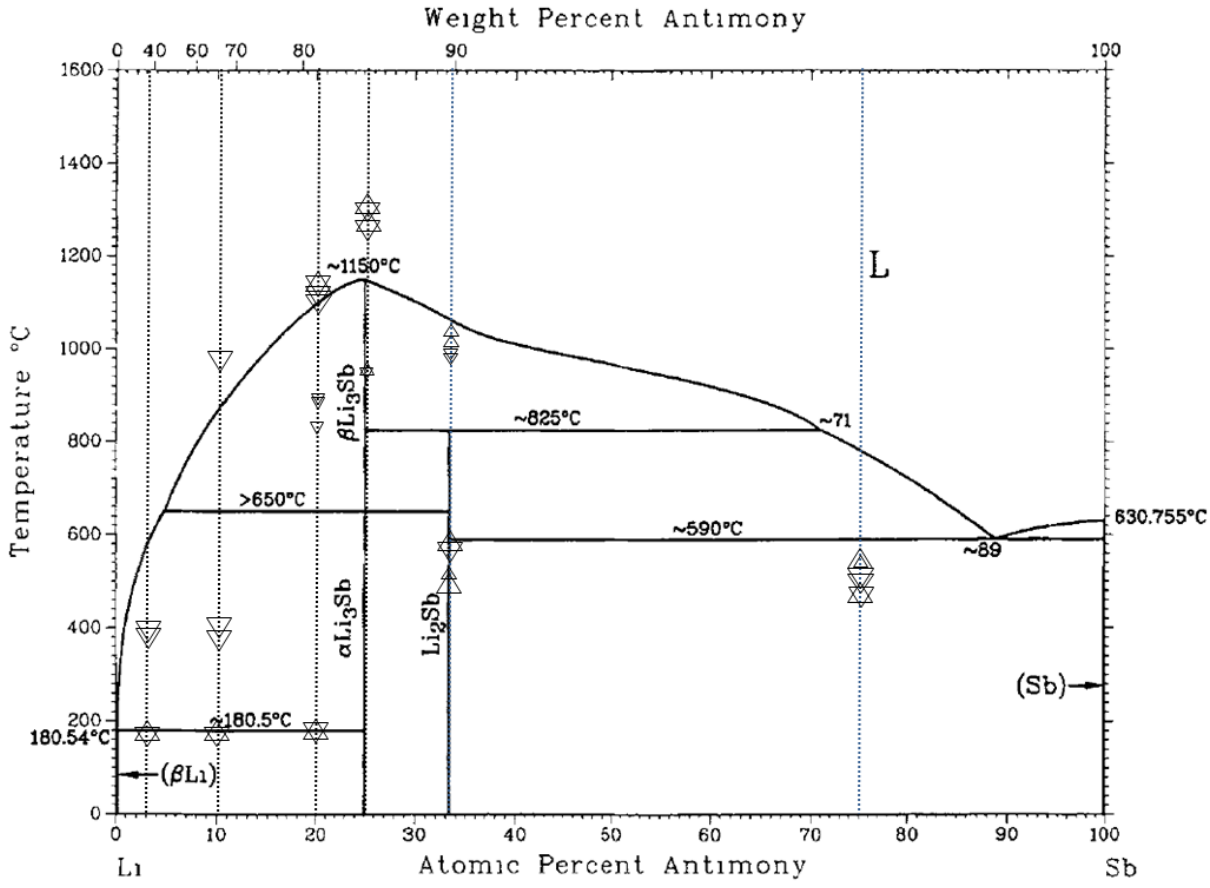

Fig. 47, The DTA data is plotted over the phase diagram calculated by Sangster and Pelton [19]. Triangles facing up reflect signals obtained during heating and triangles facing down are signals obtained during cooling. Small triangles symbolize very weak effects.

In Fig. 47, the signals acquired from the DTA measurements are plotted onto the phase diagram calculated from Sangster et.al. [19] If the DTA data are compared with the phase transitions given below [19], it gets obvious that the phase diagram is not well represented.

Table 7, the reactions observed in the Li-Sb phase diagram, as calculated by Sangster and Pelton [19].

Name	Reaction	Reaction type	Temperature [°C]
c1	L → β-Li_3Sb	Congruent melting	≈1150
p1	L+β-Li_3Sb → Li_2Sb	peritectic	825
d1	β-Li_3Sb → α-Li_3Sb	Degenerate reaction	>650
e1	L → Li_2Sb + Sb	eutectic	590
e2	L → Li + α-Li_3Sb	eutectic	180.5
p2	L + α-Li_3Sb → Li	peritectic	180.5

The lithium rich side of the phase diagram is not resolved clearly. Lithium may either melt in a eutectic reaction (e2), as proposed by Sangster et al [19], or in a peritectic one (p2); see left insert of Fig. 48. However, the reaction temperature is so close to the melting point of Li, that we cannot distinguish the two types of reaction by our DTA measurements.

No signal could be detected corresponding to the transformation of Li_3Sb from the α- into the β-modification. It was allocated at >650 C° by Sangster [19] et al. but the authors did not specify the type of transformation. For the case it is a first order transformation there are two different possibilities as shown in Fig. 48. In any case an α-β metatectic (m1) and a peritectic (p1) reaction occur. In the first case the metatecticum occurs at higher temperatures than the peritecticum and in the second case it is exactly reverse. This is taken into account in the right inserts of Fig. 48.

No DTA signal was obtained for the reaction reported at 825°C (p1). Therefore it is assumed, that the phase transition at 590°C rather is the peritectic decomposition point (p2) of the Li_2Sb phase than the eutectic reaction L → Li_2Sb + Sb. The eutectic temperature was also lowered to 470°C to be in accordance with our experimental data. The liquidus is in general too low and has to be adjusted. To resolve all these issues, the phase diagram was reconstructed and is shown in Fig. 48. The DTA signals are plotted onto the phase diagram. One peak at about 980°C, which was obtained upon cooling of the sample LSb02_DTA was disregarded, because it didn't match any transition reaction at the respective composition (Li at% = 90). The reconstructed phase diagram shows many differences to the one constructed by Sangster et. al. [19]. First of all the liquidus line was adjusted to the experimental data. It was raised, especially in the region of the binary compound Li_3Sb, where it reaches 1307°C (c1 corresponds to the congruent melting of Li_3Sb). The α-β transformation of Li_3Sb was also

raised, due to the experimental results described in the XRD section. The peritectic reaction p1 was lowered to 590°C as no DTA signal could be observed at 825°C.

The reconstructed phase diagram should only be seen as a rough sketch, as only a few data are available because of the experimental difficulties described above. However it supplies a basis for further research. The transition reactions for scheme A of the reconstructed phase diagram are listed in Table 8.

Table 8, The reactions observed in the reconstructed phase diagram (scheme A).

Name	Reaction	Reaction type	Temperature [°C]
c1	L → β-Li_3Sb	Congruent melting	1307
p1	β-Li_3Sb + L → α-Li_3Sb	Peritectic	≈900
m1	β-Li_3Sb → α-Li_3Sb + L	Metatectic	≈900
p2	L+β-Li_3Sb →Li_2Sb	Peritectic	590
e1	L → Li_2Sb + Sb	Eutectic	470
e2	L → (Li) + α-Li_3Sb	Eutectic	180.5

In scheme B, the reaction p1 and m1 have to switch their positions. Additionally, the reaction e2 has to be replaced by p3.

p3	L + α-Li_3Sb → (Li)	Peritectic	180.5

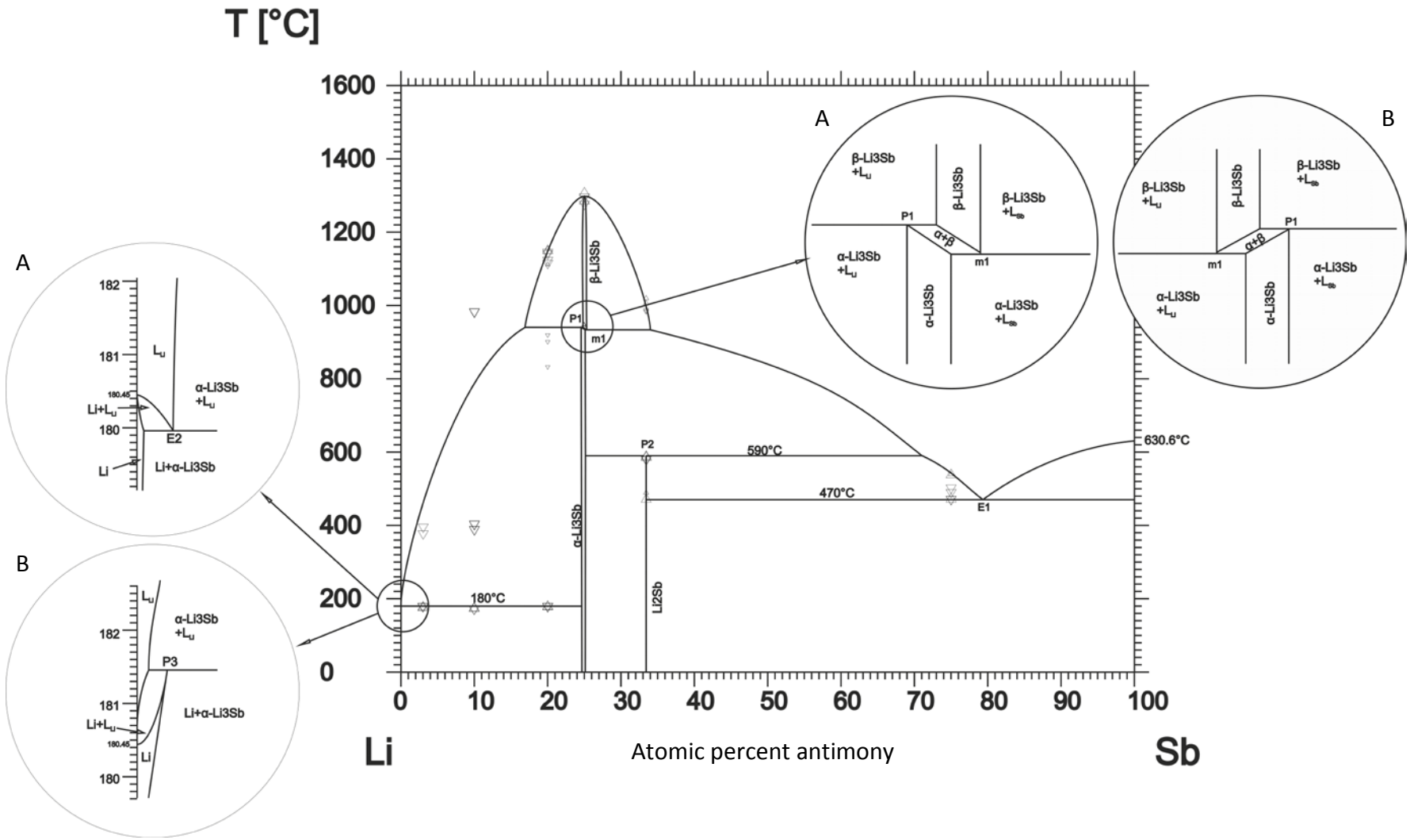

Fig. 48, The reconstructed Li-Sb phase diagram. The DTA data is plotted as triangles. Smaller triangles symbolize very weak observed effects. The Li_3Sb phase is artificially broadened to be able to show the p1 and m1 reactions. The two possible reactions for the degenerate four phase equilibrium as well as the two possibilities of the melting behavior of lithium-rich alloys are shown (scheme A, scheme B).

6.2. The ternary Cu-Li-Sb system

The ternary system Cu-Li-Sb is far from being completely investigated. Especially at higher temperatures, there is no data about the behavior of the different phases. The assumed ternary compounds from Matsuno et. al. [14] and Sharma et. al. [15] also need to be experimentally confirmed in order to ensure their existence. Therefore an investigation of an isothermal section at 400°C was started. Samples were prepared as stated above (see *4. Sample Preparation*) and annealed at 400°C for several weeks. Then they were quenched in water and analyzed by means of XRD and DTA. The respective composition and XRD data of all samples is summarized in Appendix 9.2.

The XRD data of the Li-rich region of the phase diagram was easy to evaluate. There were no unknown phases and no reactions with the crucible material could be observed. However, the samples with less amounts of lithium were more difficult to characterize. On the one hand, antimony reacted, to a little extend, with the tantalum crucibles, yielding an additional phase (Sb_2Ta) in the diffraction patterns. On the other hand, many peaks registered during the XRD measurements could not be assigned to any known structure. Therefore, single crystal measurements had to be conducted.

6.2.1. Newly found structures

Four yet unknown ternary compounds (T2, T3, T4 and T5) could be found at 30–40 at.% Sb of the ternary phase diagram. The respective structures and their relations to the binary β-Li_3Sb compound are listed below. The stoichiometry of all newly found compounds could not yet be determined. For analytical methods like AAS or AES, the mass of the single crystals obtained from the prepared samples is too low. Other techniques like energy dispersive X-ray spectroscopy need polished surfaces, which cannot be provided because of the high reactivity of the samples with oxygen and water. Furthermore, Li is not accessible to this method because of its low amount of electrons. Therefore the only possible way to determine the homogeneity range of the newly found phases is to estimate it from the information obtained by samples containing the respective phases. High quality single crystal refinements are also useful to get information about the composition of the crystal. However, the exact distribution of Li over the atomic sites cannot be determined accurately,

again because of its low amount of electrons. Therefore the reported estimated stoichiometry was deduced from the isothermal section given below and not from the single crystal data.

T2

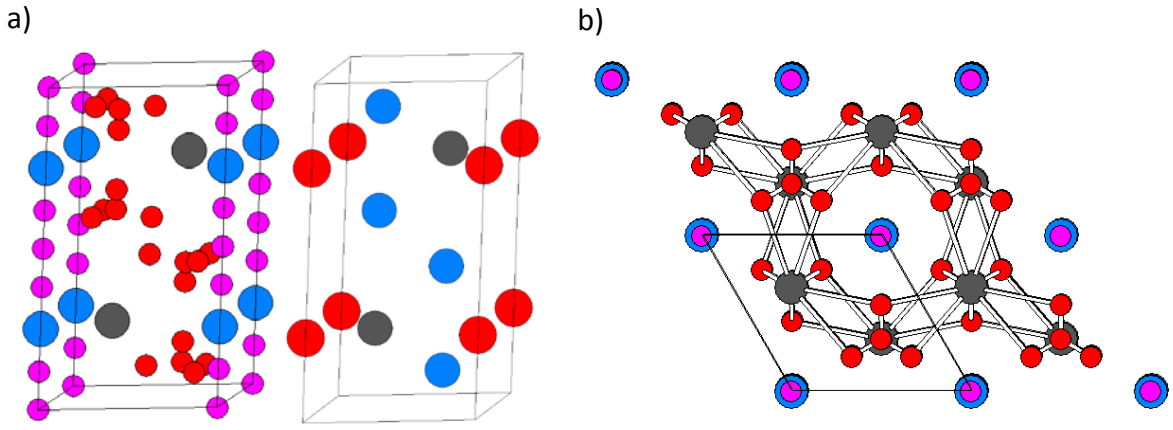

Fig. 49a, The two similar structures T2 (left) and $AsCuLi_2$ (right) are shown. The color code for the T2 structure is: Sb (grey), Cu (red), Li (blue) and the two mixed positions M1 and M2 (purple). The color code for the structure of $AsCuLi_2$ As(grey), Cu (red), Li (blue). b, the structure of T2 is shown parallel to the [001] plane. The Li-tunnel build up by Sb and Cu is clearly visible.

The T2 phase was found in the sample Li25Cu50Sb25. It exhibits a hexagonal structure, which belongs to the space group P*63/mmc*. This is the same as for β-Li_3Sb. A real isotypic structure could not be found but the structure of the compound $AsCuLi_2$ is very similar to the one of the T2 phase. The difference between the two is evident in Fig. 49a; the T2 structure has much more atomic sites than the $AsCuLi_2$ structure. The positions Cu2, Cu3, M1 and M2 are missing in the $AsCuLi_2$ phase. It is assumed, that the Cu2 and Cu3 positions indicate the thermal oscillation of the copper atoms. The majority of the copper atoms are located at Cu1, although it is also possible for them to occupy position Cu2 and Cu3. However due to steric reasons, there is the restriction, that only one of the positions assigned to copper can be occupied at the same time. They are so called split positions. In Fig. 49b, the structure of the T2 phase is shown parallel to the crystallographic plane [001]. Along the c-axis the positions Li1, M1 and M2 are aligned. It was difficult to confine these positions to a certain z-coordinate, as they are not clearly separated from each other in terms of the electron density distribution functions obtained from the single crystal diffraction experiment. As can be seen in Fig. 49b, the Sb and Cu atoms confine the location of the Li atoms by creating a

kind of tunnel along the c-axis. The electron density function within this tunnel is blurred, however there is a maximum at the Li1 position. To account for the spare part of the electron density function between the Li1 positions, the positions M1 and M2 were set up. It is not possible to assign a distinct element—Li or Cu—to these positions, as both of them are able to occupy M1 as well as M2. They are so called mixed positions. However, it is not possible, again due to steric reasons, that all positions, Li1, M1 and M2 are occupied at the same time. The ionic radius of lithium is estimated to be around 0.86Å [50]. Therefore it takes at least 1.72 Å to put two lithium ions next to each other. The positions Li1-M2 and M1-M2 however exhibit inter-atomic distances below this value. This is in contrast to the single crystal data refinement, which yielded an occupation of the Li1 position of 100%. However due to the blurred electron density in this region, the occupancy of the three split positions cannot be determined more precisely.

In table 9, the crystallographic data obtained from the single crystal measurement of the T2 phase is shown. The remark "(Cu)" for the M1 and M2 positions means that the scattering curve of copper was used to refine these positions and their occupancy.

The estimated stoichiometry of this phase is $Cu_{50}Li_{20}Sb_{30}$.

Table 9, The crystallographic data obtained from the single crystal measurement of the T2 phase are listed.

space group: P*63/mmc*

structure type: $Cu_5Li_2Sb_3$

a=4.32Å

c=7.45Å

Designation	Atom positions			Wyckoff	Occupancy
	x	y	z	symbol	[%]
Li1	0	0	¼	2b	100
Cu1	1/3	2/3	0.59492(z)	4f	61
Cu2	1/3	2/3	0.65668(z)	4f	10
Cu3	0.22269(x)	0.44539(y)	0.57800(z)	12k	7
Sb1	1/3	2/3	¼	2c	100
M1 (Cu)	0	0	0	2a	7
M2 (Cu)	0	0	0.11945(z)	4e	3

T3

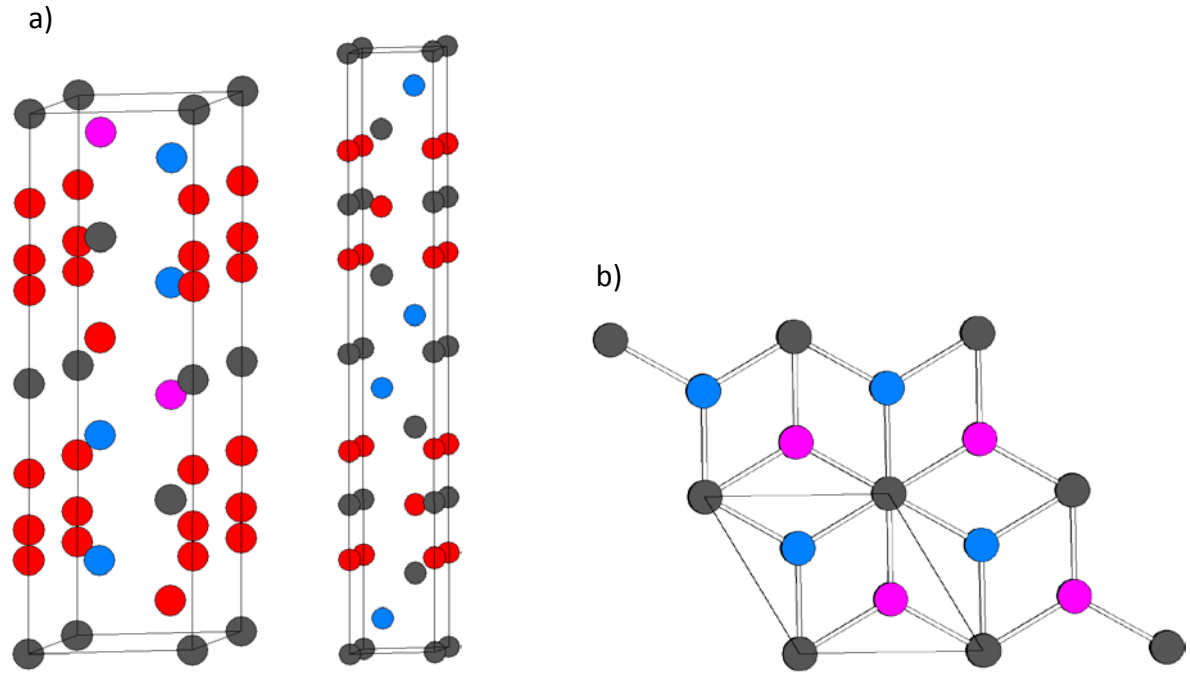

Fig. 50a, The two similar structures of the phase T3 (left) and $Al_3C_4Zr_2$ (right) are shown. The color code for the T3 structure is: Sb (grey), Cu (red), mixed Li/Cu position (violet), Li (blue). The color code for the structure of $Al_3C_4Zr_2$ was adapted to the one of T3 to emphasize their similarities: C (grey), Al (red), Zr (blue). b, the structure of T3 is shown parallel to the [001] plane.

The ternary compound T3 was also found in the sample Li25Cu50Sb25. It exhibits a hexagonal structure too, belonging to the space group P*63mc*. Again there is no isotypical structure for the T3 phase, however, as can be seen in Fig. 50a, it is similar to the $Al_3C_4Zr_2$ structure. The most obvious difference between the two structures is the length of the unit cell along the c-axis. The T3 structure has a lattice parameter c of 14.44 Å, whereas the $Al_3C_4Zr_2$ structure has one of 22.24 Å. However the same amounts of atoms are placed in both unit cells. Therefore due to steric reasons, some of the positions in the T3 structure are split positions. These are Cu2, Cu3 and Cu4, which are all placed along the c-axis. Although it might be possible that the positions Cu2 and Cu4 are occupied at the same time (interatomic distance = 2.32 Å), this is not possible for the Cu2-Cu3 and Cu3-Cu4 positions. The mixed position Cu1/Li1 is occupied by copper and lithium. Compared to T2 the mirror plane perpendicular to the six-fold axis is lost in this structure. This loss in symmetry is also reflected by the less symmetric space group and the lattice parameter c, which is twice as large as in T2.

The estimated stoichiometry of the T3 phase is $Cu_{45}Li_{30}Sb_{25}$.

Table 10, The crystallographic data obtained from the single crystal measurement of the T3 phase are listed.

space group: P*63mc*

structure type: $Cu_{45}Li_{30}Sb_{25}$

a=4.34Å

c=14.44Å

Designation	Atom positions			Wyckoff symbol	Occupancy [%]
	x	y	z		
Cu1/Li1	1/3	2/3	0.54802(z)	2b	66/34
Li2	1/3	2/3	0.10913(z)	2b	100
Li3	1/3	2/3	0.34003(z)	2b	100
Cu2	0	0	0.66593(z)	2a	81
Cu3	0	0	0.77037(z)	2a	37
Cu4	0	0	0.82686(z)	2a	45
Cu5	1/3	2/3	0.92843(z)	2b	100
Sb1	0	0	0.5	2a	100
Sb2	1/3	2/3	0.74239(z)	2b	100

T4

space group: P6??

structure type: ???

a=4.21Å

c=22.13Å

T4 also exhibits a hexagonal structure with a lattice parameter a=4.2 Å and a lattice parameter c=22.13 Å. It is assumed, that the symmetry of this structure is even lower than the one of T3, as the lattice parameter c is now thrice as large as in T2. The exact space

group is not known, although two single crystals were measured. However due to technical difficulties with the X-ray detector, the data were lost.

The estimated stoichiometry of T4 is $Cu_{71}Li_{07}Sb_{22}$

T5

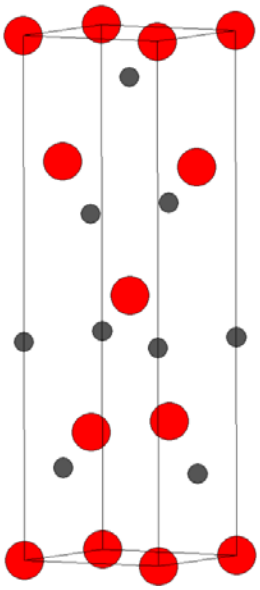

Table 11, The crystallographic data of the NbAs structure [52].

space group:I*41*

structure type: NbAs

a=4.38Å

c=6.05Å

Position	coordinates			Wyckoff symbol	Occupancy [%]
	x	y	z		
Sb1	0	0	0.41600(z)	4a	-
Cu1	0	0	0	4a	-

Fig. 51, The NbAs structure, on which the estimated structure for the T5 phase was based on.

The T5 phase is the only one, which is not yet experimentally confirmed. During the evaluation of the XRD patterns of the samples Li25Cu25Sb50, Li30Cu42Sb28 and Li33Cu33Sb33, some peaks could not be assigned to a known structure. On the basis of these peaks, a new phase was defined and the peaks were indexed with the TOPAS software. The most probable solution for this phase was a crystal structure with space group I41 and the lattice parameters given above. These parameters were used as input for a search in the ICSD database. The AsNb-phase, as described by [52], has the same space group and similar lattice parameters (a = 3.45Å; c = 6.33Å) as the newly defined one. Using the software ATOMS, a structure file was created, which defines the structure of the phase AsNb, but substitutes the As atoms with Sb and the Nb atoms with Cu. This structure file was then used to refine the XRD patterns of the three samples mentioned above. This enhanced the quality of the refinements by a value of 2 (R_{wp}-value). In the structure-file for the phase T5, no lithium atoms were defined. However, as lithium has only three electrons it hardly

influences the XRD pattern. The lithium atoms in the real structure might influence the positions of the Cu and Sb atoms, but they themselves hardly contribute to the XRD signals. The techinque used to describe the structure of the T5 phase is of course just a rough assumption, the accurate structure has to be determined by single crystal XRD. Unfortunately we did not yet succed to depict proper single crystals from the respective samples. The estimated stoichiometry of T5 is $Cu_{30}Li_{30}Sb_{40}$.

6.2.2. Isothermal section at 400°C

With the aid of the newly found compounds, the following isothermal section was obtained.

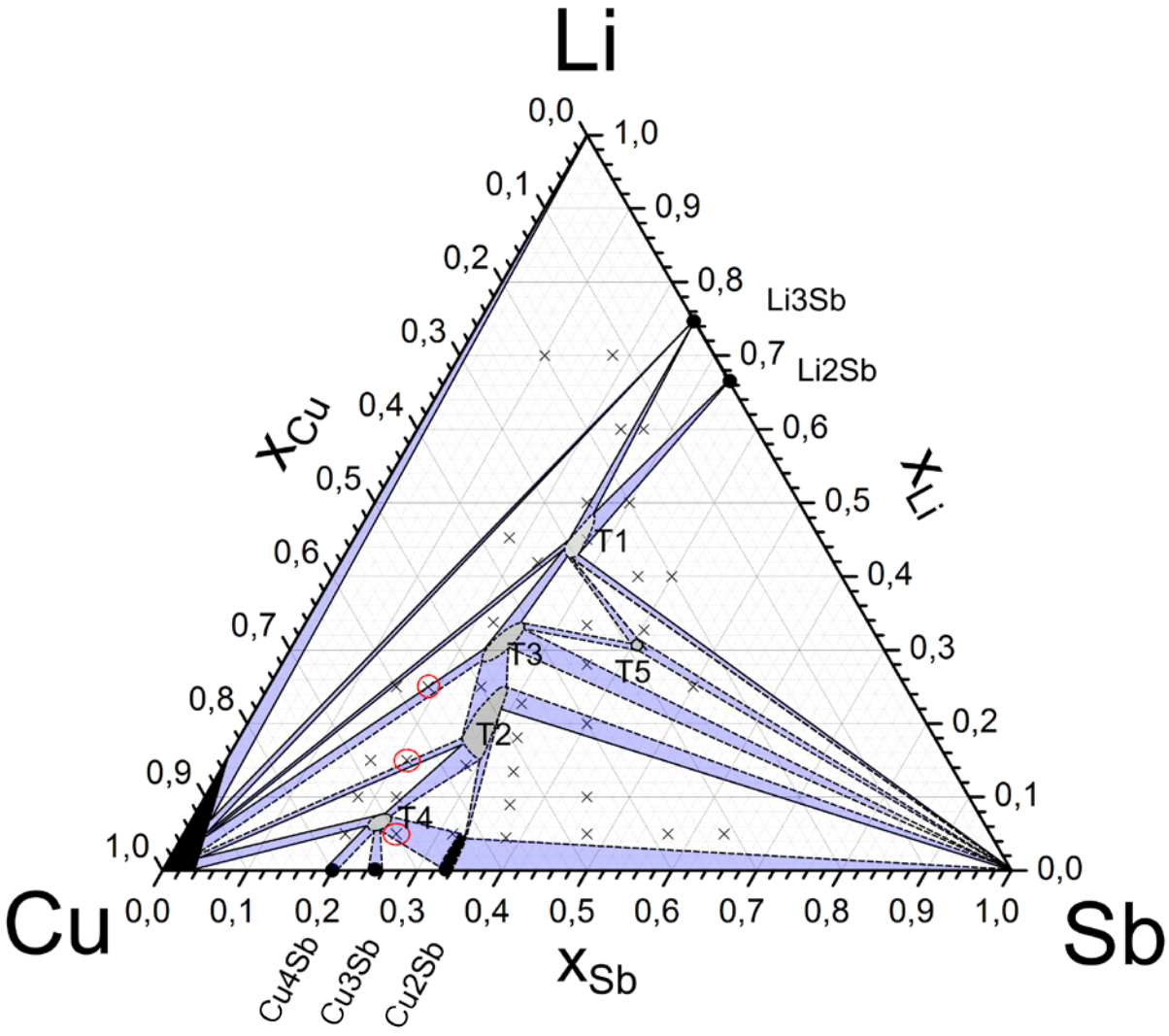

Fig. 52, Isothermal section at 400°C. Solid lines are drawn when the corresponding phase equilibria are confirmed with at least one sample. Dashed lines are drawn, when the phase equilibria are not yet confirmed, or when inconsistencies occurred between different samples. Also the ternary phases are dashed, because their homogeneity region is still not clarified. Black regions indicate solubility in the respective phase, blue regions indicate two phase equilibria and white regions indicate ternary equilibria.

On the basis of the XRD data obtained from the prepared samples, the different phases in equilibrium were determined. In the upper part of the isothermal section, the phase triangles are quite straightforward. The binary phases stable at 400°C were joined with the already known ternary compound $CuLi_2Sb$ (=T1). The shape of the T1 structure looks odd and is shifted from the ideal stoichiometry. This was done in order to ensure, that the sample LiCuSb03 is situated in the phase triangle Cu-Li_3Sb-T1.

In the antimony rich region of the phase diagram only few samples were prepared. The reason for this lies in the formation of Sb_2Ta, which contaminated the samples (see chapter 4.2.1. *Tantalum crucibles*). In order to prevent this side reaction, ceramic crucibles will be used for the study of the Sb rich side in the near future.

In the center of the phase diagram it was difficult to assign a structure to some of the peaks found in the diffraction patterns of the samples L33Cu33Sb33, Li30Cu42Sb28 and Li25Cu25Sb50. As already described above (see *6.2.1. newly found structures*), a yet unknown ternary phase T5 is assumed in this region.

The copper rich side of the phase diagram is the quite complex. In this region the other three newly found ternary compounds, were discovered. In the sample Li25Cu50Sb25, single crystals of the new phases T2 and T3 were found and analyzed. Thereby the structures of the two ternary compounds were characterized. In the sample Li05Cu76Sb19, a single crystal with a hexagonal structure was found. After a short single crystal XRD scan, the symmetry of the unit cell and the lattice parameter could be determined. The lattice parameter are a=4.21 Å and c=22.13 Å. Unfortunately, during the measurement, the controlling computer encountered a fatal error and the data were lost. Therefore this measurement has to be repeated, once the measuring system works again.

Surprisingly the ternary compounds (except T5 which was not yet confirmed) all align at about 26at% Sb and 74at%Cu and ends at Li3Sb. This shows that the relative amount of antimony of these compounds is quite constant and only the copper and lithium concentration changes. One could explain this behavior with an ionic interaction of Sb (five outer electrons) and mainly Li but also Cu which both contribute one electron. Finally, Li_3Sb perfectly follows this assumption. This also strengthens the consideration of [13], that during the lithiation of Cu_2Sb, the antimony atoms stay at their positions and only the copper and the lithium atoms rearrange.

The proposed phases CuLiSb, $CuLi_{1.5}Sb$ [14], $Cu_2Li_{0.5}Sb$ and $Cu_{1.5}LiSb$ [15] could not be confirmed. However, some of the newly found phases lie in the range of some of the proposed compositions. The T5 phase is situated near the calculated CuLiSb phase, but deviates from the calculated composition. Also the T3 phase lies near the postulated $Cu_{1.5}LiSb$ phase. However this might just be a random coincidence and the proposed phases might not be stable at 400°C.

The analysis of the isothermal section at 400°C of the ternary system Cu-Li-Sb is of course not yet finished. Some phase equilibria still need to be confirmed experimentally.

7. Summary

7.1. Summary (English)

For a systematic design of intermetallic anodes for Li-ion batteries detailed knowledge of phase equilibria of the related material systems is indispensable. The binary system Li-Sb as well as the ternary system Cu-Li-Sb were investigated by means of XRD, single crystal XRD and DTA measurements. Also AAS measurements were conducted to determine the final sample composition of samples prepared in alumina crucibles. Also the literature on these two systems was reviewed. Additionally the binary systems Cu-Li and Cu-Sb were discussed, as they are part of the ternary Cu-Li-Sb system. There is only very scarce literature information on Cu-Li-Sb.

The first step of the investigations in the binary system was the search for a proper crucible material for sample preparation. As both lithium and antimony are highly reactive materials, side reactions with different crucible materials were encountered. Crucibles made out of tantalum, alumina, magnesia and boron nitride were tested. Also two hybrid approaches were tested, especially in regard of their applicability for DTA measurements. The most promising solutions found are BN crucibles with lids for the sample preparation and a hybrid approach, which contains a BN inlet put upside down into a Ta-crucible for DTA measurements.

On the basis of the obtained DTA data, the Li-Sb phase diagram calculated by Sangster and Pelton [19] was reconstructed. The degenerated four phase equilibrium occurring at >650°C was resolved using two possible reaction schemes. The transition temperature of the α- and β-modification of Li_3Sb, which was roughly determined by Brauer and Zintl [17] (>650°C), was elevated to 900°C and the corresponding melting temperature to 1307°C. The peritectic melting point of Li_2Sb was set to 590°C and the eutectic temperature to 470°C.

In the ternary system, an isothermal section at 400°C was investigated. Cu-Sb alloys of different composition were prepared. Then lithium was added to prepare samples of different composition. Sb rich samples reacted with the Ta-crucibles used and formed Sb_2Ta. Therefore BN crucible will be used for future sample preparations. Four yet unknown

compounds could be identified in the lower half of the isothermal section. Two of them (T2 and T3) could be fully characterized using single crystal XRD. The other two will be analyzed in the near future. Using the newly found phases, phase triangles were established in the isothermal section. There are still some inconsistencies regarding the phase equilibria in the copper rich region. These have to be clarified by preparing more samples.

7.2. Zusammenfassung (Deutsch)

Für eine systematische Entwicklung intermetallischer Anodenmaterialien für Li-Ionenbatterien ist eine fundierte Kenntnis über die Phasengleichgewichte in den entsprechenden Systemen unabdinglich. Das binäre System Li-Sb als auch das ternäre System Cu-Li-Sb wurden mittels XRD, Einkristall XRD und DTA untersucht. Außerdem wurden AAS Messungen vorgenommen um die endgültige Zusammensetzung bestimmter Proben zu untersuchen, die in Aluminiumoxid-Tiegeln hergestellt wurden. Bereits publizierte Informationen über die beiden Systeme wurden zusammengefasst und diskutiert. Zusätzlich wurden auch die Systeme Cu-Li und Cu-Sb besprochen, da sie Teil des ternären Systems Cu-Li-Sb sind. Es gibt nur wenig Literatur über das System Cu-Li-Sb.

Der erste Schritt der Untersuchung des binären Systems war es, ein geeignetes Tiegelmaterial für die Probenherstellung zu finden. Da sowohl Lithium als auch Antimon sehr reaktive Materialien sind, wurde Nebenreaktionen mit verschiedenen Tiegeln beobachtet. Die folgenden Tiegelmaterialien wurde getestet: Tantal, Aluminiumoxid, Magnesiumoxid und Bornitrid. Außerdem wurde auch zwei Hybridansätze ausprobiert, vor allem in Hinblick auf ihre Anwendung für DTA Messungen. Die erfolgversprechendsten Lösungen waren BN Tiegel mit Deckel für die Probenherstellung und ein Hybridansatz, bei dem ein BN Inlet mit der Öffnung nach unten zeigend in einen Tantal-Tiegel gestellt wird, für DTA Messungen.

Basierend auf die durchgeführten DTA Messungen, wurde das Phasendiagramm, welches von Sangster und Pelton [19] berechnet wurde, neu konstruiert. Das degenerierte Vierphasengleichgewicht bei ca. 650°C wurde mithilfe zweier möglicher Reaktionsschemata aufgelöst. Die Übergangstemperatur der α- und β-Modifikation des Li_3Sb Verbindung, die grob von Brauer und Zintl [17] bestimmt wurde (>650°C), wurde auf 900°C angehoben und der entsprechende Schmelzpunkt auf 1307°C gesetzt. Die peritektische Schmelztemperatur der Li_2Sb Phase wurde auf 590°C gesetzt und die eutektische Temperatur auf 470°C.

Im ternären System wurde ein isothermer Schnitt bei 400°C untersucht. Cu-Sb Legierungen unterschiedlicher Konzentration wurden hergestellt. Dann wurde Lithium zugegeben um Proben verschiedener Zusammensetzung zu erhalten. Sb reiche Proben reagierten mit dem Ta-Tiegel, in dem sie wärmebehandelt wurden, und es bildete sich Sb_2Ta. In Zukunft werden

hier BN Tiegel Anwendung finden. In der unteren Hälfte der Isotherme konnten vier, bisher unbekannte, ternäre Phasen identifiziert werden. Zwei von ihnen (T2 und T3) wurden auch schon mittels Einkristall XRD vollständig charakterisiert. Die anderen beiden werden in naher Zukunft analysiert werden. Mithilfe der neu gefundenen Phasen konnten Konnodendreiecke im isothermen Schnitt aufgestellt werden. Es gibt jedoch noch Unstimmigkeiten bezüglich der Phasengleichgewichte im kupferreichen Gebiet. Diese können durch die Präparation von mehr Proben geklärt werden.

8. References:

[1] Kotobuki, M., *The Current Situation and Problems of Rechargeable Lithium Ion Batteries*. The Open Electrochemistry Journal,2012. 4: p.28-35.

[2] Nishi, Y., *Lithium ion secondary batteries; past 10 years and the future*. Journal of Power Sources, 2001. 100: p.101–106.

[3] Kanamura, K., eds. *PROBLEMS AND EXPECTANCY IN LITHIUM BATTERY TECHNOLOGIES*. Lithium Batteries, Advanced Technologies and Applications, ed. Scrosati, B., Abraham, K.M., van Shalkwijk, W., Hassoun, J., 2013, Hoboken, New Jersey: John Wiley & Sons, Inc.

[4] Ehrlich, G.M., eds. *LITHIUM-ION BATTERIES*. Handbook of Batteries, ed. Linden, D., Reddy, T.B., 2002, New York: The McGraw-Hill Companies, Inc.

[5] Goodenough, J.B., Park, K-S., *The Li-Ion Rechargeable Battery: A Perspective*. Journal of the American Chemical Society, 2013. 135: p.1167-1176.

[6] Zhang, W-J., *A review of the electrochemical performance of alloy anodes for lithium-ion batteries*. Journal of Power Sources, 2011. 196: p. 13-24.

[7] Larcher, D., Beattie, S., Morcrette, M.,Edström, K., Jumasc, J-C. Tarascona, J-M., *Recent findings and prospects in the field of pure metals as negative electrodes for Li-ion batteries*. J. Mater. Chem., 2007. 17: p.3759–3772.

[8] Agubra, V., Fergus, J., *Lithium Ion Battery Anode Aging Mechanisms*. Materials, 2013. 6: 1310-1325.

[9] Benedek, R., Thackeray, M.M., *Lithium reactions with intermetallic-compound electrodes*. Journal of Power Sources, 2002. 110: p.406-411.

[10] Lukas, H.L., Fries, S.G., Sundman, B., Computational Thermodynamics, The Calphad Method. 2007, Cambridge: Cambrdige University Press.

[11] Wang, J., Raistrick, I.D., Huggins, R.A., *Behavior of Some Binary Lithium Alloys as Negative Electrodes in Organic Solvent-Based Electrolytes*. J. Electrochem. Soc.: ELECTROCHEMICAL SCIENCE AND TECHNOLOGY, 1986. 133(3): p.457-460.

[12] Besenhard, J.O., Fritz, H.P., *REVERSIBLES ELEKTROCHEMISCHES LEGIEREN VON METALLEN DER V. HAUPTGRUPPE IN ORGANISCHEN LI^+-LÖSUNGEN*. Electrochimica Acta, 1975. 20: p.513-517.

[13] Fransson, L.M.L., Vaughey, J.T., Benedek, R., Edström, K., Thomas, J.O., Thackeray, M.M., *Phase transitions in lithiated Cu_2Sb anodes for lithium batteries: an in situ X-ray diffraction study*. Electrochemistry Communications, 2001. 3: p.317-323.

[14] Matsuno, S., Noji, M., Kashiwagi, T., Nakayama, M., Wakihara, M., *Construction of the Ternary Phase Diagram for the Li-Cu-Sb System as the Anode Material for a Lithium Ion Battery*. J. Phys. Chem. C, 2007. 111: p.7548-7553

[15] Sharma, S., Dewhurst, J. K., Ambrosch-Draxl, C., *Lithiation of InSb and Cu2Sb: A theoretical investigation*. PHYSICAL REVIEW B, 2004. 70: p. 104110.1-104110.5.

[16] Lebeau, M.P., *Sur l'antimonuire de lithium et sur la preparation de quelques alliages de ce metal*. Comptes rendus hebdomadaires des séances de l'Académie des sciences, 1902. Séance du 27 Janvier: p.231-233.

[17] Brauer, G., Zintl, E., *Konstitution von Phosphiden, Arseniden, Antimoniden und Wismutiden des Lithiums, Natriums und Kaliums*. 23. Mitteilung über Metalle und Legierungen, 1937. p.323-352.

[18] Gérardin, R., Aubry, J., *Préparation et identification d'un nouveau compose binaire Li_2Sb*. C.R. Acad. Sc. Paris Série C, 1974. 278: p.1097-1098.

[19] Sangster, J., Pelton, A.D., *The Li-Sb (Lithum-Antimony) System*. Journal of Phase Equilibria, 1993. 14(4): p.514-517

[20] Massalski, T. B.; Okamoto, H.; ASM International. *Binary alloy phase diagrams*; 2nd ed.; 1990, Materials Park, Ohio: ASM International.

[21] Pelton, A.D., *The Cu-Li (Copper-Lithium) System*. Bulletin of Alloy Phase Diagrams, 1986. 7(2): p.142-144.

[22] Klemm, W., Volavšek, B., *Zur Kenntnis des Systems Lithium-Kupfer*. Zeitschrift für anorganische und allgemeine Chemie, 1958. 296: p.1958 1934

[23] Pastorello, S., *Thermal analysis of the system: lithium-copper*. Gazzetta chimica italiana, 1930. 60: p.988-

[24] Dudel, F.P., Gole, J.L., Sanders, T.H., King, J., Browner, R., *Kinetically controlled lithiation: a variant of physical vapour deposition with application to lightweight alloys and lithium batteries*. PHILOSOPHICAL MAGAZINE B, 1997. 75(5): p.733-755

[25] Van de Walle, A., Moser, Z., Gasior, W., *First-principles calculation of the Cu-Li phase diagram*. Archives of Metallurgy and Materials, 2004. 49(3): p.535-544.

[26] Gasior, W., Onderka, B., Moser, Z., Dębski, A., Gancarz, T., *Thermodynamic evaluation of Cu_Li phase diagram from EMF measurements and DTA study*. CALPHAD: Computer Coupling of Phase Diagrams and Thermochemistry, 2009. 33: p.215-220.

[27] Fürtauer, S., Flandorfer, H., *A new experimental phase diagram investigation of Cu–Sb*. Monatsh Chem, 2012. 143: p.1275–1287

[28] Pauly, H., Weiss, A., Witte, H., *The Crystal Structure of the Ternary Intermetallic Phases Li_2EX (E=Cu, Ag, Au; X=Al, Ga, In, Tl, Si, Ge, Sn, Pb, Sb, Bi)*. Z. Metallkde., 1968. 59: 47-58.

[29] Reshak, A.H., Kamarudin, H., *Theoretical investigation for Li2CuSb as multifunctional materials: Electrode for high capacity rechargeable batteries and novel materials for second harmonic generation*. Journal of Alloys and Compounds, 2011. 509: p.7861–7869

[30] Jensen, P., Kjekshus, A., Skansen, T., *The Systems Molybdenum-Arsenic, Tungsten-Arsenic, Molybdenum-Antimony, Tungsten-Antimony, Niobium-Bismuth, Tantalum-Bismuth, Molybdenum-Bismuth, and Tungsten-Bismuth*. Acta Chemica Scandinavica, 1966. 20: p.403-416.

[31] Boller, H. Nowotny, H*., Kristallchemische Untersuchungen in Systemen (Ti, Nb, Ta, Mo, W)-(As, Sb)*. Monatshefte für Chemie, 1964. 95: p.1272-1282.

[32] Furuseth, S., Selte, K., Kjekshus, A., *On the Arsenides and Antimonides of Tantalum*. Acta Chemica Scandinavica, 1965. 19: p.95-106.

[33] Henriques, D., Motalov, V., Bencze, L., Fürtauer, S., Markus, T., *Experimental thermodynamics of the Li–Sn system by Knudsen Effusion Mass Spectrometry*. Journal of Alloys and Compounds, 2014. 585: p.299-306.

[34] Studnitzky, T., Schmid-Fetzer, R., *Phase formation and reaction kinetics in M-Sn systems (M = Zr, Hf, Nb, Ta, Mo)*. Z. Metallkd., 2002. 93(9): p.894-903.

[35] Konys, J., Borgstedt, H.U., *THE PRODUCT OF THE REACTION OF ALUMINA WITH LITHIUM METAL*. Journal of Nuclear Materials, 1985. 131: p.158-161.

[36] Altintas, B., Parlak2, C., Bozkurt, C., Eryiğit, R*, Intercalation of graphite and hexagonal boron nitride by lithium*. The European Physical Journal B, 2011. 79: p.301-312.

[37] Holleman, A.F., Wiberg, E., Wiberg, N*., Lehrbuch der Anorganischen Chemie*. 2007, Berlin: Walter de Gruyter & Co.

[38] Atkins,P., de Paula, J., *Atkins' Physical Chemistry*. 2010, Oxford: Oxford University Press

[39] Waseda, Y., Matsubara, W., Shinoda, K., *X-Ray Diffraction Crystallography, Introduction, Examples and Solved Problems*. 2011, Berlin Heidelberg: Springer-Verlag.

[40] Suryanarayana, C., Norton, M.G., *X-Ray Diffraction, A Practical Approach*. 1998, New York: Plenum Press.

[41] Woolfson, M.M., *An introduction to X-ray crystallography*. 1997, Cambridge: Cambridge University Press.

[42] Gross, R., Marx, A., *Festkörperphysik*. 2012, München : Oldenbourg.

[43] West, A.R., *Grundlagen der Festkörperchemie*. 1992, Weinheim: VCH Verlagsgesellschaft mbH.

[44] Krischner, H., Koppelhuber-Bitschnau, B*., Röntgenstrukturanalyse und Rietveldmethode, eine Einführung*. 1994, Wiesbaden: Springer Fachmedien.

[45] Ladd, M., Palmer, R., *Structure Determination by X-ray Crystallography, Analysis by X-rays and Neutrons*. 2013, New York: Springer Science+Business Media, LLC.

[46] Speyer, R., *THERMAL ANALYSIS OF MATERIALS*. 1994, New York: MARCEL DEKKER, Inc.

[47] Hemminger, W.F., Cammenga, H.K., *Methoden der thermischen Analyse*. 1989, Berlin: Springer.

[48] Lajunen, L.H.J., *SPECTROCHEMICAL ANALYSIS BY ATOMIC ABSORPTION AND EMISSION*. 1992, Cambridge: The Royal Society of Chemistry.

[49] ed. Cantle, J.E., *ATOMIC ABSORPTION SPECTROSCOPY. TECHNIQUES AND INSTRUMENTATION IN ANALYTICAL CHEMISTRY-VOLUME 5*, 1982. Amsterdam: Elsevier Scientific Publishing Company.

[50] ed. Campbell, F.C., *Phase Diagrams, Understanding the Basics*. 2012, Ohio: ASM International; F.C. Campbell.

[51] Ladd, M.F.C., *The Radii of Spherical Ions*. Theoret. chim. Acta (Berl.), 1968. 12: p.333-336.

[52] Furuseth, S., Kjekshus, A., *The crystal structure of NbAs (comments)*. Acta Crystallographica, 1964. 17: p.1077-1078

9. Appendices

9.1. XRD data of all binary samples

Name	Sample preparation						XRD analysis									
	Li	Sb	T_{melt} [°C]	T_{anneal} [°C]	t_{anneal} [d]	Crucible material	phase	space group	Structure type	Lattice parameter [A] a	b	c	Amount [%]	R_B	R_{wp}	comments
LSB01_400	97	3	800r	400	21	Ta	Li	I*m-3m*	W	3.51	-	-	92	2.685	3.690	
							β-Li_3Sb	P*63/mmc*	Na_3As	4.69	-	8.33	8	2.073		
LSB02_400	90	10	800r	400	21	Ta	β-Li_3Sb	P*63/mmc*	Na_3As	4.70	-	8.31	100	0.974	2.878	
LSB03_400	80	20	1000r	400	21	Ta	α-Li_3Sb	F*m-3m*	BiF_3	6.58	-	-	4	0.516	0.957	
							β-Li_3Sb	P*63/mmc*	Na_3As	4.69	-	8.33	71	0.655		
							Sb	R-*3mH*	α-As	4.31	-	11.28	24	0.137		
LSB03_170	80	20	1000r	400	115	Ta	α-Li_3Sb	F*m-3m*	BiF_3	6.57	-	-	41	1.062	3.071	
							β-Li_3Sb	P*63/mmc*	Na_3As	4.69	-	8.33	59	2.171		
Li77Sb23_AlOx_500	77	23	T900r	500	0	alumina	Li reacted with silica tube									
Li77Sb23	77	23	1100i	500	27	Ta	α-Li_3Sb	F*m-3m*	BiF_3	6.58	-	-	33	0.441	2.835	
							β-Li_3Sb	P*63/mmc*	Na_3As	4.69		8.33	67	1.087		
Li75Sb25_AlOx_500	75	25	T900r	500	26	alumina	α-Li_3Sb	F*m-3m*	BiF_3	6.58	-	-	92	3.591	4.301	
							β-Li_3Sb	P*63/mmc*	Na_3As	4.66	-	8.40	2	1.699		
							Li2Sb	P-*62c*	Fe_2P	7.95	-	6.53	6	2.554		
Li75Sb25	75	25	1100i	500	27	Ta	α-Li_3Sb	F*m-3m*	BiF_3	6.58	-	-	31	2.082	3.627	
							β-Li_3Sb	P*63/mmc*	Na_3As	4.69	-	8.33	68	2.446		
							Li_2Sb	P-*62c*	Fe_2P	7.95	-	6.53	0,5	1.798		
Li75Sb25_800	75	25	-	800	30	Ta	α-Li_3Sb	F*m-3m*	BiF_3	6.58	-	-	43	2.330	3.217	
							β-Li_3Sb	P*63/mmc*	Na_3As	4.69	-	8.33	54	1.763		
							Li_2Sb	P-*62c*	Fe_2P	7.96	-	6.52	2	1.582		
							Sb	R-*3mH*	α-As	4.30	-	11.38	1	0.855		

Name	Sample preparation						XRD analysis									
	Li	Sb	T_{melt} [°C]	T_{anneal} [°C]	t_{anneal} [d]	Crucible material	phase	space group	Structure type	Lattice parameter [A] a	b	c	Amount [%]	R_B	R_{wp}	comments
Li75Sb25_900	75	25	-	900	30	Ta	α-Li_3Sb	F*m-3m*	BiF_3	6.58	-	-	72	3.774	3.988	
							β-Li_3Sb	P*63/mmc*	Na_3As	4.65	-	8.36	6	1.352		
							Li_2Sb	P-*62c*	Fe_2P	7.96	-	6.53	14	1.368		
							Sb	R-*3mH*	α-As	4.30	-	11.30	9	1.294		
Li75Sb25_1000	75	25	-	1000	30	Ta	α-Li_3Sb	F*m-3m*	BiF_3	6.58	-	-	39	1.426	3.035	
							β-Li_3Sb	P*63/mmc*	Na_3As	4.69	-	8.33	61	1.663		
Li73Sb27_AlOx_500	73	27	T900r	500	26	alumina	α-Li_3Sb	F*m-3m*	BiF_3	6.58	-	-	52	3.563	4.327	
							β-Li_3Sb	P*63/mmc*	Na_3As	4.65	-	8.37	4	1.391		
							Li_2Sb	P-*62c*	Fe_2P	7.95	-	6.53	36	4.261		
							Sb	R-*3mH*	α-As	4.31	-	11.31	8	0.657		
Li73Sb27	73	27	1100i	500	27	Ta	α-Li_3Sb	F*m-3m*	BiF_3	6.58	-	-	73	5.028	4.339	
							β-Li_3Sb	P*63/mmc*	Na_3As	4.68	-	8.33	14	0.940		
							Li_2Sb	P-*62c*	Fe_2P	7.95	-	6.53	7	1.360		
							Sb	R-*3mH*	α-As	4.30	-	11.27	5	0.665		
LSB04_500	70	30	1000r	500	21	Ta	α-Li_3Sb	F*m-3m*	BiF_3	6.58	-	-	52	1.244	3.188	
							β-Li_3Sb	P*63/mmc*	Na_3As	4.68	-	8.34	14	1.400		
							Li_2Sb	P-*62c*	Fe_2P	7.96	-	6.53	10	1.010		
							Sb	R-*3mH*	α-As	4.30	-	11.28	10	0.778		
							Sb_2Ta	C*121*	$OsGe_2$	10.23	3.65	8.30	15	1.609		
LSB04_700	70	30	1000r	700	14	Ta	α-Li_3Sb	F*m-3m*	BiF_3	6.59	-	-	53	1.754	7.277	
							Li_2Sb	P-*62c*	Fe_2P	7.95	-	6.33	3	2.417		
							Sb_4Ta_5	I*4/m*	Ti_5Te_4	10.25	-	3.55	44	5.516		
Li70Sb30_AlOx_500	70	30	T900r	500	46	alumina	α-Li_3Sb	F*m-3m*	BiF_3	6.58	-	-	24	3.174	3.785	
							β-Li_3Sb	P*63/mmc*	Na_3As	4.70	-	8.34	2	1.587		
							Li_2Sb	P-*62c*	Fe_2P	7.95	-	6.53	69	1.755		
							Sb	R-*3mH*	α-As	4.31	-	11.37	6	1.025		

Name	Sample preparation						XRD analysis									
	Li	Sb	T_{melt} [°C]	T_{anneal} [°C]	t_{anneal} [d]	Crucible material	phase	space group	Structure type	Lattice parameter [A] a	b	c	Amount [%]	R_B	R_{wp}	comments
LSB04_700_ind	70	30	900i	-	-	Ta	α-Li_3Sb	F*m-3m*	BiF_3	6.59	-	-	6	0.433	1.009	Quenched
							Li_2Sb	P-*62c*	Fe_2P	7.96	-	6.53	81	0.385		after
							Sb	R-*3mH*	α-As	4.31	-	11.29	14	0.273		melting
Li70Sb30_ind	70	30	900i	500	17	Ta	α-Li_3Sb	F*m-3m*	BiF_3	6.58	-	-	52	1.151	3.462	
							β-Li_3Sb	P*63/mmc*	Na_3As	4.68	-	8.33	10	0.680		
							Li_2Sb	P-*62c*	Fe_2P	7.95	-	6.53	13	1.549		
							Sb	R-*3mH*	α-As	4.31	-	11.26	5	0.761		
							Sb2Ta	C*121*	$OsGe_2$	10.23	3.65	8.30	20	1.795		
Li70Sb30_400	70	30	1000i	400	44	Ta	α-Li_3Sb	F*m-3m*	BiF_3	6.58	-	-	27	2.464	3.927	
							β-Li_3Sb	P*63/mmc*	Na_3As	4.69	-	8.33	19	1.489		
							Li_2Sb	P-*62c*	Fe_2P	7.95	-	6.53	49	4.205		
							Sb	R-*3mH*	α-As	4.30	-	11.29	5	0.691		
Li70Sb30_BN+lid_400	70	30	T800r	400	41	BN+lid	α-Li_3Sb	F*m-3m*	BiF_3	6.57	-	-	8	0.888	3.049	
							β-Li_3Sb	P*63/mmc*	Na_3As	4.69	-	8.33	55	1.628		
							Li_2Sb	P-*62c*	Fe_2P	7.95	-	6.53	34	1.415		
							Sb	R-*3mH*	α-As	4.30	-	11.32	3	0.564		
Li66Sb33_AlOx_500	66	33	T900r	500	26	alumina	Li_2Sb	P-*62c*	Fe_2P	7.95	-	6.53	92	3.045	4.017	
							Sb	R-*3mH*	α-As	4.30	-	11.34	8	0.563		
Li66Sb33	66	33	1100i	500	27	Ta	α-Li_3Sb	F*m-3m*	BiF_3	6.58	-		16	2.193	3.213	
							β-Li_3Sb	P*63/mmc*	Na_3As	4.70	-	8.34	2	0.896		
							Li_2Sb	P-*62c*	Fe_2P	7.95	-	6.53	53	1.447		
							Sb	R-*3mH*	α-As	4.31	-	11.30	10	1.191		
							Sb_2Ta	C*121*	$OsGe_2$	10.23	3.65	8.29	19	1.888		
LSB05_500	60	40	1000r	500	16	Ta	Li_2Sb	P-*62c*	Fe_2P	7.96	-	6.53	21	0.788	3.049	
							Sb	R-*3mH*	α-As	4.31	-	11.27	62	0.618		
							Sb_2Ta	C*121*	$OsGe_2$	10.23	3.65	8.29	17	1.256		

Name	Sample preparation						XRD analysis									
	Li	Sb	T_{melt} [°C]	T_{anneal} [°C]	t_{anneal} [d]	Crucible material	phase	space group	Structure type	Lattice parameter [A] a	b	c	Amount [%]	R_B	R_{wp}	comments
Li60Sb40_ind	60	40	900i	500	17	Ta	Li_2Sb	P-*62c*	Fe_2P	7.95	-	6.53	67	4.349	3.821	
							Sb	R-*3mH*	α-As	4.31	-	11.29	27	0.905		
							Sb_2Ta	C*121*	$OsGe_2$	10.23	3.65	8.28	7	1.282		
Li60Sb40_BN+lid_400	60	40	T800r	400	41	BN+lid	Li_2Sb	P-*62c*	Fe_2P	7.95	-	6.53	83	4.373	4.713	
							Sb	R-*3mH*	α-As	4.31	-	11.28	17	1.358		
Li55Sb45_MgOn_400	55	45	T800r	400	41	MgO	Li_2Sb	P-*62c*	Fe_2P	7.95	-	6.53	53	3.162	3.708	
							Sb	R-*3mH*	α-As	4.31	-	11.28	47	1.334		
Li50Sb50_AlOx_500	50	50	T900r	500	46	alumina	Li_2Sb	P-*62c*	Fe_2P	7.95	-	6.52	50	3.919	3.870	
							Sb	R-*3mH*	α-As	4.31	-	11.28	50	1.434		
LSB06_500	40	60	1000r	500	16	Ta	Li_2Sb	P-*62c*	Fe_2P	7.96	-	6.53	20	0.849	3.181	
							Sb	R-*3mH*	α-As	4.31	-	11.28	15	0.723		
							Sb_2Ta	C*121*	$OsGe_2$	10.23	3.65	8.30	65	2.001		
Li35Sb65_MgOn_400	35	65	T800r	400	41	MgO	Li_2Sb	P-*62c*	Fe_2P	7.95	-	6.53	15	4.036	3.853	
							Sb	R-*3mH*	α-As	4.31	-	11.28	85	2.434		
LSB07_500	25	75	800r	500	16	Ta	Li_2Sb	P-*62c*	Fe_2P	7.96	-	6.53	3	0.998	3.089	
							Sb	R-*3mH*	α-As	4.31	-	11.28	37	0.573		
							Sb2Ta	C*121*	$OsGe_2$	10.23	3.65	8.30	60	1.891		
Li25Sb75_BN_500	25	75	T850r	500	18	BN	Li_2Sb	P-*62c*	Fe_2P	7.95	-	6.52	18	1.794	3.869	
							Sb	R-*3mH*	α-As	4.31	-	11.28	82	1.062		
Li25Sb75_MgO_500A	25	75	800r	500	3	MgO	Silica tube corroded									
Li25Sb75_MgO_500B	25	75	800r	500	3	MgO	Spacer (Mo foil) reacted with Sb									
Li25Sb75_AlOx_500A	25	75	800r	500	9	alumina	Silica tube corroded due to a crack in the crucible material									
Li25Sb75_AlOx_500B	25	75	T850r	-	-	alumina	Li_2Sb	P-*62c*	Fe_2P	7.95		6.53	10	1.734	3.206	Quenched after melting
							Sb	R-*3mH*	α-As	4.31	-	11.28	90	1.755		
Li25Sb75_ind	25	75	800i	500	17	Ta	Li_2Sb	P-*62c*	Fe_2P	7.95	-	6.53	5	1.287	3.409	
							Sb	R-*3mH*	α-As	4.31	-	11.28	62	1.867		
							Sb_2Ta	C*121*	$OsGe_2$	10.23	3.65	8.30	33	2.378		

Name	Sample preparation						XRD analysis									
	Li	Sb	T_{melt} [°C]	T_{anneal} [°C]	t_{anneal} [d]	Crucible material	phase	space group	Structure type	Lattice parameter [A]			Amount [%]	R_B	R_{wp}	comments
										a	b	c				
Li25Sb75_400	25	75	800i	400	44	Ta	Li_2Sb	P-*62c*	Fe_2P	7.95	-	6.53	15	3.526	3.207	
							Sb	R-*3mH*	α-As	4.31	-	11.28	79	1.337		
							Sb_2Ta	C*121*	$OsGe_2$	10.23	3.65	8.29	7	1.251		
Li25Sb75_BNinv_400	25	75	800i	400	55	Ta	Li_2Sb	P-*62c*	Fe_2P	7.95	-	6.53	23	4.300	3.807	
							Sb	R-*3mH*	α-As	4.31	-	11.27	77	2.053		
Li20Sb80_AlOx_500	20	80	T900r	500	46	alumina	Li_2Sb	P-*62c*	Fe_2P	7.95	-	6.53	12	3.770	3.769	
							Sb	R-*3mH*	α-As	4.31	-	11.27	88	2.565		
Li10Sb90_AlOx_500	10	90	T900r	500	46	alumina	Li_2Sb	P-*62c*	Fe_2P	7.95	-	6.54	3	1.666	3.401	
							Sb	R-*3mH*	α-As	4.31	-	11.28	97	2.267		
LSB08_500	5	95	800r	500	16	Ta	Li_2Sb	P-*62c*	Fe_2P	7.95	-	6.54	2	1.349	3.877	
							Sb	R-*3mH*	α-As	4.31	-	11.28	71	1.276		
							Sb_2Ta	C*121*	$OsGe_2$	10.23	3.65	8.30	26	1.835		

9.2. XRD data of all ternary samples

Name	Composition [at%]			Heat treatment		XRD analysis									
	Li	Cu	Sb	T [°C]	t [d]	phase	Space group	Structure type	Lattice parameter [A]			Amount [%]	R_B	R_{wp}	comments
									a	b	c				
Li05Cu76Sb19	5	76	19	400	40	Cu_4Sb	P*63/mmc*	Mg	2.73	-	4.33	69	0.794	1.581	
						Cu	F*m-3m*	Cu	3.65	-	-	31	0.420		
						T4	P*6???*	???	4.24	-	22.33	???	0.061		
Li05Cu70Sb25	5	70	25	400	40	Cu_2Sb	P*4/nmmS*	Cu_2Sb	4.00	-	6.11	72	2.853	2.756	
						T2	P*63/mmc*	$Cu_5Li_2Sb_3$	4.32	-	7.42	16	1.859		
						Sb	R-*3mH*	α-As	4.31	-	11.27	13	1.172		
Li05Cu63Sb31	5	63.33	31.67	400	34	Cu_2Sb	P*4/nmmS*	Cu_2Sb	4.00	-	6.11	100	1.277	2.103	
						T4	P*6???*	???	4.24	-	22.33	???	0.085		
Li05Cu57Sb38	5	57	38	400	61	Cu_2Sb	P*4/nmmS*	Cu_2Sb	4.00	-	6.11	71	2.676	2.676	
						T2	P*63/mmc*	$Cu_5Li_2Sb_3$	4.32	-	7.43	14	0.949		
						Sb	R-*3mH*	α-As	4.31	-	11.27	12	1.636		
						Sb_2Ta	C*121*	OsGe2	10.23	3.65	8.29	3	0.859		
Li05Cu47Sb47	5	47.5	47.5	400	41	Cu_2Sb	P*4/nmmS*	Cu_2Sb	4.00	-	6.11	59	3.270	2.951	
						T2	P*63/mmc*	$Cu_5Li_2Sb_3$	4.32	-	7.43	8	0.809		
						Sb	R-*3mH*	α-As	4.31	-	11.27	29	0.794		
						Sb_2Ta	C*121*	$OsGe_2$	10.23	3.65	8.29	4	1.190		
Li05Cu38Sb57	5	38	57	400	41	Cu_2Sb	P*4/nmmS*	Cu_2Sb	4.01	-	6.11	39	1.956	2.861	
						T2	P*63/mmc*	$Cu_5Li_2Sb_3$	4.32	-	7.43	15	0.905		
						Sb	R-*3mH*	α-As	4.31	-	11.27	39	1.602		
						Sb_2Ta	C*121*	$OsGe_2$	10.23	3.65	8.29	7	0.977		
Li05Cu31Sb63	5	31.67	63.33	400	34	Cu_2Sb	P*4/nmmS*	Cu_2Sb	4.01	-	6.11	30	1.294	2.855	
						T2	P*63/mmc*	$Cu_5Li_2Sb_3$	4.32	-	7.42	13	0.934		
						Sb	R-*3mH*	α-As	4.31	-	11.27	36	2.002		
						Sb_2Ta	C*121*	$OsGe_2$	10.23	3.65	8.30	21	1.501		

Name	Composition [at%]			Heat treatment		XRD analysis									
	Li	Cu	Sb	T [°C]	t [d]	phase	Space group	Structure type	Lattice parameter [A]			Amount [%]	R_B	R_{wp}	comments
									a	b	c				
Li10Cu72Sb18	10	72	18	400	40	T2	P*63/mmc*	$Cu_5Li_2Sb_3$	4.32	-	7.42	63	1.057	2.157	
						Cu	F*m-3m*	Cu	3.62	-	-	37	2.327		
						T4	P*6???*	???	4.22	-	22.35	???	0.070		
Li10Cu68Sb23	10	68	23	400	53	T2	P*63/mmc*	$Cu_5Li_2Sb_3$	4.32	-	7.44	38	0.653	1.595	
						Cu	F*m-3m*	Cu	3.68	-	-	62	0.885		
						T4	P*6???*	???	4.24	-	22.34	???	0.046		
Li10Cu54Sb36	10	54	36	400	61	Cu_2Sb	P*4/nmmS*	Cu_2Sb	4.00	-	6.11	59	2.248	2.599	
						T2	P*63/mmc*	$Cu_5Li_2Sb_3$	4.32	-	7.43	30	1.319		
						Sb	R-*3mH*	α-As	4.31	-	11.26	11	1.053		
Li10Cu45Sb45	10	45	45	400	41	Cu_2Sb	P*4/nmmS*	Cu_2Sb	4.01	-	6.11	42	2.353	2.935	
						T2	P*63/mmc*	$Cu_5Li_2Sb_3$	4.32	-	7.44	29	1.395		
						Sb	R-*3mH*	α-As	4.31	-	11.27	24	1.135		
						Sb_2Ta	C*121*	$OsGe_2$	10.22	3.64	8.32	5	0.957		
Li15Cu68Sb17	15	68	17	400	40	Cu_2Sb	P*4/nmmS*	Cu_2Sb	4.01	-	6.17	7	0.946	2.417	
						Cu	F*m-3m*	Cu	3.62	-	-	54	2.805		
						T3	P*63mc*	$Cu_{45}Li_{30}Sb_{25}$	4.35	-	14.42	35	1.608		
						Sb	R-*3mH*	α-As	4.32	-	11.22	4	0.776		
Li15Cu64Sb21	15	64	21	400	53	Cu_2Sb	P*4/nmmS*	Cu_2Sb	4.01	-	6.11	20	0.687	1.941	
						T2	P*63/mmc*	$Cu_5Li_2Sb_3$	4.32	-	7.45	62	1.084		
						Cu	F*m-3m*	Cu	3.63	-	-	19	0.704		
						T4	P*6???*	???	4.26	-	22.36	≈15	0.045		
LiCuSb01_400	14.29	57.14	28.57	400	19	T2	P*63/mmc*	???	4.33	-	7.45	80	2.596	3.304	
						T4	P6??	???	4.24	-	22.33	20	2.397		

Name	Composition [at%]			Heat treatment		XRD analysis									
	Li	Cu	Sb	T [°C]	t [d]	phase	Space group	Structure type	Lattice parameter [A]			Amount [%]	R_B	R_{wp}	comments
									a	b	c				
Li15Cu51Sb34	15	51	34	400	60	Cu_2Sb	P*4/nmmS*	Cu_2Sb	4.00	-	6.11	48	2.922	2.917	
						T2	P*63/mmc*	$Cu_5Li_2Sb_3$	4.32	-	7.44	37	1.469		
						T4	P*6???*	???	4.19	-	21.36	???	0.105		
						Sb	R-*3mH*	α-As	4.31	-	11.26	11	0.927		
						Sb_2Ta	C*121*	$OsGe_2$	10.23	3.65	8.30	4	0.871		
Li20Cu48Sb32	20	48	32	400	61	Cu_2Sb	P*4/nmmS*	Cu_2Sb	4.00	-	6.10	27	1.884	3.515	
						T2	P*63/mmc*	$Cu_5Li_2Sb_3$	4.31	-	7.43	60	2.133		
						Sb	R-*3mH*	α-As	4.31	-	11.24	13	1.510		
Li20Cu40Sb40	20	40	40	400	24	T2	P*63/mmc*	$Cu_5Li_2Sb_3$	4.31	-	7.41	75	3.008	3.984	Very small amount of unknown phase present
						Sb	R-*3mH*	α-As	4.30	-	11.23	25	1.138		
Li25Cu60Sb15	25	60	15	400	40	Cu	F*m-3m*	Cu	3.62	-	-	49	2.793	3.521	
						$CuLi_2Sb$	F-*43m*	$CuHg_2Ti$	6.23	-	-	45	3.200		
						T3	P*63mc*	$Cu_{45}Li_{30}Sb_{25}$	4.35	-	14.40	6	3.878		
Li25Cu56Sb19	25	56	19	400	53	Cu	F*m-3m*	Cu	3.62	-	-	25	0.860	2.985	
						$CuLi_2Sb$	F-*43m*	$CuHg_2Ti$	6.24	-	-	57	2.241		
						T2	P*63/mmc*	$Cu_5Li_2Sb_3$	4.33	-	7.43	18	2.321		
Li25Cu50Sb25	25	50	25	400	34	Cu	F*m-3m*	Cu	3.61	-	-	5	1.369	2.077	
						T2	P*63/mmc*	$Cu_5Li_2Sb_3$	4.34	-	7.45	71	1.613		
						T3	P*63mc*	$Cu_{45}Li_{30}Sb_{25}$	4.37	-	14.44	18	2.127		
						Sb	R-*3mH*	α-As	4.32	-	11.24	5	0.578		
Li25Cu45Sb30	25	45	30	400	61	T2	P*63/mmc*	$Cu_5Li_2Sb_3$	4.32	-	7.43	88	2.683	3.884	
						Sb	R-*3mH*	α-As	4.31	-	11.26	12	2.163		
Li25Cu25Sb50	25	25	50	400	34	T3	P*63mc*	$Cu_{45}Li_{30}Sb_{25}$	4.35	-	14.41	16	1.723	2.798	One small peak unidentified (2θ=43.4).
						T5	I*41*	NbAs	4.38	-	6.05	35	1.669		
						Sb	R-*3mH*	α-As	4.31	-	11.27	38	1.230		
						Sb_2Ta	C*121*	$OsGe_2$	10.22	3.64	8.29	11	1.331		

Name	Composition [at%]			Heat treatment		XRD analysis									
	Li	Cu	Sb	T [°C]	t [d]	phase	Space group	Structure type	Lattice parameter [A]			Amount [%]	R_B	R_{wp}	comments
									a	b	c				
Li28Cu36Sb36	28	36	36	400	40	T3	P*63mc*	$Cu_{45}Li_{30}Sb_{25}$	4.35	-	14.42	71	1.337	2.942	One small peak unidentified (2θ=43.4).
						Sb	R-*3mH*	α-As	4.31	-	11.27	28	1.727		
						Sb_2Ta	C*121*	$OsGe_2$	10.22	3.64	8.29	2	1.173		
Li30Cu42Sb28	30	42	28	400	53	$CuLi_2Sb$	F-*43m*	$CuHg_2Ti$	6.22	-	-	37	3.399	3.805	
						T5	I*41*	NbAs	4.38	-	6.04	34	3.558		
						Sb	R-*3mH*	α-As	4.30	-	11.26	29	1.621		
LiCuSb02_400	33.81	43.81	22.38	400	19	Cu	F*m-3m*	Cu	3.62	-	-	23	1.263	2.603	Some peaks of T3 are not present in the pattern.
						$CuLi_2Sb$	F-*43m*	$CuHg_2Ti$	6.24	-	-	69	1.660		
						T3	P*63mc*	$Cu_{45}Li_{30}Sb_{25}$	4.33	-	14.45	7	3.519		
Li33Cu33Sb33	33.33	33.33	33.33	400	24	$CuLi_2Sb$	F-*43m*	$CuHg_2Ti$	6.23	-	-	30	2.191	2.916	
						T3	P*63mc*	$Cu_{45}Li_{30}Sb_{25}$	4.35	-	14.42	23	1.560		
						T5	I*41*	NbAs	4.38	-	6.05	29	1.452		
						Sb	R-*3mH*	α-As	4.31	-	11.27	18	0.902		
Li40Cu24Sb36	40	24	36	400	34	Li_2Sb	P-*62c*	Fe_2P	7.93	-	6.51	2	1.955	4.813	One small peak unidentified (2θ=43.4); small amount of unknown phase present.
						$CuLi_2Sb$	F-*43m*	$CuHg_2Ti$	6.21	-	-	60	2.465		
						Sb	R-*3mH*	α-As	4.31	-	11.27	38	3.601		
Li40Cu20Sb40	40	20	40	400	34	Li_2Sb	P-*62c*	Fe_2P	7.93	-	6.52	7	2.023	4.731	
						$CuLi_2Sb$	F-*43m*	$CuHg_2Ti$	6.22	-	-	57	3.469		
						Sb	R-*3mH*	α-As	4.31	-	11.28	36	3.165		
LiCuSb03_400	45.24	36.67	18.09	400	19	α-Li_3Sb	F*m-3m*	BiF_3	6.57	-	-	8	0.383	2.181	
						β-Li_3Sb	P*63/mmc*	Na_3As	4.68	-	8.33	16	0.564		
						Cu	F*m-3m*	Cu	3.62	-	-	39	2.085		
						$CuLi_2Sb$	F-*43m*	$CuHg_2Ti$	6.25	-	-	22	0.398		

Name	Composition [at%]			Heat treatment		XRD analysis									
	Li	Cu	Sb	T [°C]	t [d]	phase	Space group	Structure type	Lattice parameter [A]			Amount [%]	R_B	R_{wp}	comments
									a	b	c				
Li45Cu33Sb22	45	33	22	400	61	α-Li_3Sb	F*m-3m*	BiF_3	6.56	-	-	0.5	1.708	4.979	
						Cu	F*m-3m*	Cu	3.62	-	-	12	0.933		
						$CuLi_2Sb$	F-*43m*	$CuHg_2Ti$	6.26	-	-	88	3.200		
Li45Cu28Sb28	45	28	28	400	61	Li_2Sb	P-*62c*	Fe_2P	7.94	-	6.52	13	2.866	5.350	One small peak unidentified (2θ=41.7)
						$CuLi_2Sb$	F-*43m*	$CuHg_2Ti$	6.23	-	-	87	3.696		
Li50Cu20Sb30	50	20	30	400	34	Li_2Sb	P-*62c*	Fe_2P	7.93	-	6.52	16	1.639	4.013	One small peak not fully identified (2θ=41.7)
						$CuLi_2Sb$	F-*43m*	$CuHg_2Ti$	6.23	-	-	70	3.008		
						Sb	R-*3mH*	α-As	4.31	-	11.27	14	2.280		
Li60Cu16Sb24	60	16	24	400	34	α-Li_3Sb	F*m-3m*	BiF_3	6.56	-	-	38	2.786	4.159	
						Cu	F*m-3m*	Cu	3.61	-	-	5	0.806		
						$CuLi_2Sb$	F-*43m*	$CuHg_2Ti$	6.26	-	-	56	2.365		
Li60Cu13Sb27	60	13	27	400	41	Li_2Sb	P-*62c*	Fe_2P	7.94	-	6.53	1	1.085	4.084	
						α-Li_3Sb	F*m-3m*	BiF_3	6.56	-	-	32	2.873		
						$CuLi_2Sb$	F-*43m*	$CuHg_2Ti$	6.24	-	-	67	2.287		
Li70Cu20Sb10	70	20	10	400	34	Li	I*m-3m*	W	3.49	-	-	3	0.816	2.809	
						α-Li_3Sb	F*m-3m*	BiF_3	6.58	-	-	22	1.246		
						β-Li_3Sb	P*63/mmc*	Na_3As	4.69	-	8.33	53	1.743		
						Cu	F*m-3m*	Cu	3.65	-	-	22	2.479		
Li70Cu12Sb18	70	12	18	400	34	α-Li_3Sb	F*m-3m*	BiF_3	6.58	-	-	21	1.960	3.050	
						β-Li_3Sb	P*63/mmc*	Na_3As	4.69	-	8.32	48	1.517		
						Cu	F*m-3m*	Cu	3.64	-	-	31	1.043		

9.3. DTA data of the measured binary samples

Name	Composition		Crucible	T_{melt}	T_{anneal}	t	DTA analysis						
	Li	Sb	material	[°C]	[°C]	[d]	Heating rate	T_{max} [°C]	crucible	1.heating [°C]	2.heating [°C]	1.cooling [°C]	2. cooling [°C]
LSB01_400	95	5	Ta	800f	400	21	5	700	Ta	179.9i	177.6i	181.5i 381.4L	181.5i 411.1L
LSB02_400	90	10	Ta	800f	400	21	5	1000	Ta	179.5i W812.8L	178.8i	181.4i 393.0ni 408.8ni 980.1L	181.4i 393.3ni 406.0ni 981.3L
LSB03_400	80	20	Ta	1000f	400	21	5	1200	Ta	179.5i 1186.1L	179.3i 1189.1L	181.5i 916.0i 1183.7L	181.5i 944.2i 1181.1L
LSB03_170	80	20	Ta	1000f	170	115	5	1300	Ta	181.1i 1035.8ni w1065.0ni w1148.3L	181.8i w1113.8ni 1144.0L	181.4i W831.9ni W900.0ni 1119.4i 1143.5L	181.4i W861.1ni W922.3ni 1123.1i 1140.2L
Li25Sb75_BN_500	25	75	BN	850f	500	18	5	850	Ta	466.0i 836.0ni	460.0i 580.0i 752.0ni	455i 542.0ni 557.0i	W450i 545.0ni 562.0i
								850	Ta+BNinlet	W540.1ni	477.0i 540.6ni	471.0i 491.0i	470.0i 509.0i
Li66Sb33_AlOx_500	66	33	alumina	900f	500	26	5	1250	Ta+BNinlet	W489.8i 590.4i W1021.5ni/L	474.8i 587.2i W1008.6ni/L	458.2i 578.1i W992.1ni/L	447.6i 579.2i W988.0ni/L
Li75Sb25	75	25	Ta	1100i	500	27	5 5	1250 1350	Ta Ta	W951.9i W948.4i 1307.0L	W950.5i 1287.1L	W944.8i 1261.7i 1294.0L	 1258.3i 1271.9L

i…invariant reaction; ni…non-invariant reaction; L…liquidus; W…weak signal

9.4. Curriculum Vitae et Studiorum

Name:	Alexander Beutl
D.O.B.:	Nov.9th. 1988. Vienna
Citizenship:	Austria
Home address:	Otto-Probst-Str. 5/33/7. 1100Wien

Education and Career

Planned to start at 09/2014	PhD studies at the Department of Inorganic Chemistry / Materials Chemistry. Vienna
2013-2014	Master thesis at the Department of Inorganic Chemistry / Materials Chemistry. Vienna: Phase Equilibria in the Intermetallic System Li-Cu-Sb
2008-2013	Master studies at the University of Vienna: Chemistry
2006-2007	basic military service
1998-2006	Secondary school in Vienna. Austria